Physics – Uspekhi **64** (8) 747 – 800 (2021)

REVIEWS OF TOPICAL PROBLEMS PACS number: 96.15.Hy

Gas envelopes of exoplanets — hot Jupiters

D V Bisikalo, V I Shematovich, P V Kaygorodov, A G Zhilkin

DOI: https://doi.org/10.3367/UFNe.2020.11.038879

Contents

1. **Introduction** **747**
2. **Upper atmospheres of hot Jupiters** **749**
   2.1 Heating of hydrogen-dominated atmosphere by extreme stellar radiation; 2.2 Extreme stellar radiation effect on heating efficiency; 2.3 Heating by electron precipitation into the exoplanetary upper atmosphere; 2.4 Aeronomic model of a hot Jupiter taking into account suprathermal particles
3. **Gas dynamics of envelopes of hot Jupiters** **758**
   3.1 Roche lobe overflow by the planetary atmosphere; 3.2 Stabilization of hot Jupiter envelopes by stellar wind; 3.3 Effect of stellar radiation on flow in the envelope
4. **Magnetic field effect on the dynamics of envelopes of hot Jupiters** **774**
   4.1 Effect of the proper planetary magnetic field; 4.2 Stellar wind effect; 4.3 Sub-Alfvénic flow regime; 4.4 Development of MHD models: necessary steps
5. **Effect of stellar activity on envelopes of hot Jupiters** **785**
   5.1 Effect of a stellar flare on the dynamical state of the atmosphere; 5.2 Interaction of coronal mass ejections with extended envelopes of hot Jupiters; 5.3 Dependence of the exoplanetary atmospheric mass loss on the coronal mass ejection rate; 5.4 Effect of a magnetic field on envelope interaction with coronal mass ejections
6. **Conclusions** **796**

References **798**

Abstract. We consider the physical characteristics and dynamics of the gaseous envelopes of hot Jupiters (HJs) — gas giants with a mass comparable to Jupiter's and a semi-major axis of less than 0.1 a.u. Although HJs were discovered almost a quarter of a century ago, many issues about their origin remain open. There are two reasons for the scientific interest in HJs. The first is the absence of such planets in the Solar System, which is challenging in all cosmogonical theories. The second is that the exoplanet atmospheres' characteristics can now be derived primarily for transit HJs by examining their absorption spectra. Thanks to their large size, such planets can be readily observed, as opposed to others, and their transits can be observed at much higher orbital inclinations. Comparatively recently, in at least some HJs, extended gas envelopes far exceeding their Roche lobes have been found. The paper focuses on the results of theoretical investigations and numerical modeling of the dynamics of HJ envelopes. We also discuss experimental testing of the obtained results and predictions using the planned Russian Spectrum-UV (international name: WSO-UV) and Millimetron space telescopes.

D V Bisikalo [(a)], **V I Shematovich** [(b)], **P V Kaygorodov** [(c)], **A G Zhilkin** [(d)]
Institute of Astronomy, Russian Academy of Sciences,
ul. Pyatnitskaya 48, 119017 Moscow, Russian Federation
E-mail: [(a)] bisikalo@inasan.ru, [(b)] shematov@inasan.ru,
[(c)] pasha@inasan.ru, [(d)] zhilkin@inasan.ru

Received 1 June 2020, revised 9 November 2020
Uspekhi Fizicheskikh Nauk **191** (8) 785 – 845 (2021)
Translated by P Konstantinov

Keywords: hot Jupiters, exoplanetary atmospheres, aeronomic models, MHD

1. Introduction

The presence of planets around distant stars was hypothesized quite long ago. However, for a long time, observational capabilities were insufficient to detect them. Partially, successful searches were hampered by the generally recognized notion of the Solar System's ordinary nature, suggesting a hunt for long-period planets around solar-type stars. Nevertheless, one of the first planets, 51 Peg b, discovered in 1995 [1], had entirely unexpected parameters: a mass of about half of Jupiter's and a very short orbital period of four days, meaning its distance to the host star was one seventh that from Mercury to the Sun. Later on, many similar objects were discovered around different stars. As a result, they were commonly dubbed hot Jupiters (HJs).

The discovery of HJs became a challenge for planetary cosmogony. Indeed, commonly accepted cosmogonical theories [2–5] predict the formation of giant planets only in high orbits where they can accrete sufficient matter before protoplanetary disk dissipation. Subsequently, according to these theories, giant planets continue revolving in the same orbits, explaining the Solar System's observed structure. To explain the origin of HJs, several hypotheses have been proposed. They can be subdivided into three groups: (a) the formation of HJs directly in low orbits; (b) the migration of gas giants formed beyond the snow line to low orbits due to the interaction with a gas-dust protoplanetary disk; (c) the tidal capture of gas giants by a host star to highly eccentric

orbits (see, e.g., recent reviews [6–8]). Unfortunately, despite the quarter of a century since the discovery of the first HJ, there is no consensus as to their principal or preferable formation mechanism as yet. Each proposed hypothesis has its advantages and limitations. For example, group (a) hypotheses are supported by many HJs with low inclination circular orbits. However, by assuming that future HJs are super-Earths accreting matter from the protoplanetary disk (see, e.g., [9]), their formation demands very high surface densities of the solid fraction in the inner disk parts. This contradicts both observations (albeit quite limited) and theoretical models of protoplanetary disks. The migration caused by the interaction with the protoplanetary disk (group b) and/or other massive planets (group c) is supported by many HJs in elliptical high-inclination orbits. In addition, the migration in the disk (group b) enables us to understand the observed distribution of orbital periods of gas giants [10], and the tidal migration (group c) explains the absence of small planets near HJs and HJs in mildly eccentric orbits [6]. At the same time, to implement group b mechanisms, specific disk properties should be sustained that, in turn, contradict the observed population of other exoplanets. For group c mechanisms to operate, a planetary system should have a particular architecture, which (with the current statistics) is also not always supported by observations. Clearly, further progress in studying the cosmogony of planetary systems with HJs requires the accumulation of observations and the development of theoretical models. One possible research avenue includes studying the physical and chemical properties of the atmosphere and gas envelopes of hot Jupiters, enabling us to find additional indications of the HJ formation place in a planetary system.

As of the time of writing (April 2020), the database http://exoplanet.eu includes about 500 reliable objects with a mass $> 0.25\,M_{\rm jup}$ and a semimajor axis < 0.1 a.u., enabling their classification as HJs. Nearly half of them have zero orbital eccentricity; maximal eccentricity exceeds 0.5. Photometric radii of most HJs fall within the range of $(1-2)\,R_{\rm jup}$ (see Fig. 1); however, several planets have much smaller radii (down to $\lesssim 0.1\,R_{\rm jup}$). Also, two planets with a mass of several dozen Jupiters were found to have much larger radii, ~ 5 and $\sim 6\,R_{\rm jup}$.

There are two reasons for the scientific interest in HJs. First, there are no HJ analogues in the Solar System; hence, there is an opportunity to test cosmogonical theories. Second, detailed characteristics of exoplanet atmospheres can now be derived from observations of HJs only. The fact that there are many known HJs and observing them is comparatively simple make them attractive objects for studies. Many known HJs exhibit transits, making it possible to get information on their form and envelope composition from their light curves and spectral data.

The first observations of transiting HJs yielded unexpected results. For example, the disk of the planet HD 209458b can block only 1.8% of stellar light during an eclipse, but in the Ly-α line, the eclipse can attain 15% [11, 12]. Later, a similar effect was observed in C, O, and Si lines [13–15]. Moreover, in many HJs, the eclipse in lines starts much earlier and ends much later than in the continuum [16, 17]. These features suggest the presence of very extended gas envelopes around HJs. Their size significantly exceeds that of the atmosphere, and the envelopes should intensively interact with the host star, the stellar wind, and the planet itself, offering a unique opportunity to explore these objects.

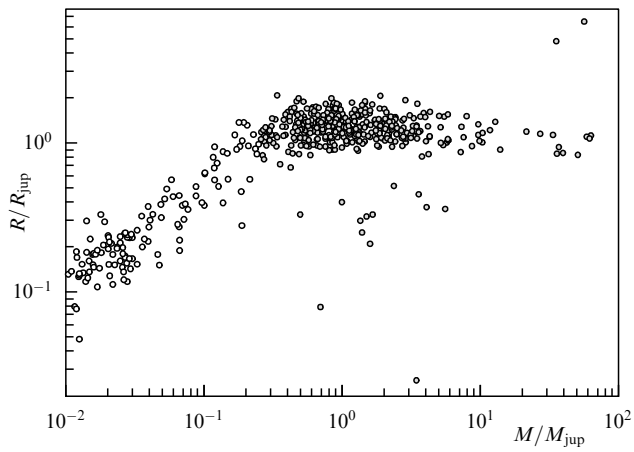

Figure 1. Mass – radius diagram for exoplanets with masses $> 0.01\,M_{\rm jup}$ and semi-major axes < 0.1 a.u. HJs (with masses $> 0.25\,M_{\rm jup}$) are shown by grey dots.

Since their discovery, extended envelopes of HJs and the structure of the outer layers of these exoplanets have been carefully investigated. For example, paper [18] showed that the main factor determining the atmospheric structure of HJs is extreme ultraviolet and soft X-ray heating from the host star. Subsequent aeronomic models studied the structure and chemical processes in the atmosphere in detail and revealed the main components absorbing radiation [19–22]. More complicated models were developed later, taking into account both magnetic fields [23–25] and kinetic processes [26, 27]. Already, the first papers revealed that the standard definition of atmosphere as a region extending up to the exobase, where the Knudsen number becomes approximately equal to one, becomes hardly applicable in this case. Indeed, the strong heating leads to the atmosphere expanding beyond the Roche lobe (the Hill sphere, in other words). The presence of a nearby star results in gas outflow and the formation of a gas cloud with a high density (low Knudsen numbers) but weakly gravitationally bound to the planet. These facts enabled researchers to recognize that HJs possess so-called gas envelopes extending from the exobase to the interstellar medium, in addition to the proper atmosphere. Subsequently, based on gas-dynamical calculations [28, 29], extended envelopes of HJs were shown to belong to one of three types: closed, when the envelope lies entirely inside the Roche lobe, quasi-closed, when the envelope is stabilized by the dynamical pressure of the stellar wind far beyond the Roche lobe, or open, when the outflow from the atmosphere cannot be stopped. In a quasi-closed atmosphere, the mass-loss rate is approximately equal to that of a closed atmosphere, sustaining the envelope for a long time.

The presence of asymmetric extended envelopes around HJs is supported by observations from the Hubble Space Telescope (HST). For example, observations of WASP-12b [16, 30] indicate an early start of the near UV eclipse at phase $\phi \sim 0.92$, whereas the optical eclipse starts at phase $\phi \sim 0.94$. The early eclipse suggests absorbing matter present in front of the planet at distances up to several planet radii. Observations of WASP-12b in 2013 [31] revealed an even more complex character of the planetary atmosphere. The HST COS (Cosmic Origins Spectrograph) spectroscopic data demonstrated an eclipse much earlier than at phase $\phi \sim 0.92$, starting at phase $\phi \sim 0.83$, corresponding, in fact, to the beginning of observa-

tions. A noticeable UV absorption of stellar emission starting from phase $\phi \sim 0.83$ was also noted in paper [30]. Thus, it can be stated that both theoretical studies and observations provide evidence of the presence of large asymmetric gas envelopes around hot Jupiters, which can be quasi-closed and quasi-stationary or open (nonstationary).

Note that hot Jupiters, in addition to extended envelopes, demonstrate several other intriguing features:

• the extended atmosphere and gas envelope leads to the formation of a large transitional region (part of the atmosphere where the Knudsen numbers are of the order of one), bringing about a much more important role for nonthermal processes in the physics of HJ atmospheres;

• the close distance to the star means that the planets are inside the region where tidal forces are strong. As we know from close binary star research, this can lead to Roche lobe overflow by the atmosphere and gas outflow through the vicinity of the libration points. The supersonic stellar wind and orbital motion of the typical HJ lead to the formation of a bow shock and the appearance of many features in the gas dynamics of HJ envelopes;

• thanks to the star's close location, such planets are located inside the stellar strong magnetic field, which can significantly affect the envelope dynamics, even if the proper planetary magnetic field is weak;

• gas envelopes of hot exoplanets must be heavily subjected to the host star's flares and coronal mass ejections. Considering that the envelopes of these planets have large sizes and are weakly bound gravitationally, stellar activity should significantly affect the envelope dynamics and evolution.

In the present paper, we summarize the main results of studies of HJ gas envelopes taking into account the above features. The paper consists of four sections reviewing specific physical phenomena determining characteristics of atmospheres and envelopes of HJs. Section 2 considers aeronomic models of HJ atmospheres and their interaction with stellar wind particles. Section 3 describes gas-dynamical models of HJ envelopes. Section 4 considers the effects of the proper magnetic field and stellar wind magnetic field on the HJ envelope properties. Section 5 describes the effects of stellar activity on the HJ envelope dynamics. The Conclusion (Section 6) briefly summarizes the main results and discusses the possibility of observing the effects reported in the paper using existing and future ground-based and space telescopes.

2. Upper atmospheres of hot Jupiters

The rapidly growing number of exoplanets has stimulated present studies of the physical and chemical evolution of planetary atmospheres. Observations of exoplanets provide new grounds for planetary cosmogony and enable investigating their evolution with the help of modern aeronomic models of exoplanetary upper atmospheres.

In an exoplanetary upper atmosphere, two regions can be distinguished: the thermosphere and exosphere, shown in Fig. 2 for Jupiter in the Solar System. The thermosphere is located above the homopause above which turbulent mixing is small, and partial atmospheric height scales characterize the height distribution of the principal components. In the thermosphere, the temperature increases due to the direct absorption of stellar short-wavelength radiation by rarefied gas above the temperature minimum at the upper mesosphere boundary (mesopause) lying below. In addition to heating by

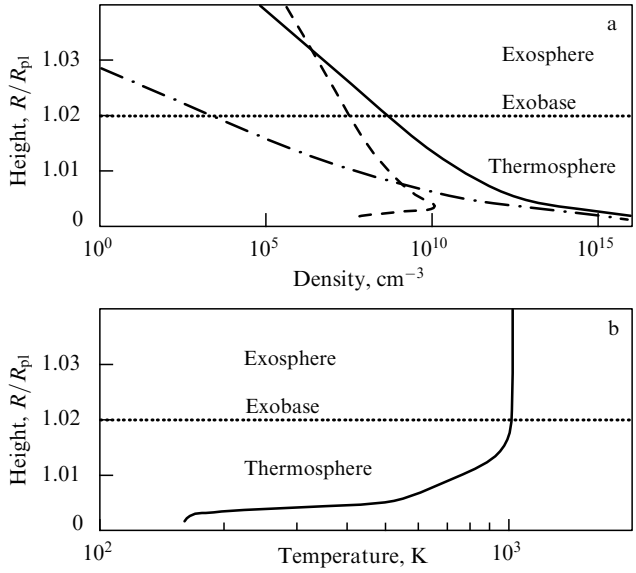

Figure 2. (a) Number density height profiles of molecular hydrogen (solid line), atomic hydrogen (dashed line), and helium (dashed-dotted line) in the Jovian atmosphere according to model [32]. (b) Atmospheric gas temperature height profile. The height is in units of Jupiter's photometric radius. Also shown are two main atmospheric regions: the thermosphere and the exosphere, separated by the conventional boundary, the exobase (horizontal dotted line).

stellar extreme UV radiation, the thermosphere structure and dynamics are also controlled by the IR heating of its lower layers, radiative and collisional cooling, energy dissipation of gravitational and planetary waves, thermal tides, and the precipitation of charged particles [33–35]. Particle collisions occur in the thermosphere but are virtually absent in the exosphere (also referred to as the planetary corona) lying above. The exosphere is separated from the thermosphere by the exobase, above which molecules and atoms can travel the distances of planetary scale with a low collision probability. At such altitudes, particles with energies exceeding their gravitational attraction energy and streaming along ballistic trajectories can escape into outer space. The exobase is determined as the scale at which the atmospheric height scale becomes comparable to the microscopic scale — the mean free path of particles between collisions. Correspondingly, above the exobase, only a very limited number of collisions occur, and from the viewpoint of kinetic theory of gases, any particle from this zone can leave the planetary atmosphere [36, 37].

A high particle velocity at the exobase level can be achieved in different physical processes. It is determined, in the first place, by the upper atmosphere temperature controlling thermal escape. The fraction of particles escaping from the atmosphere is regulated by the local temperature varying in space and time. If the atmosphere near the exobase is in hydrostatic equilibrium, the local velocity distribution of particles is Maxwellian, and the process is called 'Jeans escape' (or evaporation). The relation between the gravitational and kinetic energies at this level is referred to as the 'Jeans escape parameter.' If this parameter is close to one, the planet's gravity weakly bounds its atmosphere. In this case, its state deviates from the hydrostatic equilibrium, and the local particle velocity distribution is a Maxwellian with shifted velocity, for which the escape probability of particles increases. Traditionally, this escape mechanism is called

hydrodynamical outflow or planetary wind, in analogy with the solar wind. In both cases above, the escape of particles is determined by the upper atmosphere temperature. Therefore, both the Jeans and hydrodynamical escapes are a particular case of thermal escape: the atmospheric dissipation via Jeans escape does not change the particles' velocity distribution (upper atmosphere temperature) at the exobase level, whereas the hydrodynamical escape strongly affects the particles' velocity distribution and upper atmosphere temperature. See the known reviews for a detailed description, history, and present state of thermal dissipation studies [36–38]. In addition to the thermal dissipation mechanism, there can be a nonthermal escape from a planet's atmosphere when the velocity of escaping particles does not depend on the exobase temperature. Most nonthermal escape processes are related to the exothermic reactions of atmospheric photochemistry, the presence of ions, and their behavior in electric and magnetic fields [37–40]. Nonthermal escape processes can affect the transition of the upper atmospheres of planets from a hydrostatic to hydrodynamic state, when, for example, particle precipitations are accompanied by charge exchange between the planetary coronal gas and stellar wind plasma [28, 29, 39, 41]. Of particular importance is the transitional region between the thermosphere and exosphere, where the flux of particles escaping the atmosphere forms. Boltzmann kinetic equation describes the state of atmospheric gas in the transitional region because of the need to take into account the contribution of suprathermal particles produced in nonthermal processes [27, 33, 39, 42].

Presently, only a few models of HJ atmospheres [19–21, 23, 28, 43–45] allow the vertical density distributions of the main atmospheric components (H, H_2, He) to be set. The atmosphere models differ quite significantly, preventing a unique setting of the atmospheric composition. Moreover, even in the case of a correct determination of the initial distribution of the atmospheric components, when solving the atmosphere heating problem, its response to the additional heating should be taken into account, i.e., the problem should be solved self-consistently. The self-consistency requirement makes the problem nonlinear and demands more resources. The calculations presented below were performed in the transitional $H_2 \to H$ region in a hot Jupiter upper atmosphere in the altitude range of $(1-1.26)\,R_{pl}$, where R_{pl} is the planet's radius. It is in this altitude interval that the host star's extreme radiation and wind are predominantly absorbed. The lower boundary of the studied region was set at the lower atmosphere altitudes at which the atmospheric gas density is high enough to absorb virtually completely the energy fluxes from the star. The upper boundary was set in the upper atmosphere, where the gas collisional frequency vanishes. The typical hot Jupiter atmosphere was assumed to have H, H_2, and He distributions calculated in model [19] for the exoplanet HD 209458b; for Jupiter in the Solar System, the model from paper [32] was utilized. The number density height profiles of the main components and temperature for Jupiter and hot Jupiter HD 209458b are shown in Figs 2 and 3, respectively.

The density profiles are shown inside the atmospheric heating region caused by the host star's extreme radiation absorption and the stellar wind's charged particle degradation. The vertical height is in units of the planet's photometric radius R_{pl} (7.15×10^9 cm for Jupiter and 9.54×10^9 cm for the hot Jupiter HD 209458b), facilitating a comparison with other planets. The atmospheres of the typical hot Jupiter and

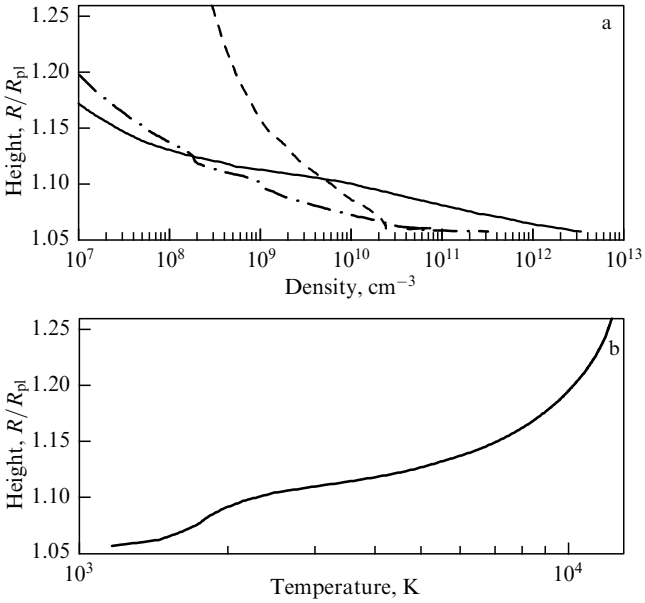

Figure 3. (a) Number density height profiles of molecular hydrogen (solid line), atomic hydrogen (dashed line), and helium (dashed-dotted line) in the atmosphere of the hot Jupiter HD 209458b according to model [19]. (b) Atmospheric gas temperature height profile. The height is in units of planet HD 209458b's photometric radius.

the Solar System's Jupiter differ significantly. In the Jovian atmosphere, H_2 dominates almost up to the upper boundary (i.e., the exosphere). In contrast, in a hot Jupiter, the atmosphere is very extended because of the high temperature, and, correspondingly, atomic hydrogen dominates. In both cases, the upper atmospheres are characteristic examples of hydrogen-helium atmospheres of gas giants.

Analysis of observations and modeling of exoplanet atmospheres interacting with host stars suggests, in particular, that, after planet formation, hydrodynamic outflow from the atmosphere, induced by soft X-ray and extreme UV heating from the star, occurs [36, 38]. When the star's extreme radiation decreases, the atmospheric escape changes from the thermosphere's hydrodynamic expansion to hydrostatic atmospheric evaporation [38]. During this transition, various nonthermal processes arise, which significantly contribute to the total atmospheric losses [39, 46]. After discovering an extended hydrogen envelope around the transiting hot Jupiter HD 209458b [11], several research groups independently worked out models [19–21, 23, 28, 43–45] to study the hydrodynamic atmospheric escape in hot Jupiters. Despite different details, all these models are in satisfactory agreement with observations of gaseous hydrogen envelopes around such planets. Still, they do not allow us to study the long-term history of an exoplanet orbiting close to the host star. The problem is mainly due to considerable uncertainties in the models, including the extreme UV flux from the star, the heating efficiency (conversion of absorbed radiation into heat), and the contribution from heavy elements. Similar to the impossibility of inverting time for studies of the evolution of the Solar System's planets, including atmospheric dissipation of Earth-like planets, it is impossible to understand a specific exoplanet's atmosphere formation but is still possible to compare features of similar planets at different evolutionary stages [36].

Heating by the host star is one of the critical factors determining the state of an exoplanet's atmosphere. It is

crucial for hot Jupiters. The first discoveries of HJs revealed that the atmospheres of some HJs overfill the Roche lobe, inducing a powerful atmospheric outflow [28, 29]. The heating of the upper hydrogen atmosphere is due to the absorption of X-ray and ultraviolet (XUV) radiation of the host star in the soft X-ray (X, 1–10 nm) and extreme ultraviolet (EUV, 10–100 nm) bands. The heating efficiency is defined as the total local atmospheric heating ratio to the stellar radiation absorption rate. This parameter is essential for the thermal dissipation of the upper atmospheres of the Solar System planets [39]. It is even more critical for exoplanets irradiated by host stars emitting extreme UV and soft X-rays [18, 26]. In this case, the heating is accompanied by the formation of a significant fraction of suprathermal particles — photoelectrons arising in the atmospheric gas ionization and suprathermal hydrogen atoms from molecular hydrogen dissociation, the main atmospheric component. Therefore, in studies of atmospheres of hot exoplanets, hot Jupiters in particular, nonthermal particles' contribution to the exoplanetary atmosphere aeronomy should be carefully assessed [27, 36].

Thus, observations and theoretical models of exoplanetary atmospheres, illuminated by the host star's extreme radiation flux, offer a remarkable opportunity to test the theoretical understanding of the key processes — thermal and nonthermal dissipation, affecting both the planet's evolution and atmosphere, the early Earth in particular. One may expect that future observations of exoplanets will yield more stringent constraints and improve the atmospheric dissipation models. Their application [36] enables clarifying the evolution of the exoplanetary atmosphere. This section discusses these key issues of the exoplanetary atmosphere aeronomy which are directly related to the evolution of giant planets closely orbiting the host stars — hot Jupiters. Special attention will be given to accounting for the contribution of suprathermal particles to the HJ atmosphere aeronomy.

2.1 Heating of hydrogen-dominated atmosphere by extreme stellar radiation

Atmospheric heating due to the absorption of the host star's extreme radiation in the 1–100 nm wavelength range essentially determines the state of the planetary atmosphere. The atmospheric gas absorbs this radiation in reactions of ionization of atomic hydrogen and helium and ionization, dissociation, and dissociative ionization of molecular hydrogen [47, 48]:

$$\mathrm{H_2} + h\nu, (\mathrm{e_p}) \to \begin{cases} \mathrm{H(1s)} + \mathrm{H(1s, 2s, 2p)} + (\mathrm{e_p}), \\ \mathrm{H_2^+} + \mathrm{e} + (\mathrm{e_p}), \\ \mathrm{H(1s)} + \mathrm{H^+} + \mathrm{e} + (\mathrm{e_p}), \end{cases} \tag{1}$$

$$\mathrm{H, He} + h\nu, (\mathrm{e_p}) \to \mathrm{H^+, He^+} + \mathrm{e} + (\mathrm{e_p}).$$

Here, part of the absorbed photon energy, equal to or exceeding the ionization or dissociation energy, is transformed into the internal energy of matter. The remaining part goes into the kinetic energy of the reaction products, mostly the kinetic energy of electrons. If an emerged photoelectron's energy is sufficiently high, photoelectron can participate in secondary ionization and excitation reactions with atmospheric components. The initial photoelectron can also lose energy into heat via elastic collisions. Thus, the energy of photoelectrons is partially transformed into internal energy and partially goes to heat the atmosphere.

Let $W_{h\nu}$ be the stellar radiation energy absorbed per unit time in a unit volume, W_{pe} be the initial kinetic energy of photoelectrons generated per unit time in a unit volume, and W_{T} be the energy of electrons transformed into heat per unit time per unit volume. Detailed expressions for $W_{h\nu}$, W_{pe}, and W_{T} are given in paper [26]. Then, the total heating efficiency coefficient will be calculated as

$$\eta_{h\nu}(z) = \frac{W_{\mathrm{T}}(z)}{W_{h\nu}(z)}. \tag{2}$$

The transport and kinetics of photoelectrons in the hydrogen- and helium-dominated upper atmosphere of an (exo)planet was calculated using a Monte Carlo model [47, 49] adapted to hydrogen atmospheres. In the day-side upper atmosphere, high-energy electrons are produced from photoionization of the main atmospheric components by soft X-ray and extreme UV stellar radiation. As noted above, the electrons in the upper atmosphere lose kinetic energy in elastic, inelastic, and ionization collisions with the main components of the surrounding atmospheric gas:

$$\mathrm{e}(E) + X \to \begin{cases} \mathrm{e}(E') + X, \\ \mathrm{e}(E') + X^*, \\ \mathrm{e}(E') + X^+ + \mathrm{e}(E_{\mathrm{s}}), \end{cases} \tag{3}$$

where E and E' are the primary electron kinetic energy before and after the collision, respectively, and X^* and X^+ are the atmospheric components in the excited and ionized states, respectively. Here, E_{s} is the energy of the secondary electron formed in the collision with subsequent ionization. The energy E_{s} is chosen according to the procedure described in papers [50–52]. Photoelectrons with suprathermal energies lose energy in collisions (3) with the ambient atmospheric gas. Energy spectra of the photo- and secondary electrons are strongly nonequilibrium [47, 49]. Correspondingly, the kinetics and transfer of the photoelectrons are described by Boltzmann equation:

$$\mathbf{v}\frac{\partial}{\partial \mathbf{r}} f_{\mathrm{e}} + \frac{\mathbf{Y}}{m_{\mathrm{e}}}\frac{\partial}{\partial \mathbf{v}} f_{\mathrm{e}} = Q_{\mathrm{e,\,photo}}(\mathbf{v}) + Q_{\mathrm{e,\,secondary}}(\mathbf{v}) + \sum_{M=\mathrm{H,\,He,\,H_2}} J(f_{\mathrm{e}}, f_M). \tag{4}$$

Here, $f_{\mathrm{e}}(\mathbf{r}, \mathbf{v})$ and $f_M(\mathbf{r}, \mathbf{v})$ are velocity distribution functions for electrons and the atmospheric gas components, respectively. The left-hand side of this equation describes the transport of electrons in the force field $\mathbf{Y}$ of the planet. On the right-hand side, the term $Q_{\mathrm{e,\,photo}}$ represents the formation rate of primary electrons, and the term $Q_{\mathrm{e,\,secondary}}$, the formation of secondary electrons from ionization by photoelectrons. The collision integrals for elastic and inelastic interactions of electrons with the surrounding atmospheric gas $J(f_{\mathrm{e}}, f_M)$ are written in the standard form, assuming that the atmospheric gas has a local equilibrium Maxwell velocity distribution.

Papers [47, 49] give a detailed description of the Monte Carlo realization of the transport of photoelectrons in planetary atmospheres. Note, however, that this realization has used experimental and theoretical cross sections and scattering angles in elastic, inelastic, and ionization collisions of electrons with $\mathrm{H_2}$, He, and H taken from the following sources: (a) for $\mathrm{e} + \mathrm{H_2}$ collisions, from the AMDIS database (https://dbshino.nfs.ac.jp) and paper [53]; (b) for $\mathrm{e} + \mathrm{He}$

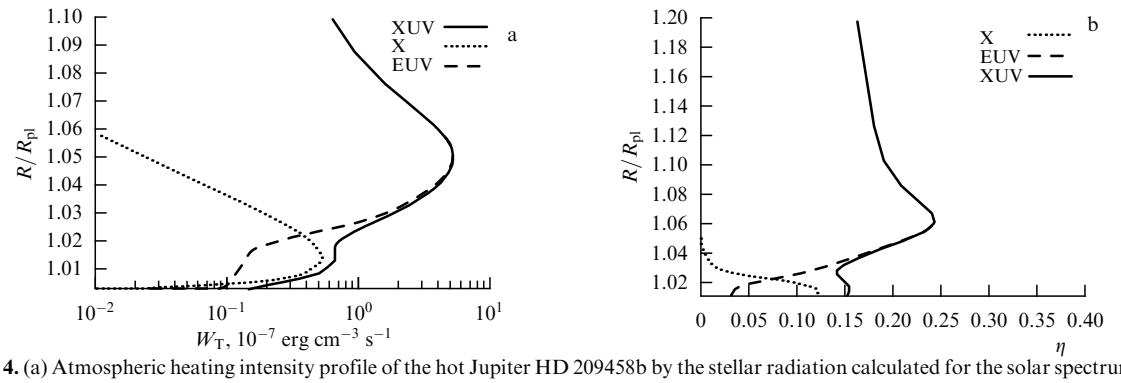

Figure 4. (a) Atmospheric heating intensity profile of the hot Jupiter HD 209458b by the stellar radiation calculated for the solar spectrum and separately for the X-ray and extreme UV ranges. The dotted line shows the heating efficiency by the X-ray radiation, the dashed line, by the extreme UV radiation. The solid line shows the heating by radiation with the total XUV solar spectrum for the exoplanet HD 209458b at a distance of 0.045 a.u. from the host star. (b) Total heating efficiency for the basic XUV model (solid line) and its components: the EUV model (dashed line) and the X model (soft X-ray range, dotted line). Here, R_{pl} is the planetary radius [60].

and e + H collisions, from the NIST database (http://physics.nist.gov/PhysRefData/Ionization/) and papers [51, 54].

Reactions taking into account suprathermal electrons reduce the actual heating efficiency below unity. However, most papers exploring the atmospheric outflow efficiency (see, e.g., review [26]) adopt the heating efficiency coefficient equal to one. Recently, paper [55] investigating the evaporation efficiency of the hydrogen atmosphere of the planet KIC 12557548b arbitrarily proposed a heating efficiency of 0.5. In paper [21], the total heating efficiency was arbitrarily assumed to be $\eta_{h\nu} = 0.32$. In more detailed studies (e.g., [19]), the heating efficiency is shown to vary within the range of 0.4–0.6 at distances $\sim (1.03-1.05)R_{pl}$, being ~ 0.2 at $\sim 1.4R_{pl}$ and ~ 0.15 at distances $> 1.4R_{pl}$. Based on these investigations, some authors assume it to be 0.3, in agreement with results [56] obtained for the early Earth's hydrogen atmosphere outflow. These values are close to estimates $\eta_{h\nu} = 0.15-0.3$ [57] obtained for the hydrodynamical outflow of early Venus's upper atmosphere. Paper [58] adopted the heating efficiency of 0.1, 0.3, 0.5, 0.8, and 1. Here, the temperature changed within the range of 6000–8000 K. Note that paper [58] ignored molecular hydrogen ionization. Yet, dissociative ionization processes significantly contribute to atmospheric heating. In addition, in this model, the computation domain lower boundary does not correspond to the thermosphere lower boundary.

In recent years, several studies of atmospheric outflows of super-Earths and sub-Neptunes in the system Kepler-11, the planet GJ 1214b, and other sub-Neptunes have been carried out. These studies used the heating efficiency in the range of 0.1–0.4. About the same extremal values, 0.15 and 0.4, were used in papers [43, 59], which explored the hydrogen envelope outflow in early Mars, super-Earths, and sub-Earths from the habitability zone around solar-type G stars with extreme-UV fluxes 100 times as high as from the Sun, and in five exoplanets in Kepler-11, intermediate between super-Earths and sub-Neptunes.

This brief review points to very different heating efficiencies between 0 and 1. Nevertheless, the wrong estimate of this parameter can alter the mass-loss rate by an order of magnitude. Therefore, calculating the efficiency of heating hydrogen atmospheres by soft X-rays and extreme UV radiation is very topical. We have calculated the heating efficiency of the planet atmosphere around HD 209458b by assuming an approximate solar radiation spectrum [26]. These calculations are valid only for a contemporary planetary atmosphere irradiated by a star with an age of four billion years. Papers [26, 60] investigated the temperature distribution of a primary atmosphere enriched with molecular hydrogen and affected by intensive XUV solar/stellar radiation. It was shown that high ionization and photochemistry rates ultimately lead to the heating and subsequent expansion of the upper atmosphere and the formation of suprathermal atoms, which can also affect the energy balance in the planet's thermosphere (Fig. 4). Papers [26, 60] suggest that the heating efficiency of the hydrogen-dominated upper atmosphere of a planet by extreme radiation does not exceed 0.2 at the thermosphere level if photoelectron effects are taken into account.

Meanwhile, stellar X-ray and UV radiation fluxes change significantly during stellar evolution. This is because the stellar rotation gradually decreases, thus weakening stellar activity determining short-wavelength radiation spectral intensity. Accordingly, atmospheric heating should change in the course of stellar evolution. Figure 1.8 of review [61] demonstrates average variations of the UV and X-ray flux for stars of different ages. For young stars, the 0.1–120-nm flux is much higher than the solar one. Nevertheless, the intensity can differ by several orders of magnitude in different bands. For example, for stars with an age of 0.1 bln years, the 0.1-nm flux is about 2000 times as high as the solar one, whereas the 100-nm flux from stars of the same age is only 30 times as high as the solar one. The flux depends strongly nonlinearly on frequency. For all EUV frequencies, the flux increases at about the same rate as the stellar age decreases. The 1–2-nm flux increases at a rate several orders of magnitude higher. In particular, the flux ratio for EK Dra stars with an age of 0.1 bln years and β Hyi with an age of 6.7 bln years is 20,000 at 1 nm, 200 at 10 nm, and only 50 at 100 nm.

Thus, to decide on the atmospheric stability of hot Jupiters on a cosmological timescale, we should understand how the atmospheric heating changes with stellar spectrum evolution.

2.2 Extreme stellar radiation effect on heating efficiency

Consider the exoplanet HD 209458b, a transit hot Jupiter that has been extensively observed and whose atmosphere has been modeled many times. The extreme spectrum of HD 209458 is thought to be similar to that of the Sun. It is shown in Fig. 5. The shaded region indicates the soft X-ray emission whose intensity changes with stellar age.

In this model, the energy transfer rate is calculated for stellar radiation and photoelectrons into the internal energy

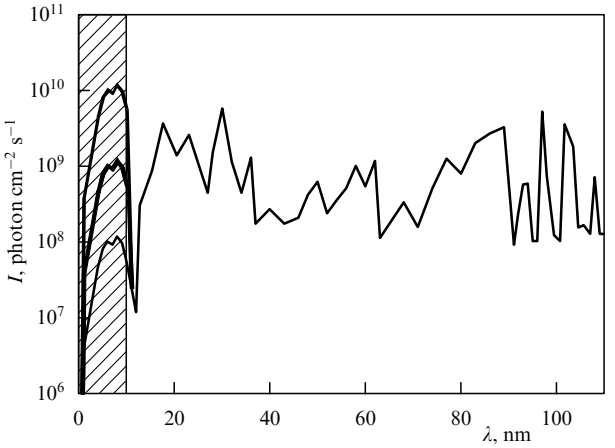

Figure 5. Radiation flux at different wavelengths for all three variants of the utilized spectrum. The shaded region indicates the soft X-ray range (wavelengths of 1–10 nm). Thick solid lines show spectra with a 10-fold and 100-fold increase in soft X-ray flux.

in each photolytic reaction (1) and photo- and secondary electron reactions (3). The energy of suprathermal photoelectrons transferred into thermal energy is calculated separately. Thus, the results of modeling enable us to determine the general heating efficiency and the efficiency of heating by photoelectrons and to understand which processes mainly influence atmospheric heating.

As noted above (see also [61]), the X-ray flux from young stars exceeds the solar value by a factor of several thousand, whereas the extreme UV flux is only a dozen times as high. Therefore, the extreme UV flux in the 10–100-nm range in all models below was constant (the EUV model), but exceeded by a factor of 10 (model 10X) and 100 (model 100X) the 1–10-nm flux. Therefore, the solar spectrum recalculated for the distance to the studied planet from the star ($r = 0.045$ a.u. for HD 209458b) was utilized as the basic model (XUV).

Figure 6 shows intensities of the stellar radiation absorption $W_{h\nu}$ (Fig. 6a) and the atmospheric gas heating W_{T} (Fig. 6b) for models 1X (solid line), 10X (dashed line), and 100X (dashed-dotted line). It is seen that the UV and X-ray radiation is absorbed at different heights, which results in two maxima for the basic model. The UV radiation is absorbed at the height of $1.05\,R_{\mathrm{pl}}$, where R_{pl} is the planetary radius. The soft X-ray radiation is absorbed at $1.015\,R_{\mathrm{pl}}$. The results presented below also suggest that the X-ray intensity increase leads to a growth of the corresponding heating intensity profile at the height of $1.015\,R_{\mathrm{pl}}$. For model 10X, both peaks have almost the same value, and for model 100X only one maximum with enhanced amplitude remains at low altitudes. Thus, with changing stellar spectrum, the heating intensity profile changes dramatically. If, for a low short-wavelength intensity, the heating occurs at the height of $1.05\,R_{\mathrm{pl}}$, a 100 times higher radiation intensity heats the atmosphere almost at the photometric radius of the planet. Despite the fact that the maximum heating moves inside by only $0.04\,R_{\mathrm{pl}}$, it can substantially change the energetic balance of the atmosphere due to the exponential dependence of the gas density on height.

As seen from Fig. 7, the heating efficiency somewhat decreases with increasing X-ray flux. This can be understood by considering partial heating efficiencies calculated separately for the soft X-rays and extreme UV (EUV) band presented in Fig. 4b. In that plot, the dashed line shows

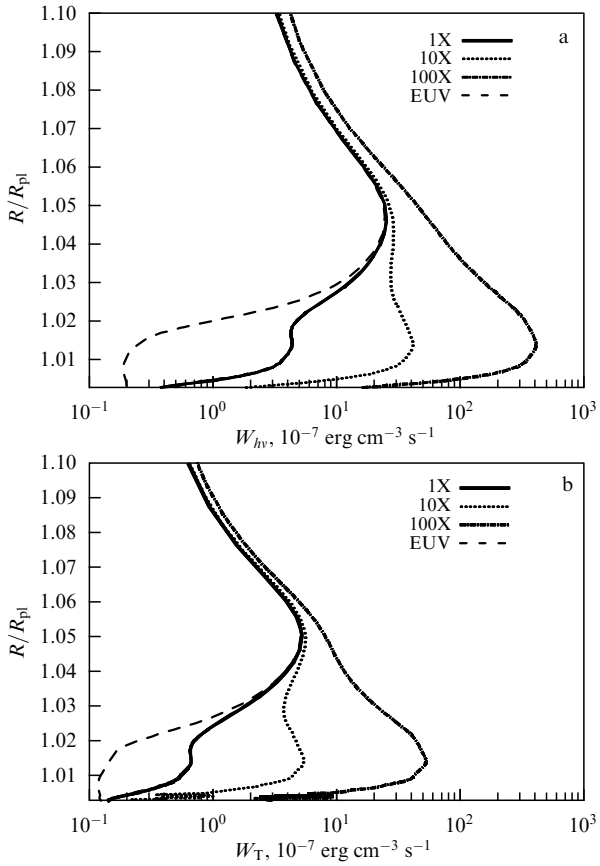

Figure 6. Absorption intensity $W_{h\nu}$ of the stellar radiation (a) and the atmospheric gas heating W_{T} (b) for models 1X (solid line), 10X (dotted line), and 100X (dashed-dotted line), and EUV (dashed line).

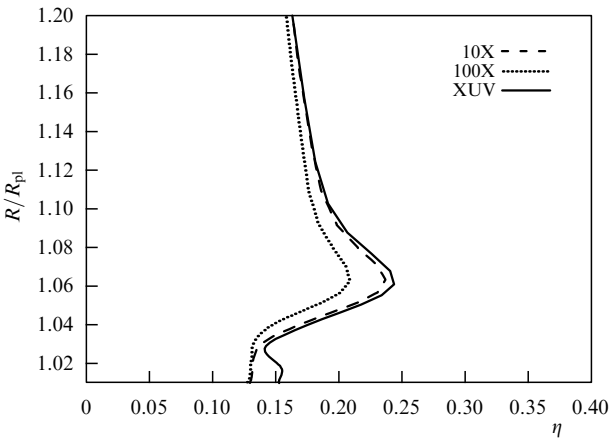

Figure 7. Total heating efficiency of the hydrogen-dominated planetary upper atmosphere for models 1X = XUV (solid line), 10X (dashed line), and 100X (dotted line).

the partial heating efficiency for the model EUV spectrum (i.e., $W_{\mathrm{T}}^{(\mathrm{EUV})}(z)/W_{h\nu}(z)$), and the dotted line indicates the partial efficiency for the model X (soft X-ray spectrum $W_{\mathrm{T}}^{(\mathrm{X})}(z)/W_{h\nu}(z)$); here, $W_{\mathrm{T}}^{(\mathrm{EUV})}(z) + W_{\mathrm{T}}^{(\mathrm{X})}(z) = W_{\mathrm{T}}(z)$. The efficiency of the atmospheric gas heating by soft X-rays is lower than by EUV radiation or by the basic XUV spectrum. Correspondingly, when the fraction of the soft X-ray radiation in the parent star spectrum increases, the heating efficiency profile approaches model X; that is, the total heating efficiency decreases.

The heating efficiencies calculated for the solar spectrum can be applied to stars younger than the Sun after the corresponding correction of the soft X-ray and extreme UV spectral contributions [61]. A complete picture of the irradiation spectral effects on the atmospheric structure and dynamics requires gas-dynamic modeling of the atmosphere and chemical reactions in the gas.

2.3 Heating by electron precipitation into the exoplanetary upper atmosphere

The correct treatment of the heating processes is greatly needed to construct atmospheric models (see, e.g., [19, 20, 23, 58]). At the same time, due to an insufficient understanding of interaction mechanisms between the stellar wind and exoplanet atmospheres, one has to use some simplifying assumptions. This, in turn, can result in noticeable deviations of the derived atmospheric parameters from real ones.

Improving physical processes, which are taken into account in the model atmospheres, is laborious work and needs to be further developed. However, the formulation of a complete list of physical processes should be considered when constructing model atmospheres of giant exoplanets. One of the possible shortcomings in modern models of exoplanetary atmospheres is ignorance of the precipitation of magnetospheric electrons. The importance of this process is quite straightforward for Jupiter in the Solar System. In Jupiter, according to the accepted estimates [62–64], the precipitation of magnetospheric electrons significantly contributes to (and even determines) the total energy balance in the upper atmosphere at high latitudes. There are two reasons for this: (1) Jupiter's significant magnetic field, which can effectively accelerate electrons (see, e.g., [65]), leading to the injection of high-energy electrons [66]; (2) the high total flux of electrons due to plasma inflow from Io [67].

The contribution of the precipitating electrons to the atmospheric heating of hot Jupiters has not been considered so far, although their contribution can be significant. Observations and theoretical estimates suggest that hot Jupiters can have an own magnetic field. Synchronization of the proper rotation of the planet with orbital revolution makes the magnetic dynamo generation ineffective, and the dipole moment of the own magnetic field is relatively weak. Nevertheless, its value turns out to be quite sufficient to create noticeable magnetospheric effects. For a more detailed discussion of the value and configuration of the own magnetic field of hot Jupiters, see Section 4.1 below. Estimates in paper [68] suggest that the magnetic field in hot Jupiters can attain one-tenth of Jupiter's magnetic moment, and electrons can be accelerated to high energies. In addition, the high atmospheric temperature, accompanied by atmospheric evaporation and/or gas-dynamic outflow, can lead to a significant plasma inflow in the magnetosphere (see, e.g., estimates of the electron density in papers [58, 69, 70]). Thus, it is very probable that the contribution of magnetospheric electrons to the atmospheric heating of hot Jupiters can be significant.

In this section, we consider the kinetics of the precipitation of electrons with different energies into the atmosphere of the typical hot Jupiter and compare them with calculations for the planet Jupiter. To perform the calculations, we use our modified numerical code [49, 71, 72] based on the solution to Boltzmann equation for high-energy electrons by the kinetic Monte Carlo method. The model is 1D, because we consider the motion of high-latitude electrons along open magnetic field lines. This approximation is valid for a dipole magnetic field and the high-latitude upper atmosphere of a giant planet. The partial and total rates of energy loss and heating of the atmospheric gas by the flux of electrons penetrating the upper planetary atmosphere are defined by the standard formulas based on the calculated distribution functions $f_e(\mathbf{r}, \mathbf{v})$ of electrons [49]. This approach enables us to consider the process of electron penetration into the atmosphere correctly, calculate the flux of electrons moving up and down, and estimate the total energy deposit into the atmosphere and atmospheric heating efficiency. To optimize the further use of these results, all calculations are performed for a unit energy flux of the precipitating electrons (1 erg cm^{-2} s^{-1}). For a given exoplanet, all results should be scaled by considering the actual flux of electrons in each specific case.

Characteristics of the flux of precipitating electrons are unclear. Our calculations have assumed that hot Jupiters can have a significant magnetic field, up to one-tenth of Jupiter's [68]. According to theoretical estimates, electrons can be accelerated to high energies in a dipole field (see, e.g., [65]). The precipitation of high-energy electrons is confirmed by observations of Jupiter by the Hubble Space Telescope [66, 67]. Taking into account the above considerations, we have investigated three typical cases of the precipitation of electrons with a Maxwellian velocity distribution for the characteristic energies $E_0 = 1$, 10, and 100 keV. The Maxwellian velocity distribution is supported by numerous measurements of electrons precipitating into Earth's magnetosphere (see, e.g., [73]).

The model atmospheres of HJs [19–21, 23, 28, 43–45] are highly different, which does not allow us to define the atmospheric composition unambiguously. Moreover, if the initial atmospheric components are correctly determined, when calculating the atmospheric heating, one needs to take into account its additional heating, i.e., the problem should be solved self-consistently. We aim to study the importance of precipitation of magnetospheric electrons for atmospheric heating; therefore, we have treated the problem in the linear approximation. In this case, the total electron energy flux is low, only about 1 erg cm^{-2} s^{-1}, which, in turn, enables us to assume that the initial radial profiles of the H, H_2, and He atmospheric components remain constant.

The calculations were carried out in the transitional $H_2 \rightarrow H$ region of the upper atmosphere of a hot Jupiter, in the altitude range of $(1-1.26)\,R_{pl}$. The lower boundary of the studied region was usually defined in the low thermosphere layers, where the atmospheric gas density is sufficiently high to absorb almost completely the energy of the precipitating electrons. The upper boundary was set in the upper atmosphere region, where the electron collision rate with the atmospheric gas is low. In the calculations, we have used neutral atmospheres of the Solar System's Jupiter and the hot Jupiter HD 209458b presented in Figs 2 and 3, respectively. The density distributions are given in the region where the injecting electron flux mostly degrades to heat the atmosphere. The height along the ordinate axis is in units of the photometric radius of the planet, facilitating a comparison of calculations with different planets. In the Jovian atmosphere, H_2 dominates almost up to the upper boundary (i.e., exosphere). In contrast, in a hot Jupiter, the atmosphere is more extended due to high gas temperature, and atomic hydrogen dominates.

The results of calculations for the Solar System's Jupiter and the hot Jupiter HD 209458b are presented in Figs 8 and 9,

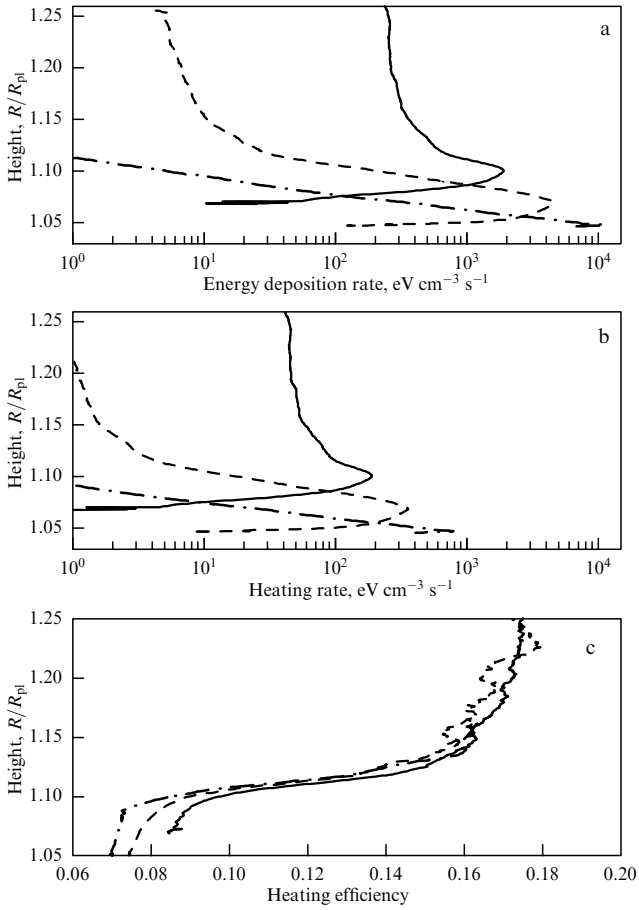

Figure 8. (a) Energy deposition rate of auroral electrons by collisions with atmospheric gas. (b) Atmospheric gas heating rate by collisions with auroral electrons. (c) Atmospheric gas heating efficiency by precipitating electrons. Auroral electrons precipitate with a Maxwellian distribution with $E_0 = 1$ keV (solid line), 10 keV (dotted line), and 100 keV (dashed-dotted line) into the atmosphere of the hot Jupiter HD 209458b.

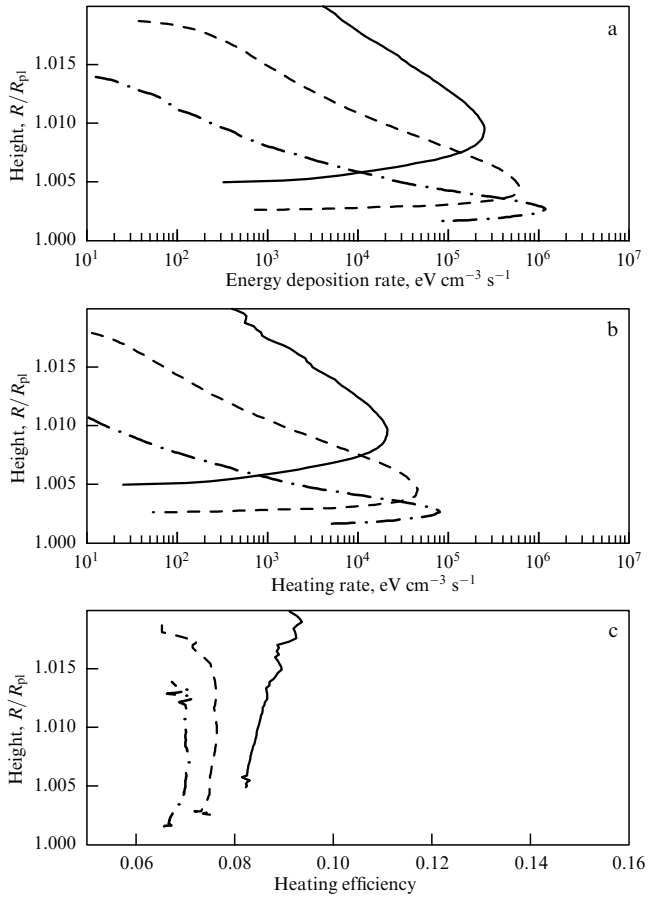

Figure 9. (a) Energy deposition rate of auroral electrons by collisions with atmospheric gas. (b) Heating rate of atmospheric gas by collisions with auroral electrons. (c) Heating efficiency of atmospheric gas by precipitating electrons. Auroral electrons precipitate with a Maxwellian distribution with $E_0 = 1$ keV (solid line), 10 keV (dotted line), and 100 keV (dashed-dotted line) into the Jovian atmosphere in the Solar System.

respectively. Figures 8a and 9a show the altitude profiles of the energy deposition rate of auroral electrons due to atmospheric absorption for three fluxes of precipitating electrons with the characteristic energy $E_0 = 1$ (solid curve), 10 (dashed curve), and 100 keV (dashed-dotted curve). Figures 8b and 9b show the altitude profiles of the atmospheric gas heating rate by injecting electrons (the notations are the same as in Figs 8a and 9a). Figures 8c and 9c show the altitude profiles of the atmospheric heating efficiency, i.e., the ratio of the energy spent to heat to the energy deposit at a given altitude (the notations are the same as in Figs 8a and 9a).

As expected, for both planets considered, with increasing energy of precipitating electrons, the peaks in absorption (deposition) and general and thermal energy shift downwards (more deeply into the atmosphere), and their absolute values increase. However, the absolute values of the energy of electrons absorbed by the atmosphere are appreciably different for different planets. For example, in the hot Jupiter, the deposition peak for the injecting electron energy $E_0 = 10$ keV corresponds to 5×10^3 eV cm^{-3} s^{-1} at a height of $1.065\,R_{pl}$, and for Jupiter, to 6×10^3 eV cm^{-3} s^{-1} at a height of $1.004\,R_{pl}$. A comparison of the obtained results indicates that, in the hot Jupiter, in addition to the decrease in the peak of energy absorbed by the atmosphere, the deposition of electron energy occurs in a more extended region of the thermosphere, and the atmospheric heating efficiency significantly increases.

The results of calculations for the typical hot Jupiter and the Solar System's Jupiter suggest that the heating efficiency weakly depends (does not depend) on the characteristic energy of injecting electrons. For the upper Jovian atmosphere, the heating efficiency is independent of the altitude and lies within the range of 7–9%. For the hot Jupiter, the heating efficiency has a significant dependence on height — it varies from 8 to 17%. Importantly, in hot Jupiters, the energy deposition rate peaks for electrons with low kinetic energies fall in the region with a higher heating efficiency, which can significantly enhance the contribution of the precipitating electrons to the total atmospheric heating.

2.4 Aeronomic model of a hot Jupiter taking into account suprathermal particles

In this section, we present a self-consistent aeronomic model of the upper atmosphere of a hot Jupiter, including reactions with the participation of suprathermal photoelectrons. The model is applied to the planet HD 209458b to calculate the gas density, velocity, and temperature altitude profiles. It is shown that taking into account the suprathermal electrons in the heating and cooling functions significantly decreases

the atmospheric gas outflow rate in the hydrodynamic regime.

Various authors have performed gas-dynamic modeling of the outflow from the atmosphere of HD 209458b [18–21, 23, 28, 43–45], taking into account chemical reactions. In these studies, a system of one-dimensional gas-dynamical equations has been solved. The main difference among the published models relates to the atmospheric composition and boundary conditions. In paper [19], the atmosphere was assumed to consist of atomic hydrogen, molecular hydrogen, and helium. Papers [20, 58] take into account the presence of admixtures. The authors of paper [58] include C, C^+, O, O^+, N, N^+, Si^+, Si, Si^{2+} in the model but assume no molecular hydrogen in the upper atmosphere. Paper [20] also takes into account molecules, including C, O, N, D. The free gas outflow is usually chosen as the outer boundary condition, which extrapolates the gas-dynamic parameters at the outer boundary from adjacent cells. In model [20], the pressure is set at the outer boundary. Usually, a fixed boundary condition is posed at the lower boundary [19, 20], although paper [58] uses the matter inflow condition. The results obtained in these studies show that the upper atmosphere can be heated to temperatures above 10,000 K, despite an equilibrium temperature of this planet of 1300 K. These models reproduce the matter outflow from the exoplanet HD 209458b, which is estimated to be 10^{10} g s^{-1} from observations [11, 18].

As noted above, models based exclusively on gas-dynamic equations prove not to be precise enough to describe the heating of the upper atmosphere, where the particle velocity distribution can differ from the Maxwellian one [27]. The main reason for the gas-dynamic outflow from atmospheres of hot Jupiters may be heating by stellar radiation [18, 20, 21, 23, 28, 43–45] in the 1–100-nm range (XUV-radiation), which is absorbed in reactions of ionization of atomic hydrogen and helium and ionization, dissociation, and dissociative ionization of molecular hydrogen [26, 47, 60].

In papers [18–21, 23, 28, 43–45], the role of photoelectrons in the heating process is taken into account by adjusting the coefficient called the heating efficiency. From the physical viewpoint, the heating efficiency shows the proportion of XUV radiation absorbed by the atmosphere that comes into the heating. The heating efficiency varies from 0 to 1 in different studies. To determine it precisely, one should compute the kinetics of photoelectrons (see Sections 2.1 and 2.2). A complex self-consistent model including the dynamics of suprathermal particles, chemical reactions, and gas dynamics is needed to calculate the dynamics of a hot Jupiter's atmosphere.

The self-consistent aeronomic model of the upper atmosphere of a hot Jupiter accounting for suprathermal photoelectrons includes a Monte Carlo module, a chemical module, and a gas-dynamic module. In the Monte Carlo module, the atmospheric heating intensity is calculated based on the atmosphere's neutral components' initial distributions and ionization rates, dissociation, and excitation of the atmosphere's components. In the gas-dynamic module, the macroscopic characteristics of the atmosphere (density, velocity, temperature) are computed from the heating rate.

To calculate the transport and kinetics of photoelectrons in the upper atmosphere of an exoplanet dominated by hydrogen and helium, the Monte Carlo model [47, 49] adapted to hydrogen atmospheres was used. The model includes collisional reactions (3) and the transport of suprathermal electrons in the atmosphere. As mentioned above, the kinetics and transport of photoelectrons are described by Boltzmann equation (4). This module computes the transfer rate of radiation and photoelectron energy into internal energy in each photolytic reaction (1) and collisional reactions of secondary electrons (3). The energy of suprathermal electrons transferring into the thermal energy is calculated separately. Thus, the results of the modeling enable the atmosphere heating function to be calculated.

In the chemical module, the system of chemical kinetic equations is solved. The network of reactions includes 19 reactions with the participation of 9 components: H, H_2, e^-, H^+, H_2^+, H_3^+, He, He^+, and HeH^+. The reaction rate constants are taken from paper [20]. As the resulting system of differential equations is stiff, DVODE software is used. The principal radiative cooling is due to H_3^+ ion radiation. The H_3^+ ion radiation intensity as a function of temperature is taken from paper [50]. It is used to compute the cooling function.

The gas-dynamic module is based on the numerical code described in paper [74]. Originally, this code was created to calculate protostellar cloud collapses. We have adapted it for planetary atmospheres. The model solves a one-dimensional spherically symmetric adiabatic system of gas-dynamic equations with the equation of state of a perfect gas [75]. To solve the system, we use an implicit fully conservative finite difference scheme described in book [76]. The calculation is performed on a Lagrangian grid, i.e., having moving cell boundaries, because the atmospheric density falls exponentially with radius; the use of a variable grid uniform on the mass results in much smaller cells near the planet's surface than in the upper computational domain. This decreases the time step determined from the Courant condition. Thus, the uniform grid leads to a slow computational speed and low spatial resolution in the upper atmosphere, where the main processes occur. The numerical method used in paper [74] was modified for computations on a nonuniform grid to solve this problem. We have used a coordinate grid nonuniform over mass: the cell mass decreases with altitude in a geometrical progression. The progression index was chosen empirically to be 0.986. An artificial viscosity was introduced into the scheme to suppress oscillations in the upper atmospheric layers. The viscosity was taken to be minimal to suppress nonphysical oscillations. At each time step of the gas-dynamic module, the thermal energy and pressure are recalculated, taking into account the heating and cooling functions obtained in the chemical and Monte Carlo modules. This approach is widely used and is known as the method of splitting by physical processes.

We chose the following initial conditions: the atmosphere is considered to be isothermal with a temperature of 1300 K corresponding to the equilibrium temperature at a distance from the star equal to the large orbital semi-axis of planet HD 209458b. The atmospheric density is taken to be barometric; the gas velocity is zero. The lower boundary of the computational domain is firmly fixed at a distance of one planetary radius; the reflection conditions are set at the lower boundary. The upper boundary is not fixed; that is, it can expand or contract during modeling. The pressure, equal to the stellar wind gas pressure at the corresponding orbital distance, is the outer boundary condition. For the stellar wind parameters taken from [77], the external pressure is $p_{ex} = 1.6 \times 10^{-6}$ dyn cm^{-2}. Initially, the atmosphere consists of molecular hydrogen and helium, with the helium mass proportion equal to 0.15. The total mass of the atmosphere

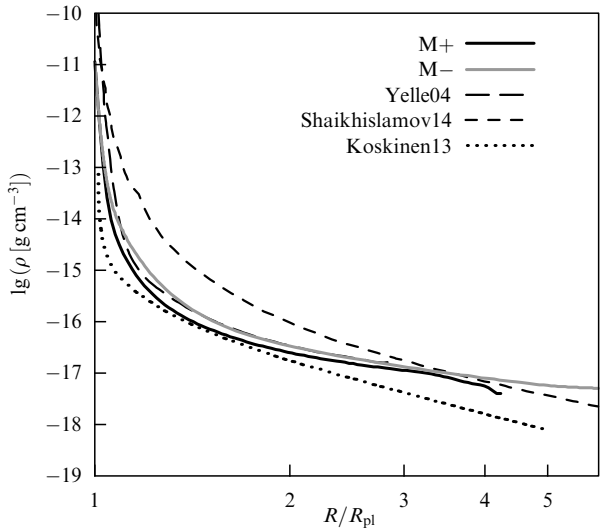

Figure 10. Density height profiles for models M+, M−, Koskinen13, Shaikhislamov14, and Yelle04.

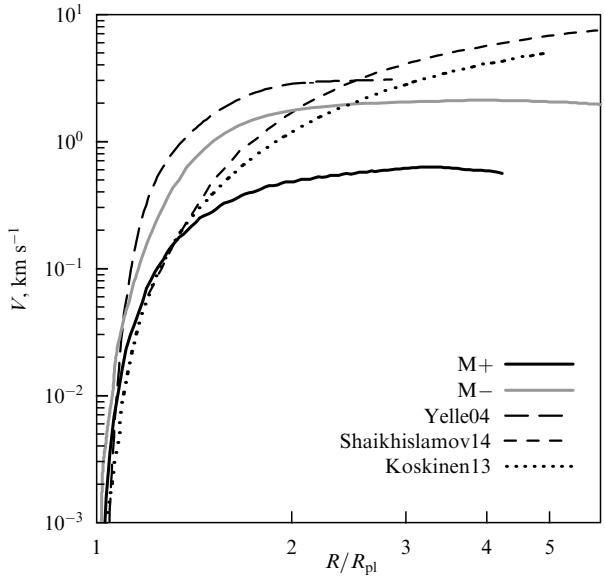

Figure 11. Mass velocity height profiles for models M+, M−, Koskinen13, Shaikhislamov14, and Yelle04.

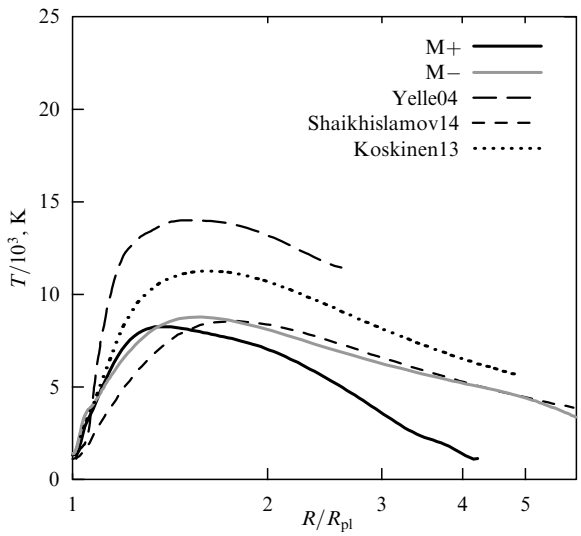

Figure 12. Temperature height profiles for models M+, M−, Koskinen13, Shaikhislamov14, and Yelle04.

is one of the input parameters. It was chosen such that the part of the atmosphere heated by XUV radiation enters into the computational domain. In our case, the atmospheric mass is 1×10^{18} g. The initial density at the lower boundary is 7×10^{11} cm^{-3}. The UV spectrum of the star is assumed to be the modern solar one taken from paper [78] and recalculated for a distance of 0.045 a.u. The calculations were performed until the stationary regime was reached. As the model is one-dimensional, we have approximated the three-dimensional Roche potential by the gravitational potential along the line connecting centers of the star and the planet.

Depending on the upper atmosphere's composition and the heating efficiency, the escape regime can change from hydrostatic to hydrodynamic. In order to investigate this problem, we have modeled the planetary atmosphere of HD 209458b with the simplified Roche potential and studied the effect of reactions with suprathermal photoelectrons on the dynamics, the change in the chemical composition, and the outflow rate of the hydrogen-helium atmosphere of the hot Jupiter HD 209458b [75]. The calculations were performed for two models: taking into account (M+) and ignoring (M−) photoelectrons. We have compared our results with those obtained by other authors; the results of papers [19, 58, 23] are denoted in the plots as model Yelle04, Koskinen13, and Shaikhislamov14, respectively.

Figures 10–12 show the calculated radial profiles of the temperature, velocity, and density for all the models compared. As the inclusion of suprathermal particles decreases the heating efficiency, one can expect that taking them into account will significantly decrease the atmospheric temperature and gas velocity, because the gas is accelerated by heating. Figure 10 compares the density profiles for M+ and M− models with models by other authors. It turns out that photoelectrons strongly affect the density profile, and all curves in this figure significantly differ, especially in the upper atmosphere.

The velocity profiles, shown in Fig. 11, also qualitatively repeat those obtained by other authors. Still, our model, which considers the contribution from photoelectrons, demonstrates lower outflow velocities of the atmospheric gas. Only at high altitudes do the models Koskinen13 and Shaikhislamov14 show velocities exceeding that in model M−. For such a variable as velocity, the difference between models M+ and M− is especially large. The gas velocity in the model without photoelectrons turns out to be several times as high.

It is seen that the results of our calculations are in qualitative agreement with other models only for model M−, i.e., without rigorously taking into account the contribution of suprathermal particles: photo- and secondary electrons. The altitude temperature profile for models M+ and M− and other authors' results are presented in Fig. 12. As expected, taking into account photoelectrons leads to an atmospheric temperature decrease, and the difference between the two models increases with radius. In model M−, the maximum temperature is about 9000 K; the effect of the suprathermal particles decreases it to 6000 K. Among the three models with which we have compared our results, the best agreement is observed for Shaikhislamov14. The temperature in models Yelle04 and Koskinen13 is higher by several thousand K. However, the temperature maximum

in all models lies at the same distance from the center, $(1.3-1.5)R_{\rm pl}$. The calculations show that the heating rate of the atmospheric gas is significantly different in models M+ and M−, which leads to different atmospheric gas temperatures (see Fig. 12) and, consequently, different gas loss rates.

The gas density and velocity at a specific radius R enable us to estimate the atmospheric outflow rate using the formula $\dot{M}(R) = 4\pi\rho(R)v(r)R^2$. The calculated outflow rate does not change above $1.2\,R_{\rm pl}$. The calculations yielded the atmospheric mass loss rate, which was compared with the results by other authors and observations. Namely, the estimate of $\sim 10^{10}$ g s^{-1} [11] was inferred from the Hubble Space Telescope (HST) observations; the estimates 4×10^{10} and 7×10^{10} g s^{-1} were obtained in gas-dynamic models [23] and [58], respectively; and our models M− and M+ yielded 4×10^{10} and 8×10^{9} g s^{-1}, respectively. Despite differences in the model details (the completeness of the physical model, numerical methods of the solution, the assumed basic atmospheric components, and the chemical complexity of the medium), all these models satisfactorily correspond to observations of the hydrogen cloud around the hot Jupiter HD 209458b. From the evolutionary point of view, what is most interesting is that the model hydrogen loss rates obtained coincide with each other within a factor of a few. Taking into account photoelectrons in model M+ decreases the outflow rate estimate several-fold, which could be one of the reasons for the incomplete loss of the primordial hydrogen-dominated atmosphere by exoplanets. Papers [28, 29, 70] suggest that the regime and rate of atmospheric outflow are determined by both the state of the atmosphere and the stellar wind parameters. Therefore, the obtained atmospheric parameters can be used as boundary conditions for three-dimensional gas-dynamic simulations modeling the interaction of the planetary atmosphere with the stellar wind.

It is seen that thermal and nonthermal particle escape can affect the transition of upper atmospheres from the hydrostatic to the hydrodynamic regime. Correspondingly, it is necessary to study in more detail the ratio of the incident stellar XUV radiation flux to the escape velocity from the planetary atmosphere, which determines the escape efficiency. Namely, taking into account in detail both energy fluxes transformed by the atmospheric chemical processes and the energy transported inside the thermosphere by suprathermal particles, photo- and secondary electrons are needed. Correspondingly, as was demonstrated in the aeronomic model M+, the calculation of the heating efficiency taking into account suprathermal particles will be more complicated [27, 79]. Yet such models enable an adequate investigation of the cosmogony of the exoplanetary atmosphere formation and loss.

3. Gas dynamics of envelopes of hot Jupiters

Observations demonstrate the signatures of extended gas envelopes around hot Jupiters. For example, observations of planets HD 189733b [80] and WASP-12b [16, 81] revealed an intriguing phenomenon — the noncoincidence of the beginning or end of the transit at different wavelengths — which was discovered in 2009 by Fossati [16] in Hubble space telescope observations of the transit of WASP-12b in the UV range. In some light curves, the transit beginning precedes that in the optical range by about 50 min, suggesting an absorbing material in front of the planet at a distance of about 4–5 radii. To explain this phenomenon, a possible mass outflow from the planet to its star was proposed [82, 83]. It is assumed that the planetary atmosphere can overflow the planet's Roche lobe. Papers [28, 29] put forward the idea that quasi-stationary envelopes can result from the interaction of matter outflowing from the planet with the stellar wind. Due to the supersonic flow around the envelope, a bow shock should arise. The bow shock is also possible because of the proper planetary magnetic field [84–86]. However, the last hypothesis requires a significant magnetic field, which is difficult to explain in the typical synchronous rotation of hot Jupiters with the star.

Generally, the presence of extended envelopes around hot Jupiters is firmly established. At the same time, theoretical explanations of the formation of such envelopes use different assumptions: charge exchange [18], radiation pressure [70, 80], mass transfer onto the star [82, 83], a proper magnetic field [84–86], and the formation of quasi-closed envelopes due to outflow from the L_1 vicinity and interaction with the stellar wind [28, 29]. This renders studies of such envelopes interesting from the point of view of the interpretation of observations and fundamental physics. The correct model will explain the envelopes' observed properties and investigate the parent star, which is inaccessible by direct measurements. The model can also probe the magnetic field of the star and stellar wind properties. It should be stressed that the study of gas-dynamic envelopes of exoplanets is a novel problem but, on the other hand, can be considered as a marginal case of mass exchange in a binary system. The gas dynamics of close binaries is a classical astrophysical problem, and there are many models for solving it. In our studies of exoplanets, we utilize gas-dynamic models elaborated at the Institute of Astronomy of RAS [87, 88].

3.1 Roche lobe overflow by the planetary atmosphere

Consider a system composed of a star and a hot Jupiter as an analogue of a binary system with an extremely small mass ratio. On general grounds, the mathematical description of binary stars can be applied to star – hot Jupiter systems. Let us use the standard approach in binary star physics and consider the forces acting in a binary system consisting of a star with mass M_* and a planet with mass $M_{\rm pl}$. Let us use the standard assumption that the binary components move in circular orbits, and their rotation is synchronized with the orbital revolution $\Omega_* = \Omega_{\rm pl} = \Omega = 2\pi/P_{\rm orb}$, where $P_{\rm orb}$ is the orbital period. In addition, we will use the Roche approximation that both components are point-like and the gravitational potential is Newtonian.

Below, we will use a Cartesian frame (x, y, z) corotating with the binary, with the origin at the star's center. We will also assume that the x-axis is directed along the line connecting the centers of the binary components, the z-axis is perpendicular to the orbital frame and parallel to $\mathbf{\Omega}$, and the y-axis completes the right-hand coordinates.

In this case, the potential Φ of the forces in the system is called the Roche potential. The motion of the components proceeds according to Kepler's third law,

$$G(M_* + M_{\rm pl}) = A^3\Omega^2\,,$$

where A is the distance between the centers of the components. The system's barycenter is given by

$$R_{\rm cm} = \frac{M_{\rm pl}}{M_* + M_{\rm pl}}\,A\,.$$

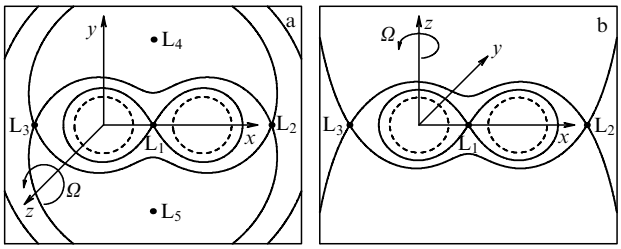

Figure 13. Roche equipotentials in (a) the equatorial xy and (b) frontal xz planes for a binary system with mass ratio $q = M_{\rm pl}/M_* = 1$. Dashed line shows the equipotential passing through point $(0.3A,\ 0,\ 0)$. The location of the Lagrangian points $L_1, \ldots, L_5$ is shown, and the coordinate frame used is also indicated.

To within a constant factor, the potential can be presented in the form

$$\Phi = -\frac{GM_*}{\sqrt{x^2+y^2+z^2}} - \frac{GM_{\rm pl}}{\sqrt{(x-A)^2+y^2+z^2}} - \frac{1}{2}\,\Omega^2\left[\left(x - A\,\frac{M_{\rm pl}}{M_*+M_{\rm pl}}\right)^2 + y^2\right]. \tag{5}$$

Equipotentials in the equatorial plane of system xy $(z=0)$ with the mass ratio $q = M_{\rm pl}/M_* = 1$ are shown in Fig. 13a. Figure 13b shows the equipotentials in the frontal plane xz $(y=0)$. Figure 13 also presents the coordinate frame (x, y, z). As seen in Fig. 13, near the centers of the components, the equipotentials are almost spherical. At a larger distance from the center, the gravitational action of the secondary component increases, and the equipotentials become ellipsoids extended along the x-axis. The rotation squeezes the equipotentials along the z-axis.

The Roche potential has five libration points, also called Lagrangian points. They are presented in Fig. 13. Their location is determined by the condition

$$\nabla\Phi = 0\,. \tag{6}$$

All five Lagrangian points lie in the equatorial plane, with three of them (L_1, L_2, and L_3) lying on the x-axis and that are inflexion points of the function Φ. The points L_4 and L_5 are maxima of the function Φ. The position of the inner Lagrangian point L_1 can be found from Eqn (6), which is usually written as [89, 90]

$$r_{L_1}^{-2} - r_{L_1} = q\left[(1-r_{L_1})^{-2} - (1-r_{L_1})\right], \tag{7}$$

where $r_{L_1} = x_{L_1}/A$.

The equipotential passing through the inner Lagrangian point L_1 binds two touching volumes known as the critical surface or the Roche lobe. This notion is fundamental in astronomy, because, for an object (star or planetary atmosphere) with the surface lying inside the Roche lobe, a stationary configuration is possible for which the gas pressure gradient balances the Roche potential gradient. When the star reaches the critical surface, the total force (the sum of the gravitational attractions to each component plus centrifugal force) vanishes at the inner Lagrangian point. The pressure gradient cannot be balanced at this point anymore, and matter overflow begins.

Consider characteristics of the overflowing matter for a typical hot Jupiter using WASP-12b as an example. In this exoplanet, the distance from the planet's center to the inner Lagrangian point L_1 is just $2R_{\rm pl}$, which allows us to consider the planet to be an object in which the upper atmospheric layers can extend beyond the Roche lobe. We will define the parameters of the flow in the vicinity of point L_1. Let planetary matter reaching point L_1 have density ρ_{L_1} and temperature T_{L_1}. The mass-loss rate through the inner Lagrangian point can be written as

$$\dot{M}_{\rm pl} = S\rho_{L_1} v_{L_1}\,, \tag{8}$$

where S is the stream's effective cross section, ρ_{L_1} is the density averaged over the stream's cross section, and v_{L_1} is the velocity. The flow through the inner Lagrangian point vicinity occurs similarly to gas expansion in a vacuum from a punctuated cavity. This means that the velocity through point L_1 is approximately equal to the speed of sound in the planetary atmosphere ($v_{L_1} \simeq c_{\rm s}$). Therefore, Eqn (8) can be written in the form

$$\dot{M}_{\rm pl} = S\rho_{L_1} c_{\rm s}\,. \tag{9}$$

In order to determine the outflow size near L_1, consider the possible motion of a particle with the local speed of sound $c_{\rm s}$ (i.e., with the specific kinetic energy $\sim c_{\rm s}^2$) from the Roche lobe of the donor star. By equating the potential energy difference in the plane to the specific kinetic energy, one can obtain an equation for the stream form near L_1 similar to the equation from paper [91]:

$$\Delta\Phi = c_{\rm s}^2\,. \tag{10}$$

By expanding this expression in a Taylor series in variables y and z and using $\nabla\Phi|_{(x_{L_1},0,0)} = 0$, we obtain the equation describing the stream form — an ellipse. After simple algebra, one can determine (see, e.g., [87, 88]) the stream's cross-section area at L_1 and, consequently, the planetary atmosphere's mass-loss rate. However, in astronomy, a simpler formula is widely used for the mass-loss rate from an astrophysical object filling its Roche lobe. To this end, one uses the notion of the effective (or volumetric) Roche lobe radius R_{L_1}, which is defined as the radius of a sphere with a volume equal to that of the Roche lobe, and the Roche lobe overflow degree $\Delta R = R - R_{L_1}$. According to [92], the mass-loss rate depends on the overflow degree of the Roche lobe by the atmosphere as

$$\frac{\dot{M}}{M_{\rm pl}} = \left(\frac{\Delta R}{R}\right)^3 \sqrt{\frac{GM_{\rm pl}}{R^3}}\,, \tag{11}$$

where R is the planetary atmosphere radius, and ΔR is the degree of Roche lobe overflow by the planetary atmosphere.

The planetary exosphere's boundary can be defined as the distance from the planet's center to the exobase, where the free-path length of particles compares with the characteristic height scale:

$$\frac{1}{R_{\rm ex}} = \frac{1}{R_{\rm pl}} - \frac{R_{\rm g}T}{GM_{\rm pl}}\,\ln\frac{R_{\rm pl}^2 R_{\rm g} T n_0 \sigma}{GM_{\rm pl}}\,. \tag{12}$$

Here, $R_{\rm ex}$ is the exobase height, T is the temperature of the upper atmospheric layers, $R_{\rm g}$ is the gas constant, n_0 is the particle number density in the atmosphere at the photometric radius $R_{\rm pl}$, and σ is the scattering cross section of the atmospheric gas.

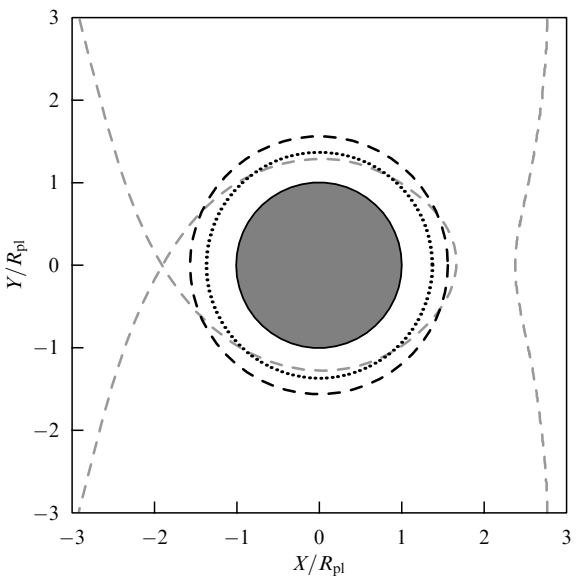

Figure 14. Photometric radius (grey-shaded circle), effective Roche lobe radius (dotted circle), and exobase height (dashed circle) for the planet WASP-12b. The grey dashed line indicates the Roche equipotential passing through point L_1 in the equatorial plane.

As an example, Fig. 14 schematically shows the photometric radius, the effective Roche lobe radius, and the exobase of a typical hot Jupiter, WASP-12b. It is seen that the planetary atmosphere exceeds the Roche lobe, with the overflow degree being $\sim 0.12R_{pl}$, which yields an extremely high mass-loss rate according to Eqn (11).

Paper [93] estimated the Roche lobe overflow degree by atmospheres of hot Jupiters with the orbital semi-major axes and photometric radii known at that time (189 planets in total). These data enabled estimating the exobase height and the degree of Roche lobe overflow. The paper showed that by assuming an atmospheric temperature of 10^4 K, almost a third of the planets should overfill their Roche lobes (10% at a temperature of 5000 K). The overflow degrees for these planets is $>1.1R_{pl}$ in all cases, reaching $2R_{pl}$ or more for some planets. Clearly, for such overflow degrees, the lifetime of giant planets cannot be sufficiently long. Correspondingly, mechanisms restricting the mass-loss rate from hot Jupiters should exist.

3.2 Stabilization of hot Jupiter envelopes by stellar wind

In paper [28], we considered the typical hot Jupiter WASP-12b and assumed that an early eclipse could arise due to a close nonspherical envelope around this planet that substantially exceeds the Roche lobe. This envelope results from the planetary atmosphere outflow through the L_1 and L_2 Lagrangian points. The interaction of the outflow with the stellar wind produces bow shocks with complex shapes. The dynamical pressure of the stellar wind makes the envelope stationary and long-lived.

Consider the motion of a hot Jupiter exoplanet in the stellar wind gas. For a solar-type star, the dependence of the local wind velocity and speed of sound on the distance to the star's center[1] is shown in Fig. 15. The solid line in this figure shows the planet's orbital velocity as a function of the orbital radius. Figure 15 suggests that the motion of the planet in the stellar wind is supersonic along the entire orbit: at small distances from the star due to a high orbital velocity, at large distances due to the supersonic radial velocity of the stellar wind.

[1] The parameters of the solar wind are taken from paper [77].

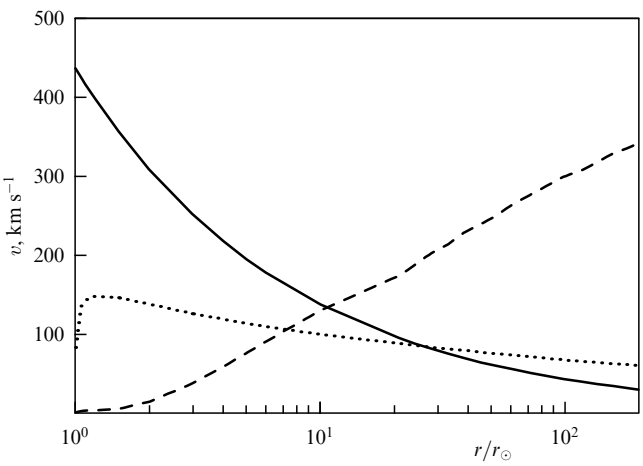

Figure 15. Stellar wind velocity (dashed line), orbital velocity of the planet (solid line), and local speed of sound (dotted line) for the Sun.

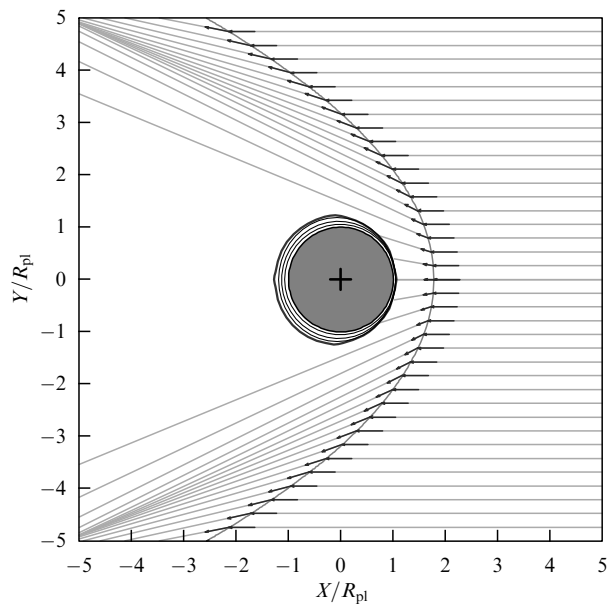

Figure 16. Contact discontinuity (thick solid line) and shock (thin solid curve) near a hot Jupiter. Shown are streamlines and wind velocity vectors upstream and downstream from the shock. The cross marks the planet's barycenter, and the grey-shaded circle indicates its photometric radius.

A planet moving supersonically with an atmosphere produces a bow shock in the stellar wind gas.[2] The contact discontinuity, the boundary separating the stellar wind from the atmosphere, is downstream from the bow shock. The structure of the flow, in this case, is schematically presented in Fig. 16.

In the idealized case of an equilibrium spherical atmosphere, it is possible to determine the contact discontinuity form using the momentum conservation [94]:

$$\rho_1 v_1^2 + p_1 = \rho_2 v_2^2 + p_2 \,, \tag{13}$$

[2] In Section 4 below, we will show that, in the presence of a magnetic field, the shock may not form.

where ρ_1 and ρ_2 are the densities, v_1 and v_2 are the velocities, and p_1 and p_2 are the pressures from both sides of the discontinuity. The pressure and density radial profiles in the upper atmosphere can be calculated from the hydrostatic equilibrium of an ideal gas in the gravitational field of a point-like mass:

$$\rho_{\rm atm}(r) = \rho_0 \exp\left[-\frac{GM_{\rm pl}}{R_{\rm gas}T_{\rm atm}}\left(\frac{1}{R_{\rm pl}} - \frac{1}{r}\right)\right], \quad p_{\rm atm}(r) = \rho_{\rm atm}\, R_{\rm gas}\, T_{\rm atm}\,, \tag{14}$$

where G is the gravitational constant, $\rho_{\rm atm}$ is the atmospheric density at radius r, ρ_0 is the atmospheric density at some radius $R_{\rm pl}$ (as a rule, ρ_0 is taken at the photometric radius of the planet), $R_{\rm gas}$ is the gas constant, $T_{\rm atm}$ is the planetary temperature, and $p_{\rm atm}$ is the atmospheric temperature at radius r.

By substituting the atmospheric density and pressure into the left-hand side of Eqn (13), and density, pressure, and inflow velocity of the stellar wind gas into the right-hand side of this equation, we can obtain an equation similar to the one determining the atmospheric form from [95]:

$$p_{\rm atm}(r) = \frac{\rho_{\rm w}\mathbf{v}_{\rm w}^2}{2}\cos(\mathbf{n}, \mathbf{v}_{\rm w}) + p_{\rm w}\,, \tag{15}$$

where $\rho_{\rm w}$ is the wind density, $\mathbf{v}_{\rm w}$ is the wind velocity, and $\mathbf{n}$ is the vector normal to the atmospheric surface. Equation (15) defines the form of the windward part of the atmosphere directly interacting with the stellar wind. The frontal collision point (FCP) at which $\cos(\mathbf{n}, \mathbf{v}_{\rm w}) = 1$ is closest to the planet's center.

The shock front lies at some radius from the contact discontinuity. The distance from the frontal collision point to the contact discontinuity is called the shock stand-off distance. Paper [96] proposes a semi-empirical formula for the shock stand-off distance:

$$\Delta = 1.1 r_0\,\frac{(\gamma-1)M^2+2}{(\gamma+1)M^2}\,, \tag{16}$$

where γ is the adiabatic index, M is the Mach number, and r_0 is the distance from the planet's center to the contact discontinuity. The form of the shock is determined by the equation

$$y^2(x) = 2R_{\rm s}(r_{\rm s} - x) + b_{\rm s}(r_{\rm s} - x)^2\,, \tag{17}$$

where $R_{\rm s}$ is the shock's curvature radius, $r_{\rm s} = r_0 + \Delta$ is the distance from the planet's center to the FCP, and $b_{\rm s}$ is the shock bluntness. The coefficients $R_{\rm s}$ and $b_{\rm s}$ are also defined by the semi-empirical equations

$$R_{\rm s} = \frac{\Delta\left(1 + \sqrt{(8/3)\epsilon^*}\right)}{\epsilon^*}\,, \tag{18}$$

$$b_{\rm s} = \tan\left(\frac{1}{M^2-1}\right)^2, \tag{19}$$

where ϵ^* is the shock compression coefficient determined from the equation

$$\epsilon^* = \frac{(\gamma-1)\,M^2+2}{2(M^2-1)}\,. \tag{20}$$

Equations (16) and (17) are obtained under the assumption that the form of the windward side of the contact discontinuity can be approximated by the equation

$$y^2(x) = 2R_0(r_0 - x) + b_0(r_0 - x)^2\,, \tag{21}$$

where b_0 is the bluntness of the contact discontinuity surface, and R_0 is its curvature radius. Equations (17) and (21) are presented in the form $y^2(x)$, because both atmosphere and bow shock are symmetric relative to the x-axis.

The contact discontinuity form can be obtained from Eqn (15). After that, by approximating it using Eqn (21), we can determine the parameters r_0, R_0, and b_0. Their substitution into Eqn (16) enables us to calculate the shock stand-off distance Δ and determine its form using Eqn (17). Note that Eqns (15) and (21) determine only the windward part of the atmosphere.

From equation (15), we can find the location of the FCP relative to the planetary barycenter. If the FCP lies inside the planet's Roche lobes, there is no outflow, because, in this case, the atmosphere does not touch the Lagrangian points L_1 and L_2 through which the outflow is possible. If the FCP lies outside the Roche lobe, an outflow is possible. In Fig. 17, the thick solid line separates the parameters of a fully closed (below the line) and an outflowing (above the line) atmosphere calculated for the exoplanet HD 209458b, assuming solar-wind-like stellar wind parameters [77]. For atmospheric parameters above the solid line in Fig. 17, outflows can appear from the vicinity of the inner Lagrangian point[3] L_1.

As shown in paper [28], such outflows (streams from the L_1 and L_2 points) can be stopped by the dynamic pressure of the stellar wind. Theoretically, it is possible to estimate the distance at which the stream from L_1 is blocked. The stopping criterion can be obtained from equation (13) by substituting the stream parameters (density $\rho_{\rm s}$, velocity $\mathbf{v}_{\rm s}$, and pressure[4] $p_{\rm s} = \rho_{\rm s}R_{\rm gas}T_{\rm atm}$) into one side of the equation and the wind parameters into the other side. We are looking for the criterion for the stream stop, not deviation, so we will consider only those points on its trajectory where the frontal collision point can exist, i.e., the stream and wind velocity vectors are assumed to be collinear.

Figure 18 schematically shows the ballistic stream trajectory from the L_1 point. The arrows crossing the stream trajectory indicate the stellar wind flow at the corresponding points in the stream. The figure suggests that, at some point (filled circle in Fig. 18; we will refer it to as the collinearity point), the stream motion is collinear to the stellar wind velocity, enabling us to solve equation (13).

It is easy to show that such a point will exist for any stellar wind parameters. At the very beginning, by leaving point L_1, the stream moves directly towards the star; its radial velocity is equal to the speed of sound, and the tangential velocity is zero. Further away, the Coriolis force deviates the stream so that, after some distance, it starts moving tangentially. There, the radial velocity vanishes and the transversal velocity is nonzero. It is easy to show that, at this point, the stream mostly approaches the star (we will call this point the periastron). Correspondingly, between point L_1 and the

[3] The points L_2 and L_1 are open almost synchronously; therefore, below in this paper, we will consider the criterion of the L_1 opening/closing.

[4] The assumption that the stream at each point has the same temperature as the atmosphere is entirely permissible, because the stream heating by radiation should occur similarly to the heating of the upper atmosphere of the planet.

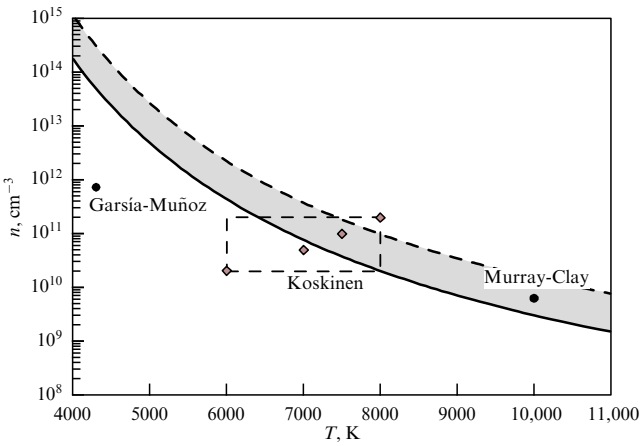

Figure 17. Atmospheric parameters of HD 209458b (temperature and gas number density at the photometric radius) at which the planetary atmosphere can belong to one of three distinguished types. Atmosphere is closed below the solid line. A quasi-closed atmosphere, in which the stellar wind can block the stream from point L_1, is possible inside the grey-shaded region. Open atmospheres lie above the dashed line. Points mark models from papers [20, 21]. Rectangle region corresponds to the parameter range of the upper atmosphere from paper [97]. Diamonds show model parameters for which 3D numerical simulations are presented.

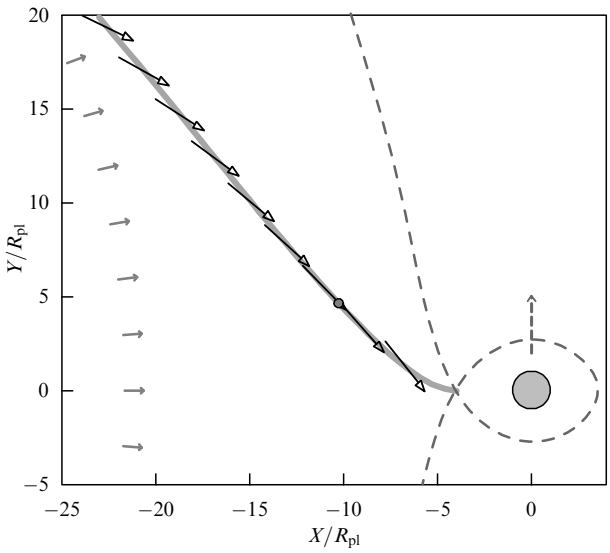

Figure 18. Ballistic trajectory of the stream from point L_1 (thick grey line). Dashed line shows the Roche equipotential passing through the L_1 point. The planetary center is at the point with coordinates $(0, 0)$. The arrows crossing the stream trajectory show the stellar wind flow in the frame corotating with the star – planet system. The solid grey arrows show the radial wind direction; the dashed grey arrow indicates the planet's orbital motion. The black dot on the ballistic trajectory corresponds to the point where the stream velocity is collinear with the stellar wind.

periastron, the velocity changes direction from purely radial to purely tangential. On the other hand, in the rotating frame, the wind velocity will be the sum of radial component v_r (we will assume it constant for simplicity) and tangent component v_t, depending on the distance:

$$v_t = \Omega r\,, \tag{22}$$

where r is the distance to the system's barycenter, which practically coincides with the star's barycenter. For an infinitely high radial velocity, the tangential component can be ignored, and, correspondingly, the collinearity point will be immediately at L_1, where the stream also moves radially.

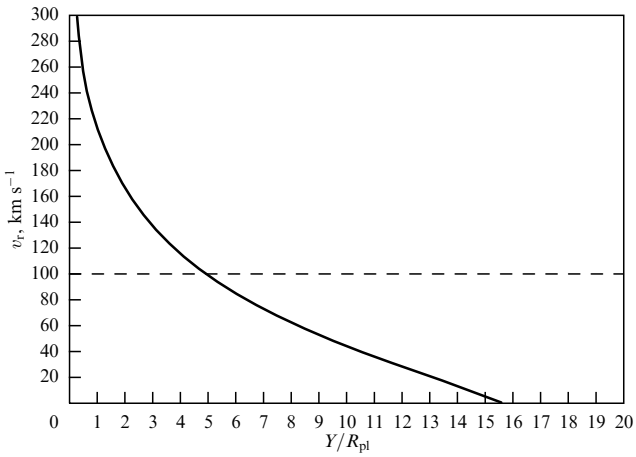

Figure 19. Radial stellar wind velocity which is needed to block the stream at a certain distance in the projection on the stellar limb. The dashed line shows the radial velocity of the solar wind at the orbital distance of WASP-12b.

For a zero radial wind velocity, the collinearity point shifts to the stream periastron, where it has only the tangential velocity. Correspondingly, by varying v_r from zero to infinity, we can place the collinearity point at any point of the stream, from L_1 to the periastron.

Figure 19 shows the wind velocity v_r which is needed to block the stream from the L_1 point of the planet WASP-12b at different distances. The distances are shown in the projection on the stellar limb, i.e., the distance observed during the planetary transit. Figure 19 suggests that the collinearity point should be at $\approx 5\,R_{pl}$ for the solar-wind parameters, in remarkable agreement with observations [16]. For the exoplanet HD 209458b, this point is at $\sim 7R_{pl}$ from the L_1 point, corresponding to the bow shock responsible for the early UV eclipse at a distance of $\sim 4.8R_{pl}$ in front of the planet projected to the stellar limb.

If condition (13) is satisfied at the collinearity point, the stream will be stopped, and the flow will be stationary. If the sum of the gas and dynamic wind pressure at this point is less than the sum of the same quantities for the stream, the motion of the stream will go on without stopping, because, at the distance from point L_1 to the periastron, there can be no second collinearity point. After passing the periastron, matter joins the stellar envelope, and most of it will not return to the planet anymore. If the total wind pressure exceeds that of the stream at this point, the stream can deviate, and the frontal collision point moves to the region where condition (13) is met.

Let us determine the criteria according to which a gas stream is not blocked by the dynamical wind pressure and the atmosphere is fully open, i.e., the planet can effectively lose its atmosphere in a short time. It is necessary to compute the critical density $\rho_0^*(T_{atm})$ separating solutions with a quasi-closed atmosphere ($\rho_0 < \rho_0^*$), where there are outflows that are stopped, however, by the stellar wind, leading to an extended nonspherical envelope formation, from solutions with a nonclosed (open) atmosphere where $\rho_0 > \rho_0^*$. In the calculations, several important physical effects should be taken into account. As the stream accelerates by moving in the star's gravitational field, its density should drop as it propagates. Using the known law of stream acceleration [98] and the Bernoulli equation, it is possible to determine the coefficient of the stream density decreasing as it propagates.

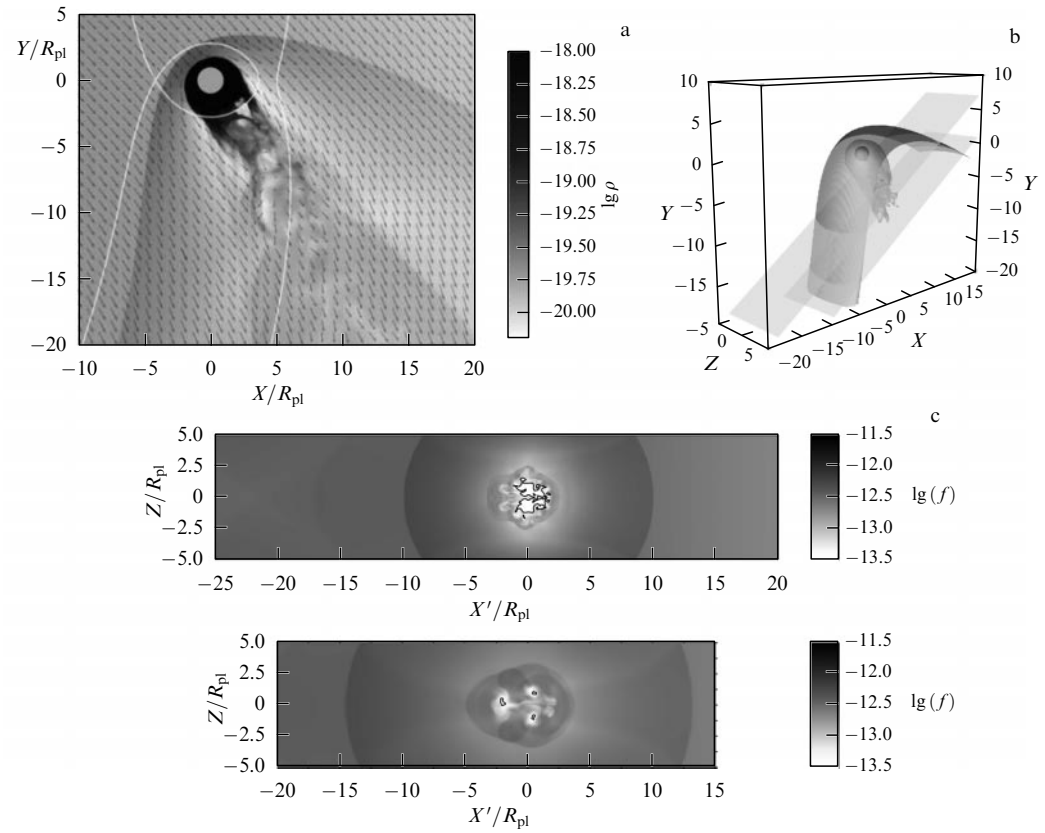

Figure 20. Results of modeling for calculation 1. (a) Logarithmic density and velocity distributions in the equatorial plane of the system. The barycenter has the coordinates (0, 0); size in units R_{pl}. White lines indicate the Roche equipotentials. (b) Flow 3D structure in calculation 1. Shown are the temperature isosurfaces corresponding to the shock and contact discontinuity and the planes through which the matter flow intensity is given. (c) Flow intensity through surfaces shown in the panel (b) on a logarithmic scale: regions with negative flux intensity (i.e., matter moves towards the planet) or with fluxes less than 3×10^{-14} g (cm^2 s)$^{-1}$ are contoured by black lines and shown in white, respectively.

Since in the approximation employed the radial wind velocity is constant, for a stationary flux the flow density should fall in proportion to the square distance to the star:

$$\rho_{\rm w} = \rho_{\rm w0}\left(\frac{r_0}{r}\right)^2, \tag{23}$$

where $\rho_{\rm w0}$ is the wind density at the distance r_0. Assuming that the stream density at the L_1 point is equal to that in the equilibrium atmosphere, we can calculate the density ρ_0 at the photometric radius from that at the stream stopping point. The critical density depends on the assumed atmospheric temperature (see (14)), so the final value of the critical density should be sought in the form $\rho_0^*(T_{\rm atm})$.

In Fig. 17, the critical density defining the condition of quasi-closeness of the atmosphere of HD 209458b is limited by the dashed line. All points lying in the hatched region between the two curves correspond to solutions with quasi-closed atmospheres. We can note that almost all atmospheric parameters for HD 209458b, including those falling in the ranges from paper [97], are in the region of either closed or quasi-closed atmospheres.

In paper [29], three-dimensional numerical gas-dynamic modeling was performed for different ρ_0 and T on the surface of the planet HD 209458b. In paper [99], the mass-loss rate for the obtained solutions was estimated. The utilized parameters are shown by the filled diamonds in Fig. 17 and are listed in Table 1. The results of numerical simulations for four selected sets of parameters are presented in Figs 20–23.

It is seen that the gas-dynamic pictures obtained are substantially different. In model 1 (Fig. 20), a closed atmosphere streamlined by the stellar wind is obtained. Here, a symmetric bow shock arises that has an almost spherical form at the FCP and tends to the Mach cone away from this point. The contact discontinuity bounding the atmosphere lies fully inside the planet's Roche lobe. Generally, the atmospheric form weakly deviates from a sphere.

Table 1. Atmospheric parameters used in modeling: temperature and number density at the photometric radius.

Model number	T, K	n, 10^{10} cm^{-3}
1	6000	2
2	7000	5
3	7500	10
4	8000	20

Figure 20b presents temperature isosurfaces corresponding to the shock and contact discontinuity for calculation 1. It is seen that the shock has a symmetric form (relative to the inflow velocity), spherical at the FCP and diverging as a Mach cone farther away from the planet. The contact discontinuity from the windward side of the planet has an almost spherical form.

Figure 20c displays, on a logarithmic scale, the intensity of mass flows across the planes shown in Fig. 20b. The first and second planes are located at a distance of $r_1 = 5\,R_{\rm pl}$ and $r_2 = 10\,R_{\rm pl}$ from the planet. The gradient filling shows the intensity of flows outward from the planet and exceeding $f \geqslant 3 \times 10^{-14}$ g (cm^2 s)$^{-1}$ ($f \geqslant 0.2\,f_{\rm w}$, where $f_{\rm w} = \rho_{\rm w} v_{\rm w} = 1.6 \times 10^{-13}$ g (cm^2 s)$^{-1}$ is the intensity of the unperturbed stellar wind flow at a distance from the star equal to the large orbital semi-axis; inside the computational domain, this

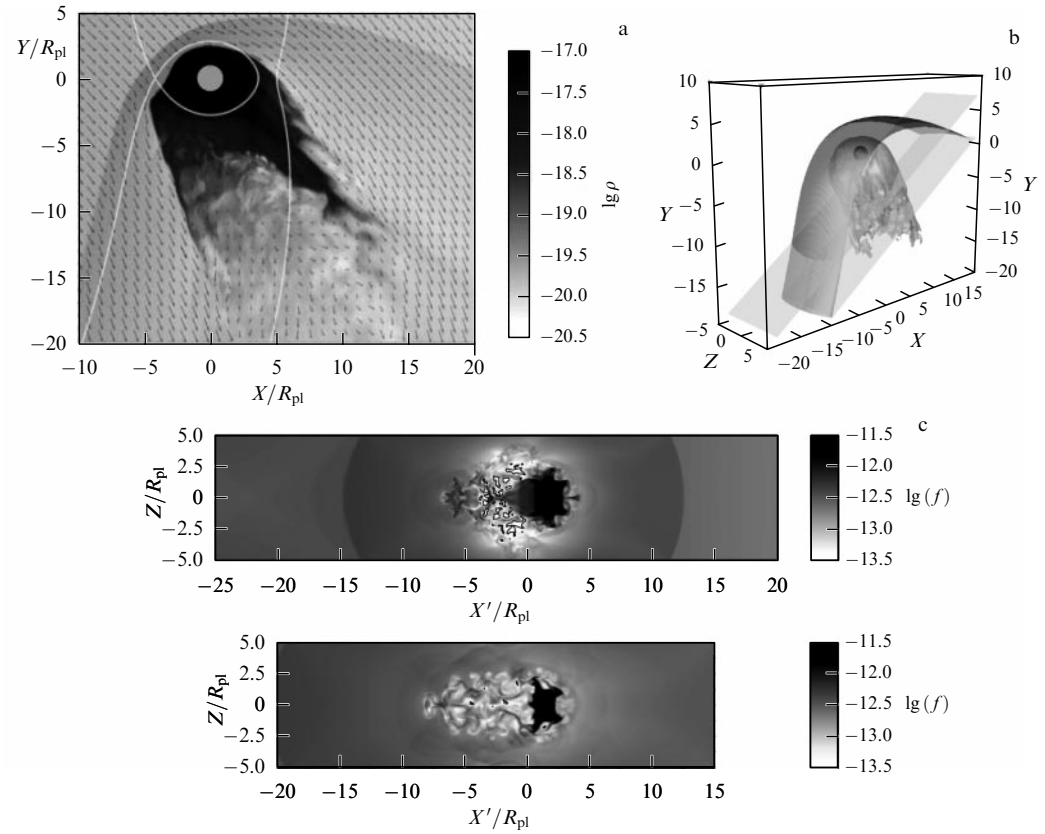

Figure 21. The same as in Fig. 20 for calculation 2.

parameter does not change significantly). Regions with solutions with negative fluxes or below the above value are encircled by black lines and colored in white, respectively. This figure suggests that the planet does not have strong outflows from the vicinity of the Lagrangian points, and, in a rarefied trail behind the planet, there is a curled mass flow not integrally exceeding the stellar wind outflow. This solution shows that an insignificant atmospheric mass loss occurs in the form of an outflow in the direction of the windward rarefied region behind the planet and then slowly streamed by the wind from the planet. Note that, in this case, all streams from the atmosphere are smaller than the wind flow, and only the upper limit on the mass-loss rate can be obtained. For this fully closed gas envelope model, the total mass outflow rate is $\dot{M} < 1 \times 10^9$ g s^{-1}.

In model 2 (Fig. 21), the atmospheric form is significantly nonspherical. Clearly, the FCP is shifted further away from the planet compared to model 1 but still inside the Roche lobe. In Fig. 21a, two cusps towards the L_1 and L_2 points are clearly visible, which, in particular, noticeably changes the shock and contact discontinuity form. The width of the trail is much larger than in model 1. Interestingly, in this case, there is no outflow from point L_1 to the star; however, a weak atmospheric outflow through point L_2 is seen. Thus, this envelope is partially open, despite the fact that, according to analytical estimates, it must be closed for these atmospheric parameters (see Fig. 17). This circumstance enables us to assess the accuracy of the analytical estimates as several percent, which is understandable, because these estimates ignored gas-dynamical effects.

Figure 21b shows the three-dimensional structure of the flow for calculation 2. As in model 1, the shock has a symmetric regular form but moves farther away from the planet. The most prominent part of the shock is outside the Roche lobe. Figure 21c shows the intensity of mass outflow through the planes shown in Fig. 21b (all notations and parameters are the same as in Fig. 20). It is seen that, in this model, there is a mass outflow from the L_2 Lagrangian point and a rarefied curled trail. The area of the flow decreases, and its mean density increases farther away from the planet. The outer boundary of the stream has a complex form that likely appeared due to contact discontinuity instability. In this model, the mass-loss rate from the closed (the flow from L_2 is partially open) gas envelope is $\dot{M} \simeq 1 \times 10^9$ g s^{-1}.

Figures 22 and 23 present the results for models 3 and 4, respectively. Clearly, the flow character qualitatively changed. Two powerful streams formed from the L_1 and L_2 points. Unlike solutions typical for close binary systems [100], the formation regions of the gas streams have significant sizes. The flux from L_1 starts from a sufficiently large area between the Lagrangian point and the upper edge of the Roche lobe. The stream from point L_2 has almost the same size. However, farther downstream, the forms of the two streams significantly differ. While the stream from L_1 gradually narrows, the flux from L_2, in contrast, appreciably widens. The isodensity lines indicate that the density in the stream from L_1 is much higher than from L_2 at the same distance from the planet. Interestingly, the flow from L_2 is separated in the longitudinal direction by one more shock, which probably resulted from the decay of the discontinuity at the boundary between the stream and the atmosphere.

Figures 22b and 23b show the principal elements of the flow for these two calculations. It is seen that the bow

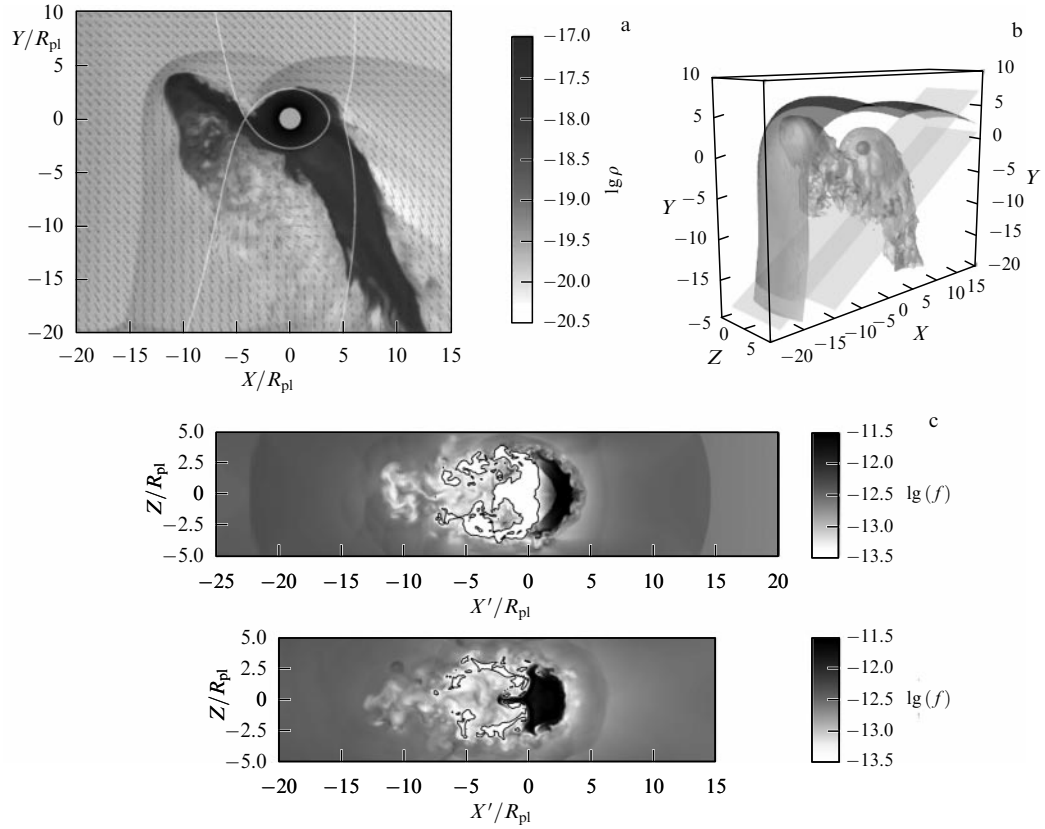

Figure 22. The same as in Fig. 20 for calculation 3.

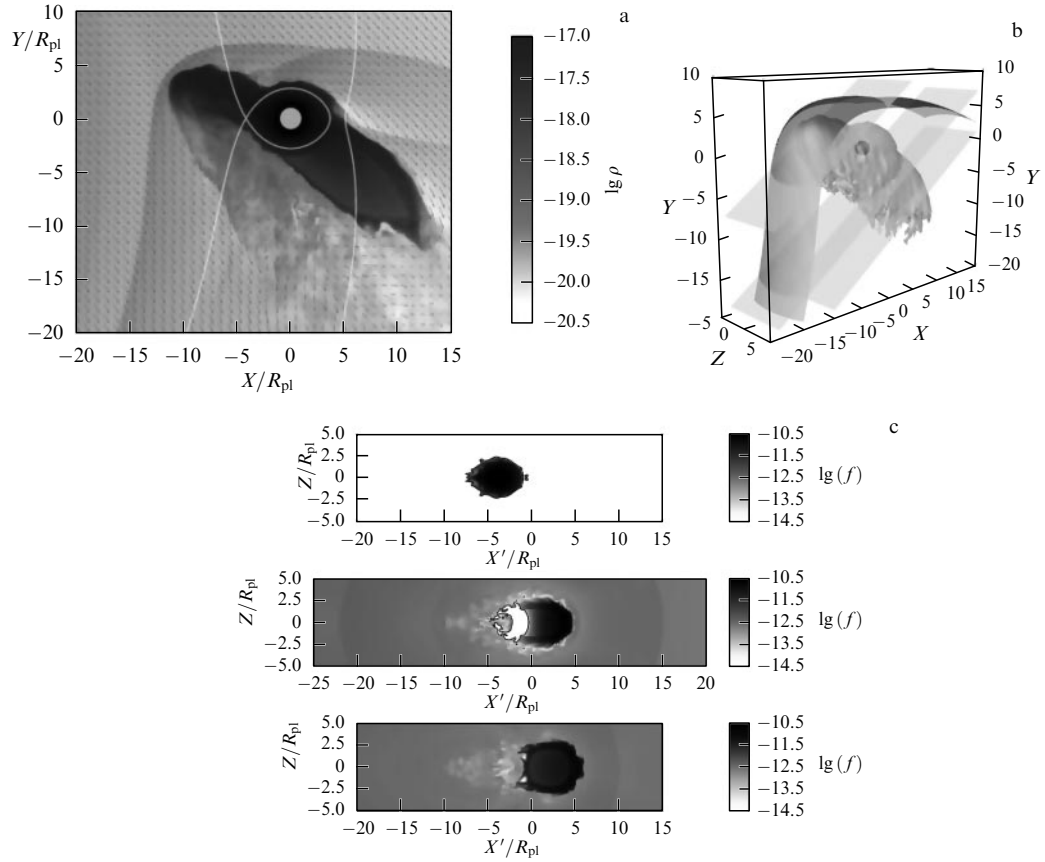

Figure 23. The same as in Fig. 20 for calculation 4.

shock consists of two shock waves, one formed around the atmosphere, the other around the stream from point L_1. It is possible to note that one more shock arises at their crossing point and extends from the shock-atmosphere joint point to the shock breaking at the joint point of its two branches. The FCP is at the edge of the stream from point L_2. The bow shock in front of the atmosphere spans a much larger computational domain than the previous models do. At the FCP, it extends up to the Roche lobe boundary. A broad trail is formed behind the planet. As this trail appears behind the planet and both flows, its width is much larger than previous models.

Figure 22c presents the mass outflow intensity through the planes shown in Fig. 22b. As the stellar wind fully blocks the outflow from point L_1, most of the matter expelled from the vicinity of point L_1 falls back into the atmosphere. Correspondingly, most of the mass is lost through point L_2. Note that, near the planet, the characteristic size of the stream from L_2 along the Z-coordinate exceeds that along the X'-coordinate, and there is a fallback region (upper diagram in Fig. 22c corresponding to the distance 5 $R_{\rm pl}$). The presence of the fallback stream evidences a complex flow in this region. The matter leaving the atmosphere through the vicinity of point L_2 starts expanding freely; here, as the rarefication zone is formed immediately behind the planet, the gas pressure gradient creates a force shifting part of the flow back to the planet. The Coriolis force winds up being part of the matter, forming a stationary vortex immediately close to the atmosphere near point L_2. The gas density in the vortex is several orders of magnitude lower than the atmospheric one; however, the Roche potential form in this region allows the vortex to remain in pressure equilibrium with both atmosphere and stream from point L_2. The vortex has a comparatively small size (of the order of several $R_{\rm pl}$). Correspondingly, farther away from the planet, the fallback flow disappears, as seen in the lower diagram in Fig. 22c. The L_2 flow density is approximately $f \simeq 10^{-11}$ g (cm^2 s)$^{-1}$ ($f \simeq 10^2 f_{\rm w}$), which coincides with the previous case, but here the stream cross section is several times as large. Similar to calculation 2, instabilities arise at the flow's outer boundary, although their effect is significantly less in this case. This is likely to be due to a higher density contrast between the stream and wind. The mass-loss rate in this model is estimated to be $\dot{M} \simeq 3 \times 10^9$ g s^{-1}.

Figure 23c presents the mass flow intensity across the planes shown in Fig. 23b. The middle plot in Fig. 23c indicates that, for the outflow from point L_2, a zone with a negative flow (i.e., moving towards the planet) arises near the planet. This is apparently for the same reasons as in calculation 3. There is a persistent matter outflow from the Lagrangian points L_1 and L_2. The streams from L_1 and L_2 have approximately the same area of $\simeq 20\, R_{\rm pl}^2$, and the mean flux density in them is $f \simeq 10^{-11}$ g (cm^2 s)$^{-1}$ ($f \simeq 10^2 f_{\rm w}$). The mass-loss rate from L_1 is $\dot{M}_{L_1} \simeq 17 \times 10^9$ g s^{-1}, the mass-loss rate from L_2 is $\dot{M}_{L_2} \simeq 14 \times 10^9$ g s^{-1}, and the total atmospheric mass-loss rate, in this case, is $\dot{M} \simeq 3 \times 10^{10}$ g s^{-1}.

Despite a similar flow pattern in calculations 3 and 4, they are fundamentally different: the solution in model 3 is quasi-closed, i.e., the streams from the Lagrangian points are blocked by the stellar wind, and a closed envelope with small matter outflow along the discontinuity forms; in model 4, in contrast, the stream from point L_1 does not stop and continues propagating towards the star; all the matter in the stream leaves the envelope, resulting in an intensive mass loss.

3.3 Effect of stellar radiation on flow in the envelope

The gas-dynamical models considered above did not take into account the stellar radiation pressure. This assumption can be justified by considering a high ionization degree of the envelope gas hampering radiation absorption. However, an estimate of the radiation pressure to gravity force ratio, $\beta = f_{\rm rad}/f_{\rm grav}$, for a nonexcited hydrogen atom in the envelope (see, e.g., [101]), turns out to be close to unity. This means that Ly-α radiation can significantly affect the gas dynamics of HJ envelopes, in analogy with the interstellar medium in the heliosphere [102]. In order to assess the radiation pressure effect on the dynamics of HJ envelopes, we need to estimate the ionization degree, the Ly-α radiation intensity, and absorption coefficients in the envelope.

In paper [103], we carried out three-dimensional modeling of the flow in the extended envelope of HD 209458b. We took into account nonstationary hydrogen ionization in the envelope and radiation pressure due to absorption in the Ly-α line. In the temperature interval $3.5 < \log T < 4.0$ and for the number density range $7 < \log n < 8$, the radiation absorption occurs mainly in Ly-α due to transitions of hydrogen atoms from the ground to the second level. The Ly-β contribution is significantly less, because the intensity in this line center is about 100 times smaller than in the Ly-α line [104]. As oscillator strength for the transitions $1 \to n$ decreases with the upper level, taking into account other Lyman lines does not significantly change the radiation pressure.

We can estimate the contribution from the Balmer lines by calculating the population of the second hydrogen level. According to the Boltzmann distribution,

$$\frac{n_2}{n_1} = \frac{g_2}{g_1} \exp\left(-\frac{\chi_2 - \chi_1}{kT}\right), \tag{24}$$

where n_1 and n_2 are populations of the first and second levels, g_1 and g_2 are the corresponding statistical weights, and the energy difference $(\chi_2 - \chi_1)$ between the first and second levels of a hydrogen atom is 10.2 eV. For temperatures in the HJ envelopes $kT < 0.9$ eV, therefore, $n_2/n_1 < 10^{-4}$. The flux ratio in the H_α and Ly-α lines for the Sun is $F_{\nu,\,{\rm H}_\alpha,\,{\rm cntr}}/F_{\nu,\,{\rm Ly\text{-}\alpha},\,{\rm cntr}} \sim 10^2$. Considering that the oscillator strength is 0.6 for H_α and 0.416 for Ly-α [105], we can conclude that, in an optically thin gas, the radiation pressure in the H_α line will not exceed 10^{-2} that in Ly-α. Other Balmer lines have less oscillator strength and thus can be ignored.

Other processes also insignificantly contribute to the radiation pressure. For example, the intensity of the ionizing radiation for hydrogen ($\lambda < 913$ Å, a bound-free transition) is less than that in the Lyman-alpha line, and bound-free absorption can be safely disregarded at these low temperatures. The Thomson scattering on electrons and negative hydrogen H^- absorption can be ignored because of an envelope's very small optical depth (see Section 3.3.5).

In addition, for the radiation pressure in the envelope, it is possible to disregard reemission processes. Indeed, after absorbing a photon, a hydrogen atom will be excited at level k for time $\tau_k = 1/(\sum A_{ki})$, where A_{ki} is Einstein's coefficient of spontaneous emission from the k to i energy level and the sum is taken over all levels i below the excited level k. For a hydrogen atom, $A_{ki} \sim 10^7$ s^{-1}, and the corresponding lifetime of the excited state is $\tau \sim 10^{-7}$ s. The characteristic collision time between hydrogen atoms in the envelope is $\tau_{\rm gas} \sim 10^1 - 10^2$ s; therefore, the collisional deexcitation can

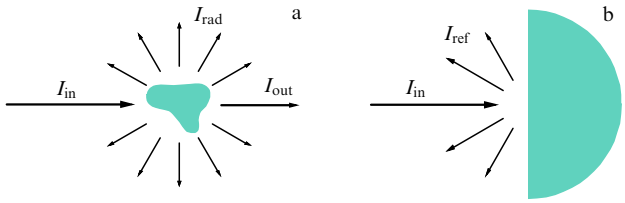

Figure 24. (Color online.) Scattering of radiation in matter: (a) transparent medium with a size comparable to the radiation absorption length; (b) opaque medium — a hemisphere filled with absorbing gas.

be ignored. After reemission, the photon moves in an arbitrary direction with a centrally symmetric distribution (for example, for a Lyman-alpha transition, the scattering angle distribution has the form

$$\phi(\omega) = \frac{11/12 + (1/4)\cos^2\omega}{4\pi} ,$$

where ω is the angle between the incident and scattered photons [106]). Therefore, this process does not contribute to momentum transfer. This statement remains valid even if the frequency of the reemitted photon differs from that of the absorbed one.

Consider two cases of radiation scattering in a medium: a transparent medium with a size comparable to the radiation absorption length (Fig. 24a) and an opaque medium — a hemisphere filled with absorbing gas (Fig. 24b). In the first case, after passing through the medium, some of the radiation remains unabsorbed, some will be absorbed due to collisional deexcitations of excited atoms, etc., and some will be reemitted. The reemitted photons will have a centrally symmetric distribution in space around the region with matter, because every incident photon can be absorbed and reemitted only once, on average, in a region with a size comparable to the absorption length.

In the second case of an optically thick medium, the photon will be reemitted until it leaves the envelope in the direction opposite to the incident one, or its energy is thermalized. That is to say, a gas region with a size much exceeding the absorption length works as a 'mirror', and the incident radiation is partially 'reflected'. Assuming that the gas state does not change, the maximally absorbed momentum can be up to two times as large as the incident radiation momentum. Correspondingly, by ignoring the reemission in optically thick regions, one could underestimate the radiation pressure by a factor of two.

In paper [103], we used a physical model for the radiation pressure similar to that described in [101]. The model takes into account the Doppler shift and self-absorption, the latter of which is very important, because the envelope is optically thick in the Lyman-alpha line.

To take into account the radiation pressure, the momentum equation should be added with the radiative pressure term, $\mathbf{f}_{rad}$:

$$\frac{\partial \mathbf{v}}{\partial t} + (\mathbf{v}\nabla)\mathbf{v} = -\frac{1}{\rho}\nabla p - \nabla\Phi - 2\left[\mathbf{\Omega}\times\mathbf{v}\right] + \mathbf{f}_{rad} , \qquad (25)$$

where ρ is the gas density, $\mathbf{v}$ is the velocity, p is the pressure, $\mathbf{\Omega}$ is the angular rotational velocity of the coordinate frame, and Φ is the Roche potential.

The model parameters and initial and boundary conditions were taken following the solution for a quasi-closed envelope around the planet HD 209458b [29]. In order to solve the system of gas-dynamic equations, we have used Roe's scheme [107] with TVD corrections and an entropy fix based on the LLF (Lax–Friedrichs) scheme. The elaborated numerical scheme possesses a low numerical viscosity in the smooth solution domain but does not smear shocks [108].

3.3.1 Photoionization. The radiation pressure in the Lyman-alpha line acts on neutral hydrogen only. To calculate the ionization of matter, one needs to compute the neutral hydrogen number density in the envelope, n_{HI}, at each moment by solving the transfer equation for n_{HI} simultaneously with gas-dynamic equations:

$$\frac{\partial n_{HI}}{\partial t} + \nabla(n_{HI}\mathbf{u}) = \mathcal{R} - \mathcal{C} - \mathcal{I} , \qquad (26)$$

where $\mathcal{R}$, $\mathcal{C}$, $\mathcal{I}$ are the rates of recombination, collisional ionization, and photoionization, respectively. The initial distribution of neutral hydrogen, n_{HI}, is determined from the Saha equation.

The recombination rate of atomic hydrogen due to collisions with electrons is computed by the formula

$$\mathcal{R} = \alpha_B(T)\, n_e\, n_{HII} = \alpha_B(T)(n - n_{HI})^2 , \qquad (27)$$

where $\alpha_B(T) = 2.55\times10^{-13}(T/10^4\,\mathrm{K})^{-0.79}$ cm^3 s^{-1} is the recombination coefficient for collisions of ionized hydrogen atoms with electrons. The envelope is optically thick for the radiation emitted during recombination to the ground level; therefore, the emitted photon ionizes another neutral hydrogen atom in the envelope, and the recombinations to the ground level do not change the gas ionization degree on average. In this case, one uses the 'B-case' recombination coefficient (see, e.g., [109]).

The collisional ionization due to inelastic collisions of neutral atoms with electrons is not significant in most of the envelope, because its temperature ($\sim 10^4$ K) is much lower than the hydrogen ionization energy (13.6 eV corresponds to $\sim 10^5$ K). Nevertheless, behind the planet (in the shadow region), the photoionization efficiency is zero, and then the ionization rate is determined by collisions, and we should consider this term. The collisional ionization rate can be calculated as

$$\mathcal{C} = c(T)\, n_{HI}\, n_e = c(T)(n - n_{HI})\, n_{HI} , \qquad (28)$$

where the collisional ionization coefficient was taken from paper [110]:

$$\begin{aligned} c(T) = \exp\Big[& -96.1443 \\ & + 37.9523\ln T \\ & - 7.96885(\ln T)^2 \\ & + 8.83922\times10^{-1}(\ln T)^3 \\ & - 5.34513\times10^{-2}(\ln T)^4 \\ & + 1.66344\times10^{-3}(\ln T)^5 \\ & - 2.08888\times10^{-5}(\ln T)^6 \\ & - \frac{157800}{T}\Big]\ \mathrm{cm}^3\ \mathrm{s}^{-1} . \end{aligned} \qquad (29)$$

In the grey approximation, assuming that all ionization flux goes to the Lyman series limit frequency, the last term in equation (26) for the photoionization rate can be written in the form

$$\mathcal{I} = \frac{F_{\mathrm{UV}}}{h\nu_0} \exp(-\tau)\, \sigma_{\mathrm{UV}}\, n_{\mathrm{HI}}\,, \tag{30}$$

where h is the Planck constant, $\sigma_{\mathrm{UV}} = 6.3 \times 10^{-18}$ cm^2 is the photoionization cross section at the Lyman continuum limit ν_0 (see, e.g., [111]), $F_{\mathrm{UV}} = F_0(a_{\mathrm{pl}}^2/l^2)$ is the ionization flux at the distance l from the star's center, $F_0 = 884$ erg s^{-1} cm^{-2} is the radiation flux at the planet's orbital distance, a_{pl} [112, 113], and τ is the optical depth. The optical depth is calculated similarly to absorption in the Ly-α line (see Section 3.3.2).

Thus, excluding the region behind the planet, the ionization is determined by a balance between photoionization and collisional recombination. The characteristic relaxation time for ionization is about several hours, which is an order of magnitude faster than the time needed for the envelope to be formed from the initial conditions; therefore, the choice of initial conditions for the ionization degree does not affect the final results.

3.3.2 Radiative pressure. To take into account radiation absorption in the envelope of a hot Jupiter we need to solve the radiation transfer equation:

$$\frac{\mathrm{d}I_\nu(\mathbf{n}, l)}{\mathrm{d}l} = -\alpha_\nu(l)\left[I_\nu(\mathbf{n}, l) - S_\nu(l)\right], \tag{31}$$

where the intensity $I_\nu(\mathbf{n}, l)$ is the energy flux at the distance l in the direction $\mathbf{n}$ at the frequency ν, $\alpha_\nu(l)$ is the absorption coefficient, and $S_\nu(l)$ is the source function. Ignoring reemission, Eqn (31) can be written in the form

$$\frac{\mathrm{d}I_\nu(\mathbf{n}, l)}{\mathrm{d}l} = -\alpha_\nu(l)\, I_\nu(\mathbf{n}, l)\,. \tag{32}$$

In order to calculate the radiation field, in paper [103] ray-tracing was used. Equation (32) was integrated along the ray from the stellar surface to the cell's center utilizing opacity coefficients in the envelope along the ray to calculate the intensity in each computational cell. After that, the energy absorbed in the cell was calculated, and, correspondingly, the radiation force acting on the cell. In the computational cell i with constant opacity $\alpha_\nu^i(\rho^i, T^i)$, the ratio between the incoming $I_{\nu,\mathrm{in}}^i$ and outcoming $I_{\nu,\mathrm{out}}^i$ intensities is calculated as

$$I_{\nu,\mathrm{out}}^i = I_{\nu,\mathrm{in}}^i \exp(-\alpha_\nu^i\, \Delta l^i)\,, \tag{33}$$

where Δl^i is the ray path length inside cell i. The radiation intensity reaching the nth cell is

$$I_{\nu,\mathrm{in}}^n = I_{\nu,\mathrm{in}}^0 \left[\prod_{i=0}^{n-1} \exp(-\alpha_\nu^i \Delta l^i)\right] = I_{\nu,\mathrm{in}}^0 \exp\left(-\sum_{i=0}^{n-1} \alpha_\nu^i \Delta l^i\right), \tag{34}$$

where the product and sum are taken over all cells along the ray between the star and computational cell n, and $I_{\nu,\mathrm{in}}^0$ is the incident intensity,

$$I_{\nu,\mathrm{in}}^0 = \frac{R_{\mathrm{star}}^2}{l_0^2}\, I_{\nu,\mathrm{star}}\,, \tag{35}$$

where R_{star} is the star's radius, l_0 is the distance from the star's center to the envelope's boundary cell along the ray, and $I_{\nu,\mathrm{star}}$ is the energy flux radiated from the stellar surface. The intensity of radiation absorbed in the nth cell is

$$\begin{aligned} I_{\nu,\mathrm{abs}}^n &= I_{\nu,\mathrm{in}}^n \int_{S_{\mathrm{cell}}^n} \left[1 - \exp(-\alpha_\nu^n \Delta l^n)\right] \mathrm{d}S \\ &\approx I_{\nu,\mathrm{in}}^n \int_{S_{\mathrm{cell}}^n} \alpha_\nu^n \Delta l^n\, \mathrm{d}S = I_{\nu,\mathrm{in}}^n \alpha_\nu^n V_{\mathrm{cell}}^n\,, \end{aligned} \tag{36}$$

where the integral is performed over the nth cell surface, S_{cell}^n, as it is seen from the star's center, Δl^n is the path length in the cell, and V_{cell}^n is the nth cell volume. Finally, the radiative pressure acting on the gas in the computational cell n is

$$\begin{aligned} f_{\nu,\mathrm{rad}}^n &= \frac{I_{\nu,\mathrm{abs}}^n}{c} = \frac{1}{c}\frac{R_{\mathrm{star}}^2}{l_0^2}\, I_{\nu,\mathrm{star}} \\ &\quad \times \exp\left(-\sum_{i=0}^{n-1} \alpha_\nu^i \Delta l^i\right) \int_{S_{\mathrm{cell}}^n} \left[1 - \exp(-\alpha_\nu^n \Delta l^n)\right] \mathrm{d}S\,, \end{aligned} \tag{37}$$

where c is the speed of light.

3.3.3 Ly-α profile in HD 209458. In our calculations, we use the Lyman-alpha line profile for HD 209458 from paper [101] shown in Fig. 25. The thick solid line shows the observed line profile, and the line profile corrected for the interstellar absorption is presented by the thin solid line. To calculate the radiation flux in the line at the stellar surface, $F_{\nu,\mathrm{star}}$, we should multiply the corrected line profile by $(d_{\mathrm{star}}/R_{\mathrm{star}})^2$, where d_{star} is the distance from Earth to HD 209458 [114]. The radiation pressure acting on one hydrogen atom is determined by the formula [115]

$$f_{\mathrm{atom}}(\nu) = \frac{\pi e^2}{m_{\mathrm{e}} c^2}\, f_{\mathrm{osc}}\, F(\nu)\,, \tag{38}$$

where e is the electron charge, m_{e} is the electron mass, and f_{osc} is the oscillator strength for the Lyman-alpha line. Then, the specific absorption coefficient is determined by the expression

$$\alpha(\nu) = \frac{\pi e^2}{m_{\mathrm{e}} c}\, f_{\mathrm{osc}}\, n_{\mathrm{HI}}\, \phi(\nu)\,, \tag{39}$$

where $\phi(\nu)$ is the line profile normalized as

$$\int_0^\infty \phi(\nu)\, \mathrm{d}\nu = 1\,. \tag{40}$$

The final result does not depend significantly on the choice of $\phi(\nu)$, because most of the absorption occurs in the line core, where the Doppler broadening shapes the line profile. In a gas element with bulk velocity u_{bulk}, each atom has the proper velocity u directed along the radiation propagation direction; the proper velocity distribution is assumed to be Maxwellian. Correspondingly, the line profile was taken as

$$\phi(\nu) = \sqrt{\frac{m}{2\pi kT}} \exp\left[-\frac{m\left(u(\nu) - u_{\mathrm{bulk}}\right)^2}{2kT}\right]. \tag{41}$$

Therefore, the absorption coefficient takes the form

$$\alpha(\nu) = \frac{\pi e^2}{m_{\mathrm{e}} c}\, f_{\mathrm{osc}}\, n_{\mathrm{HI}} \sqrt{\frac{m}{2\pi kT}} \exp\left[-\frac{m\left(u(\nu) - u_{\mathrm{bulk}}\right)^2}{2kT}\right]. \tag{42}$$

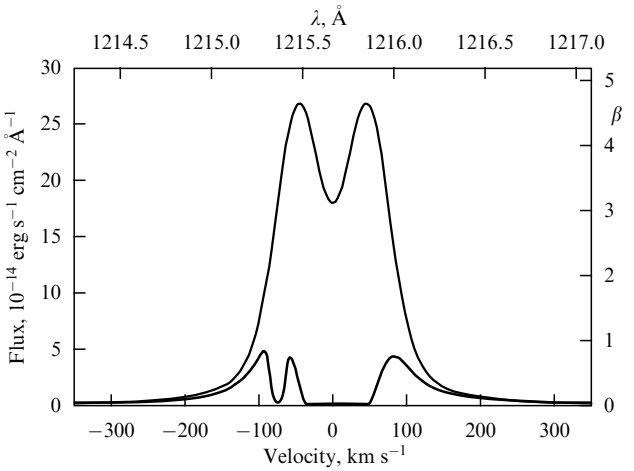

Figure 25. Lyman-alpha line profile from paper [101] for the star HD 209458. Thick solid line shows Lyman-alpha line profile as observed on Earth. Thin solid line shows line profile corrected for interstellar absorption. Corresponding values of the ratio $\beta = f_{\rm rad}/f_{\rm grav}$ shown to the right are calculated for a single neutral hydrogen atom using equation (38).

3.3.4 Results of three-dimensional modeling. Figure 26a shows the density (left) and neutral hydrogen fraction (right) distributions for a model of a quasi-closed envelope modeled taking into account the radiation pressure. The only significant difference from the case without radiation is that the gas flow from point L_1 is somewhat shorter (by $\sim 0.4\,R_{\rm pl}$) than without radiation pressure.

In paper [103], additional calculations with 10- and 100-fold intensities of the Lyman-alpha line and ionizing radiation were carried out to understand better the radiation pressure effect in this system. Figure 26b shows the solution for the 10-fold intensity. In comparison with the original solution, it is seen that the radiation pressure starts blocking the flow from the vicinity of the L_1 point, and the stream is shorter by $\sim 2\,R_{\rm pl}$ than in the case without radiation pressure. Still, the global structure of the flow in the system did not change qualitatively. As both the Lyman-alpha line and ionizing radiation intensity were enhanced, the mean fraction of neutral hydrogen in the stream from L_1 decreased by one order of magnitude from 10^{-2} to 10^{-3}. In the case of intensities 100 times higher (Fig. 26c), the radiation pressure entirely blocks the flow from L_1. In this case, the radiation pressure significantly affects the solution, although the neutral hydrogen fraction is as low as 10^{-4} in the stream from L_1.

In the right panels of Fig. 26, we can see a low-ionization region behind the planet (relative to the star located beyond the computational domain to the left). The ionization in this region is determined by the recombination and collisional ionization, which is less effective (see Section 3.3.1) than photoionization. The sharp boundary of the shadow region behind the planet in Fig. 26b appears because, with increasing ionizing radiation, the characteristic relaxation time to the stationary ionization degree gets much shorter than the characteristic gas-dynamic time in this region.

To illustrate the radiation pressure distribution in the envelope and its effect on the flow structure, we calculate the ratio between the radiative and gravitational forces, $\beta = f_{\rm rad}/f_{\rm grav}$, by assuming a fixed constant ionization degree. This calculation enables us to clearly show that the Ly-α line is completely absorbed in the envelope, and the main result of this section does not depend on the computational accuracy of the ionization degree in the solution. Figure 27 demonstrates $\log\beta$ for different ionization degrees: 0%, 90%, 99%, and 99.9% ($\log(n_{\rm HI}/n) = 0, -1, -2$, and -3, respectively). It is supposed that the stellar wind is fully ionized. In this figure, the gravitational force is defined as $f_{\rm grav} = -\,{\rm grad}\,\Phi$.

In the case of nonzero ionization (Fig. 27a), the ratio $\beta = f_{\rm rad}/f_{\rm grav}$ is of the order of unity only in a thin layer adjacent to the star. This corresponds to values plotted on the right ordinate of Fig. 25, showing that this ratio is about unity for a single neutral atom. But in the 'deeper' layers, the effect of the residual line intensity is insignificant compared to the gravitational force, because the 'external' layers already absorbed the energy in the line core. In addition, we see that several elements of the flow structure (for example, the flow from the L_2 point) can absorb energy in the line wings due to taking into account the Doppler shift when the energy in the line center has already been absorbed. But generally, β is of the order of unity only inside a skinny 'under-stellar' layer of the envelope. Therefore, the radiative force cannot change the general solution.

In cases with a nonzero ionization degree ($\lg(n_{\rm HI}/n) = -1, -2$, and -3), the Lyman-alpha radiation can penetrate deeper and affect the 'internal' parts of the envelope. Figure 28 shows the relative radiation pressure and dynamical wind pressure force acting on an element of the envelope contained within the solid angle $\Delta\Omega$ from the star's center shown by the white trapezoid in Fig. 27. When the neutral hydrogen fraction falls within the range $-4 < \lg(n_{\rm HI}/n) < 0$, the total radiation force acting on this element is almost constant. This 'plateau' illustrates that all energy in the line is absorbed, i.e., the envelope is fully opaque in the Ly-α line. Only when the neutral hydrogen fraction drops below $\lg(n_{\rm HI}/n) \sim 10^{-5}$ does the radiation pressure force become linearly dependent on the neutral hydrogen fraction. This corresponds to absorption in a transparent gas. For comparison, we show the gravitational force and stellar wind dynamical pressure; the former exceeds the radiation pressure by ~ 2 orders of magnitude. This result suggests that for HD 209458b the intensity of the Ly-α line of the host star is insufficient to cause any significant changes in the dynamical structure of the envelope.

Assuming that all Lyman-alpha radiation is fully absorbed, we can make a simple estimate of the radiation pressure. Full flux in the Ly-α line of HD 209458 on the stellar surface is

$$F_{\text{Ly-}\alpha} = \int_{-(3/2)\Delta\lambda}^{+(3/2)\Delta\lambda} F_{\rm star}(\lambda_{\text{Ly-}\alpha} + \lambda)\,{\rm d}\lambda = 6\times 10^5\ [{\rm erg\ s^{-1}\ cm^{-2}}]\,, \tag{43}$$

where $\Delta\lambda$ is the half-width of the Ly-α line. Then, the radiation pressure force acting on an element of matter (see Fig. 27) located at a distance of $\sim a_{\rm pl}$ and contained within the solid angle $\Delta\Omega$ (relative to the star's center) is

$$f_{\rm rad} = F_{\text{Ly-}\alpha}\,\frac{\Delta\Omega\,R_{\rm star}^2}{c}\,. \tag{44}$$

At the same time, the gravitational attraction force from the star is

$$f_{\rm grav} \sim G\,\frac{M_{\rm star}\,m_{\rm elem}}{a_{\rm pl}^2} = GM_{\rm star}\,\frac{\rho_{\rm clmn}\,\Delta\Omega\,a_{\rm pl}^2}{a_{\rm pl}^2}\,, \tag{45}$$

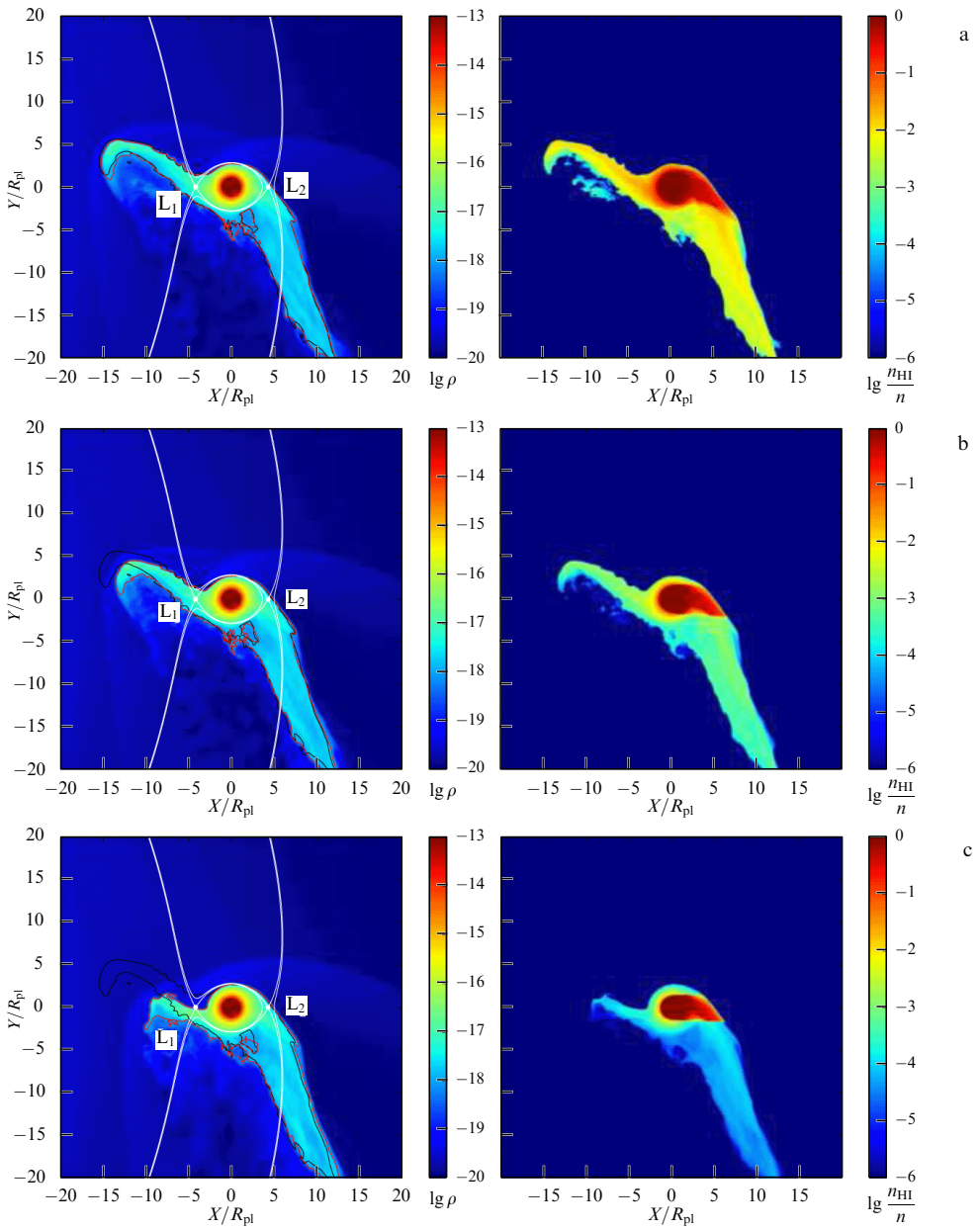

Figure 26. (Color online.) Logarithm of density (to the left) and neutral hydrogen fraction (to the right) in the system HD 209458b modeled taking into account the radiation pressure in the Lyman-alpha line. Solid red curve is the isodensity line ($\rho = 10^{-18}$ g cm^{-3}). It approximately encircles the contact discontinuity of the planetary envelope. Black solid curve shows a similar contour for the case without radiation pressure. Solid white curves indicate the Roche equipotentials passing through the L_1 and L_2 Lagrangian points. (a) Initial models. (b, c) Models for Lyman-alpha and ionizing radiation intensities, respectively, increased 10-fold and 100-fold.

where $\rho_{\rm clmn} = \int_{r_1}^{r_2} \rho_{\rm atm}\, {\rm d}l$ is the column density of atmospheric matter, r_1 and r_2 are the closest and the most remote (from the star) points of the envelope along the line of sight, and $\rho_{\rm atm}$ is the atmospheric gas density. Then, the ratio of these forces is

$$\beta = \frac{f_{\rm rad}}{f_{\rm grav}} \sim \frac{1}{c}\,\frac{F_{\text{Ly-}\alpha} R_{\rm star}^2}{G M_{\rm star}}\,\rho_{\rm clmn}^{-1} \sim 9\times 10^{-10}\,\rho_{\rm clmn}^{-1}\,. \qquad (46)$$

In the streams from points L_1 and L_2 (Fig. 29), the column density is about $10^{-8}-10^{-7}$ g cm^{-3}; therefore, β in these regions will be of the order of $0.1-0.01$. This simple estimate shows that in the hydrogen envelope of HD 209458b the radiation pressure force is at most several percent of the gravitational force.

3.3.5 Effect of other absorption mechanisms. Consider in detail the effect of electron Thomson scattering and absorption by negative hydrogen ions on the radiation pressure in our problem.

The Thomson scattering cross section is independent of wavelength and is $\sigma_{\rm T} = 6.65\times 10^{-25}$ cm^2. To calculate the energy scattered by an elementary volume of the envelope with the unitary cross section shown in Fig. 27, we should estimate the column density of electrons in this volume:

$$n_{\rm e-clmn} \lesssim n_{\rm clmn} = \frac{\rho_{\rm clmn}}{m_{\rm H}} \approx 10^{14}\ {\rm cm}^{-2}\,. \qquad (47)$$

The fraction of energy to be scattered (and hence the momentum to be transferred to the atmosphere) in this

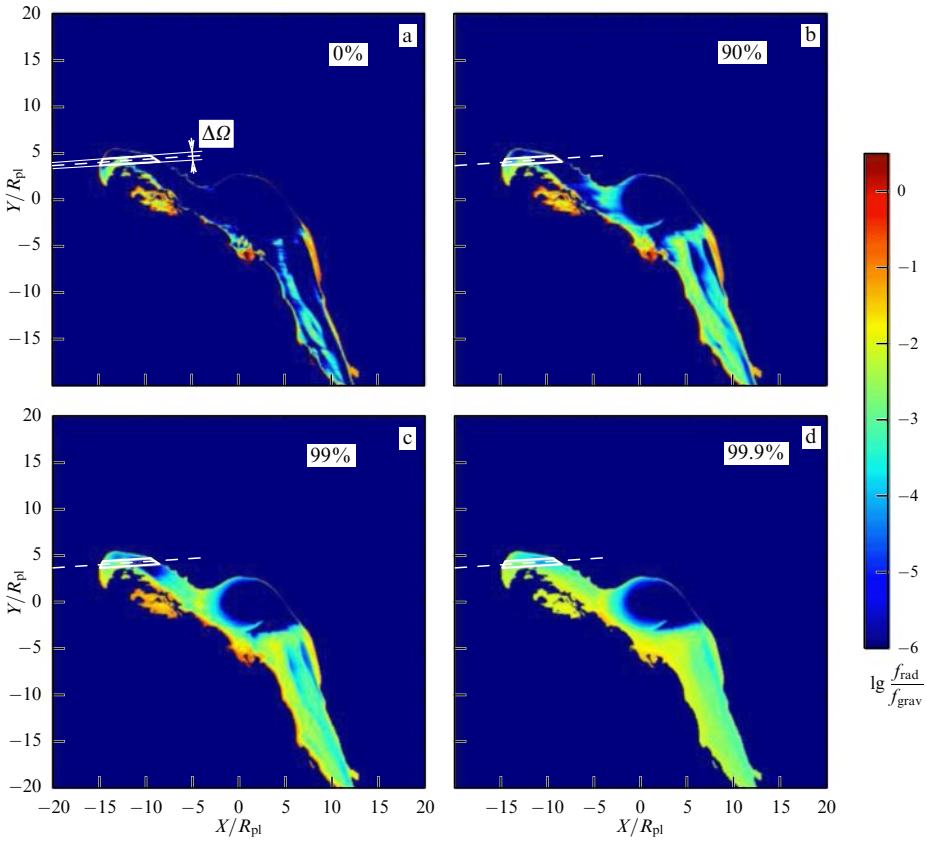

Figure 27. (Color online.) Ratio of the radiation pressure to the gravity force, $\beta = f_{\rm rad}/f_{\rm grav}$, calculated by assuming a constant hydrogen ionization degree of 0% (a), 90% (b), 99% (c), and 99.9% (d) ($\log(n_{\rm HI}/n) = 0, -1, -2$, and -3, respectively). Element of the stream from Lagrangian point L_1 along the line passing from the stellar center (dashed white line) is shown by the white trapezoid and is used to estimate the effect of radiation pressure on the envelope.

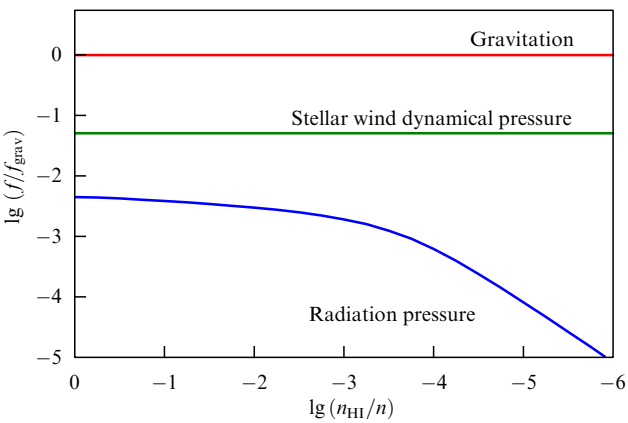

Figure 28. (Color online.) Dependence of relative radiation pressure force acting on the matter element shown in Fig. 27 by the white trapezoid on the neutral hydrogen fraction. Also shown are gravitation and stellar wind dynamical pressure forces acting on this matter element.

volume is

$$\frac{\Delta E}{E} = \sigma_{\rm T} n_{\rm e} \approx 10^{-10}\,. \tag{48}$$

The total energy emitted by a surface element of HD 209458 ($T_{\rm star} \approx 6092$ K [116]) per unit time is

$$F_{\rm star} = \sigma T^4 = 8 \times 10^{10}\ {\rm erg\ cm^{-2}\ s^{-1}}\,.$$

Using this value, we can compare the radiation pressure force on electrons with the pressure in the Lyman-alpha line:

$$\frac{f_{\rm e}}{f_{\rm Ly\text{-}\alpha}} = \frac{F_{\rm star}\,\Delta E/E}{F_{\rm Ly\text{-}\alpha}} \approx 10^{-5}\,. \tag{49}$$

Thus, this estimate suggests that the radiation pressure due to Thomson scattering on electrons is negligibly small compared to the pressure in the Ly-α line. Note that, in reality, the envelope of a hot Jupiter is expected to have an approximately solar chemical composition with a significant metal abundance, and in the case of their full ionization, the number of electrons can be several orders (~ 3) of magnitude higher than the number of hydrogen atoms (see formula (47)). But, as we have seen, this does not change the result obtained.

In order to estimate the energy absorbed by negative hydrogen ions, we should calculate their number density in the HJ envelope. In the local thermodynamic equilibrium (LTE) case, the number density of ions would be determined by the Saha equation:

$$n_{\rm e}\,\frac{n_{\rm HI}}{n_{\rm H^-}} = \frac{g_{\rm HI}}{g_{\rm H^-}}\,\frac{2(2\pi m_{\rm e} kT)^{1.5}}{h^3}\,\exp\left(-\frac{\chi_{\rm H^-}}{kT}\right). \tag{50}$$

Let us calculate the negative hydrogen number density for our parameters $n = 3 \times 10^7$ cm^{-3}, $T = 7.5 \times 10^3$ K, and ionization degree $n_{\rm HII}/n = 99\%$. In such a gas, the number density of atomic hydrogen is $n_{\rm HI} = 3 \times 10^5$ cm^{-3}, and the number density of electrons for pure hydrogen plasma is

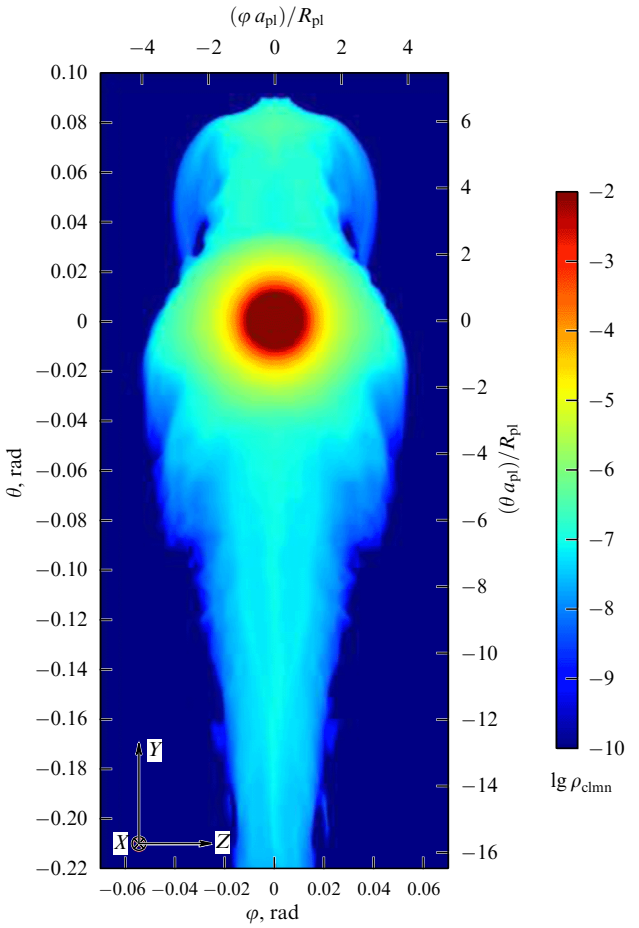

Figure 29. (Color online.) Envelope column density, $\rho_{\rm clmn}$, as seen from the star's center. The abscissa axis (angle φ, perpendicular to the orbit) and the ordinate axis (angle θ, counted along the orbit) correspond to the computational axes Z and Y.

$n_{\rm e} \approx 3 \times 10^7$ cm^{-3}. Statistical weights for these states are $g_{\rm HI} = 2$ and $g_{\rm H^-} = 1$, and the binding energy of a negative hydrogen ion is $\chi_{\rm H^-} = 0.75$ eV (see, e.g., [115]). In the LTE case with these parameters, the number density of the negative hydrogen ions would be

$$n_{\rm H^-} = 4.5 \times 10^{-9}\ {\rm cm}^{-3}\,. \tag{51}$$

However, in this case, by analogy with hydrogen ionization, the number density of negative hydrogen is not in the static equilibrium, and, to calculate it, we need to consider several reactions whose balance determines the negative hydrogen number density. The first pair of reactions include recombination and photodissociation:

$$\mathrm{H} + \mathrm{e}^- \rightleftharpoons \mathrm{H}^- + h\nu\,.$$

From left to right, it is the recombination of neutral hydrogen with electrons; from right to left it is the photodissociation of negative hydrogen by photons. As will be shown below, this is the principal reaction determining negative hydrogen number density. Deviations from the equilibrium number density are due to the possibility of a recombination photon leaving an almost transparent envelope. In the statistical equilibrium, the photon should be absorbed to dissociate another negative hydrogen ion, and the general state of matter does not change. However, in a transparent envelope, the radiation field is defined by the stellar emission, which is much weaker than needed for the equilibrium balance.

The recombination rate of electrons with neutral hydrogen atoms, corresponding to Ref. [117], has the following form:

$$\mathcal{R} = \alpha(T)\, n_{\rm HI} n_{\rm e}\,, \quad \alpha = 1.43 \times 10^{-18}\, T\,[{\rm K}]\,[{\rm cm}^3\ {\rm s}^{-1}]\,. \tag{52}$$

The photodissociation rate of negative hydrogen can be calculated as

$$\mathcal{I} = \int \frac{F_{\rm star}(\lambda)}{h\nu}\, \sigma_{\rm bf}(\lambda)\, {\rm d}\lambda \left(\frac{R_{\rm star}}{a_{\rm pl}}\right)^2 n_{\rm H^-}\,. \tag{53}$$

The radiation flux from the star HD 209458, $F_{\rm star}(\lambda)$, can be represented by a black body spectrum with temperature $T_{\rm star}$, and the dissociation cross sections of a negative hydrogen ion, $\sigma_{\rm bf}(\lambda)$, are taken from Ref. [118]. Then,

$$i_{\rm phot} = \int \frac{B(\lambda, T_{\rm star})}{h\nu}\, \sigma_{\rm bf}(\lambda)\, {\rm d}\lambda \left(\frac{R_{\rm star}}{a_{\rm pl}}\right)^2 \approx \frac{F_{\rm star}}{h\nu_{4760\ \text{Å}}}\, \sigma_{\rm bf,\,max} \left(\frac{R_{\rm star}}{a_{\rm pl}}\right)^2 = 8 \times 10^4\ [{\rm s}^{-1}]\,, \tag{54}$$

where the estimate is taken at $\lambda = 4760$ Å, corresponding to the maximum of the black-body emission with a given temperature. The precise value is $i_{\rm phot} = 10^4$ [s^{-1}]. The number density of negative hydrogen as determined by the balance of the first pair of reactions, photodissociation and recombination, is

$$n_{\rm H^-} = \frac{\mathcal{R}}{i_{\rm phot}} = 10^{-5}\ [{\rm cm}^{-3}]\,. \tag{55}$$

We see that it exceeds the equilibrium value by several orders of magnitude. We stress again that both number densities — the equilibrium one (50) and the one determined from photodissociation and recombination balance (55) — are proportional to the number density of electrons, and, therefore, the result does not depend on metals being taken into account. Consider now the next pair of reactions, including the dissociation of negative hydrogen by electron collisions and the inverse reaction:

$$\mathrm{H}^- + \mathrm{e}^- \rightleftharpoons \mathrm{H} + \mathrm{e}^- + \mathrm{e}^-\,.$$

For the reaction rate from left to right (dissociation), we can write the following expression:

$$\mathcal{C} = c(T)\, n_{\rm H^-}\, n_{\rm e}\,, \quad c(T) = \int f(E)\sigma(E) v_{\rm e}\, {\rm d}E\,, \tag{56}$$

where $c(T)$ is the integral over all energies from the product of electron energy distribution $f(E)$ (assumed to be Maxwellian), the collision cross section between an electron and a negative hydrogen ion $\sigma(E)$, and electron velocity $v_{\rm e}$ (which is proportional to the collision rate).

According to Ref. [119], the cross section of this inelastic collision is

$$\sigma(T) = 4\pi a_0^2 \left(\frac{R}{T}\right) \left[7.484 \ln \frac{T}{R} + 25.3\right], \tag{57}$$

where R is the Rydberg constant. Then,

$$c(T) \approx \sigma(T_{\rm gas}) \sqrt{\frac{kT_{\rm gas}}{m_{\rm e}}} = 2 \times 10^{-7}\ [{\rm cm}^3\ {\rm s}^{-1}] \tag{58}$$

(the exact value is $c(T) = 10^{-6}$ [cm^3 s^{-1}]). We can now assess the effect of this pair of reactions relative to the first pair (photodissociation and recombination) on the negative hydrogen ion number density:

$$\frac{\mathcal{C}}{\mathcal{I}} = \frac{c(T)\, n_{\rm e}}{i_{\rm phot}} \approx 10^{-3}\,. \tag{59}$$

The inverse reaction rate will be even lower, because it should be balanced with the electron collisional dissociation at the equilibrium temperature (50), much lower than that in system (55). Other reactions, for example, dissociation and neutralization by proton collisions,

$$\mathrm{H}^- + \mathrm{H}^+ \rightleftharpoons \mathrm{H}^+ + \mathrm{H} + \mathrm{e}^-\,, \quad \mathrm{H}^- + \mathrm{H}^+ \rightleftharpoons \mathrm{H} + \mathrm{H}\,,$$

are less important than electron collisional dissociation. They have comparable cross sections with the previous pair of reactions [115], but electron velocities are higher by two orders of magnitude; therefore, electron collisions dominate. This consideration suggests that the nonequilibrium number density of negative hydrogen ions will be determined by the first pair of reactions of recombination and photodissociation, i.e., $n_{\rm H^-} = 10^{-5}$ cm^{-3}. Here again, we note that this value was obtained for purely hydrogen plasma.

With a known negative hydrogen number density, one can calculate the energy to be absorbed or scattered in a volume of the unitary cross section shown in Fig. 27:

$$\Delta E = \int B(\lambda, T_{\rm star}) \big(\sigma_{\rm bf}(\lambda) + \sigma_{\rm ff}(\lambda)\big)\, {\rm d}\lambda \left(\frac{R_{\rm star}}{a_{\rm pl}}\right)^2 n_{\rm H^-,\,clmn}\,. \tag{60}$$

As the cross section of bound transitions for the negative hydrogen ion $\sigma_{\rm ff}(\lambda)$ becomes comparable to its dissociation cross section, $\sigma_{\rm bf}(\lambda)$, only for wavelengths $\lambda > 15{,}000$ Å [120] can we omit it in our calculations, because HD 209458 is a solar-like star. Then,

$$\begin{aligned}\varepsilon_{\rm phot} &= \int B(\lambda, T_{\rm star})\, \sigma_{\rm bf}(\lambda)\, {\rm d}\lambda \left(\frac{R_{\rm star}}{a_{\rm pl}}\right)^2 \\ &\approx F_{\rm star}\, \sigma_{\rm bf,\,max} \left(\frac{R_{\rm star}}{a_{\rm pl}}\right)^2 = 3 \times 10^{-8}\ [{\rm erg\ s}^{-1}]\,. \end{aligned} \tag{61}$$

The relative amount of energy absorbed in this volume will be

$$\frac{\Delta E}{E} = \frac{\varepsilon_{\rm phot}(n_{\rm H^-}/n)\, n_{\rm clmn}}{F_{\rm star}(R_{\rm star}/a_{\rm pl})^2} = 9 \times 10^{-16}\,. \tag{62}$$

The ratio of the radiative pressure force caused by the negative hydrogen absorption (which leads to its dissociation) to absorption (and the subsequent immediate reemission) by neutral hydrogen in the Lyman-alpha line is

$$\frac{f_{\rm H^-}}{f_{\rm Ly\text{-}\alpha}} = \frac{F_{\rm star}(\Delta E/E)}{F_{\rm Ly\text{-}\alpha}} \approx 10^{-10}\,. \tag{63}$$

This suggests that this absorption source is negligible in our problem. Here, we note again that, even if the envelope of a hot Jupiter has an approximately solar composition, the number of electrons will be by several orders of magnitude higher than we used in our estimate. But, as we see, the obtained result remains valid even for very high electron number densities.

To summarize the results presented in Section 3, we can assert that tidal interaction with a star should primarily determine both the formation and main properties of hot Jupiters envelopes. The Roche lobe overflow and the subsequent atmospheric mass flow through the vicinity of the inner Lagrangian point are the main reservoirs of matter for the envelope. Further interaction of the gas stream with the stellar wind shapes a quasi-closed envelope with a complex form and forward bow shock. Note that this model is in good agreement with existing observational data.

We should also add that the model in which the planetary magnetic field leads to the formation of a magnetopause and bow shock can also explain the beginning of the eclipse in transits of some HJs. An argument against the 'magnetic' model is the low magnetic field of some hot Jupiters (see Section 4 for more detail). However, the lack of direct measurements of magnetic fields in HJs does not allow us to reject this hypothesis.

Theoretically justified observational differences between the two hypotheses, in principle, enable us to chose between the models. Unfortunately, the attempt to experimentally test the hypotheses, for which we were given observational time on the Hubble space telescope (21 orbits), did not give a clear answer about the validity of the model with the Roche lobe overflow. The point is that the maximal size of a quasi-closed steady-state envelope is defined as the distance where the flow from L_1 can be blocked by the dynamical pressure of the stellar wind; otherwise, the envelope becomes open. The location of this point is determined only by the wind velocity profile. This point can exist for any radial stellar wind velocity; it is close to L_1 when the radial wind velocity is high and moves away from L_1 when the wind velocity decreases. The maximal distance of this point is reached for zero wind velocity.

According to simple ballistic estimates [121], the size of a stationary quasi-closed envelope around the exoplanet WASP-12b should be ~ 0.17 in phase units. A bow shock in front of this envelope can lead to excessive absorption in the near UV region starting from phase $\phi \sim 0.78$. For the eclipse to begin at phase $\phi \sim 0.83$, the size of the stream from L_1 should be $\Delta\Phi = 0.95 - 0.83 = 0.12$ or 21 planetary radii. This size agrees with estimates obtained by assuming solar-like stellar wind parameters. Comparing the theoretical envelope size with observations suggests that the quasi-closed envelope model can describe the existing observations. The difference in the envelope size at different phases can be explained by changing the stellar wind parameters. Unfortunately, both available beginnings of observations correspond to phase $\phi \sim 0.83$ [30, 31]. This prevents us from firm conclusions about the type of atmosphere in WASP-12b. If the additional absorption actually begins at earlier stages, the envelope size can exceed the maximum size of a stationary quasi-closed envelope, which requires interpreting the observations by the open-envelope model. Additional arguments supporting the Roche-overflow model can be found in papers [122–124], which consider complex atmospheric chemical composition and compare the model with more observational data. Turning back to the question about which model (with the Roche lobe overflow or the 'magnetic' one) is true, we note

that the whole model should consider both effects. This is why our Roche-lobe overfilling model [28, 29] was developed mainly by fully taking into account the proper magnetic field of the planet and the magnetic field in the stellar wind.

4. Magnetic field effect on the dynamics of envelopes of hot Jupiters

Hot Jupiters can have the proper magnetic field that should affect the stellar wind flow around them. However, estimates of the proper magnetic field of hot Jupiters show that it must be quite weak. The characteristic magnetic moment of hot Jupiters is about $(0.1-0.2)\,\mu_{\rm jup}$, where $\mu_{\rm jup} = 1.53\times10^{30}$ G cm^3 is Jupiter's magnetic moment. This value is in good agreement with both observational [68, 85, 125, 126] and theoretical [127] estimates. Such a low magnetic moment is explained by inefficient dynamo generation of the magnetic field in the planetary interiors. This as due to the close location of hot Jupiters to their host stars. Due to strong tidal interactions, the proper rotation of a typical hot Jupiter should be synchronized with its orbital motion in several million years [128]. For synchronous planetary rotation, the efficiency of the magnetic dynamo drastically decreases.

The planet's interior structure strongly determines the dynamo generation of the planetary magnetic field (see, e.g., [129, 130]). For Jupiter-like planets, the deviation from the axial symmetry is the necessary condition for the dynamo (both laminar [131] and turbulent [132]) to operate [133]. This can be provided by the Coriolis forces in the rotating systems. The asymmetry can be manifested in planetary magnetic dipole–spin axis misalignment [127]. For example, in Jupiter, the magnetic-rotational misalignment is about 11°.

It should be noted that the magnetic field of hot Jupiters can be generated not only in the planetary interiors but also in the upper atmosphere. Estimates in [103] show that the upper atmosphere of hot Jupiters consists of almost fully ionized gas. This is due to thermal ionization and hard X-ray emission of the host star. Therefore, the upper atmospheric layers of a hot Jupiter can be called the *ionospheric envelope*. Paper [134] shows that the proper magnetic field of a hot Jupiter should control the formation of large-scale (zonal) flows in its atmosphere. Detailed 3D calculations [135, 136] demonstrate a complex picture of the wind flows in the upper atmosphere, where the magnetic field is important. In particular, electromagnetic forces can shift westward a hot spot forming in the under-sun point. This effect can appear in the light curves of hot Jupiters as well. For example, from a comparison of the observed light curves of the planet HAT-P-7 b with calculations, the magnetic field in the atmosphere is estimated to be 6 G [137]. Most likely, this value is greatly overestimated. Let us recall that the magnetic field in Jupiter's cloudy layer is 4–5 G, although the field is higher at the north and south magnetic dipole poles (14 G and 11 G, respectively). Jupiter's magnetic field is not purely dipole. The quadrupole and octupole components contribute 22% and 18%, respectively. The measurements of Jupiter's complex magnetic field by the Juno mission are presented in the recent paper [138]. Note, however, that, even in this case, the dipole component dominates in the magnetospheric region.

Finally, note that, due to the close location of the host star, hot Jupiters can possess quite a strong magnetic field induced by the stellar wind magnetic field. Calculations in [139] show that the corresponding induced magnetic moment can attain 10–20% of Jupiter's magnetic moment, which greatly exceeds the induced magnetic field of Venus and Mars. To summarize, we can conclude that the strength and configuration of the magnetic field in hot Jupiters remain an open issue.

The effect of the stellar wind magnetic field on the wind flow around the atmosphere of a hot Jupiter [140] can be pretty strong. This is because almost all hot Jupiters are located in the so-called sub-Alfvénic zone of the host star's stellar wind, where the wind velocity is less than the Alfvén velocity. Taking into account the orbital velocity of the planet, the flow velocity turns out to be close to the Alfvén velocity. Therefore, depending on the specific situation (large orbital semi-axis, the host star's spectral class and rotational velocity, the stellar wind features), the flow's super-Alfvénic and sub-Alfvénic regimes can be realized. Note that, in the super-Alfvénic regime, the magnetosphere of a hot Jupiter will include all basic elements of the magnetospheres of the Solar System's planets (bow shock, magnetopause, magnetospheric tail on the nightside, etc.) [141, 142]. In the sub-Alfvénic flow regime, there is no bow shock in the magnetosphere [143].

Other authors have made attempts to take into account the magnetic dipole in one-dimensional [23, 144, 145], two-dimensional [24], and three-dimensional [145 – 147] numerical aeronomic models of hot Jupiter atmospheres. However, these papers considered only the immediate vicinity of the planet, and mass-loss estimates were made ignoring extended envelopes. Paper [147] is an exception. In that paper, the authors performed three-dimensional numerical simulations in a wide spatial region and obtained MHD solutions for exoplanets with open and quasi-closed envelopes. In our recent papers, we have studied the effect of both proper planetary magnetic field [148, 149] and wind magnetic field [140, 150–152] on the dynamics of hot Jupiter envelopes. In this section, we present the results of our numerical modeling and discuss prospects for the further development of MHD models.

4.1 Effect of the proper planetary magnetic field

To describe the flow structure around a hot Jupiter, we will use the ideal single-fluid magnetic hydrodynamic approximation with an explicit background magnetic field [88, 140, 148, 153]. In this approach, the total magnetic field of a planet $\mathbf{B}$ is presented as the sum of a background field $\mathbf{H}$ and the magnetic field $\mathbf{b}$ induced by currents in the plasma, $\mathbf{B} = \mathbf{H} + \mathbf{b}$. In our problem, the background field is generated by sources outside the computational domain (inside the star or, more precisely, inside the corona, or inside the planet). Therefore, inside the computational domain, it should satisfy the potentiality condition, $\nabla\times\mathbf{H} = 0$. This property of the background field can be used to partially exclude it from the MHD equations [154, 155]. In addition, we assume that the background magnetic field is stationary, $\partial\mathbf{H}/\partial t = 0$, which corresponds to the case where the proper rotation of a hot Jupiter is synchronized with its orbital revolution.

Under the potentiality and stationarity conditions for the background magnetic field, the ideal MHD equations can be written in the form

$$\frac{\partial\rho}{\partial t} + \nabla(\rho\mathbf{v}) = 0\,, \tag{64}$$

$$\rho\left[\frac{\partial\mathbf{v}}{\partial t} + (\mathbf{v}\nabla)\mathbf{v}\right] = -\nabla P - \frac{\mathbf{b}\times\nabla\times\mathbf{b}}{4\pi} - \frac{\mathbf{H}\times\nabla\times\mathbf{b}}{4\pi} - \rho\mathbf{f}\,, \tag{65}$$

$$\frac{\partial \mathbf{b}}{\partial t} = \nabla \times (\mathbf{v} \times \mathbf{b} + \mathbf{v} \times \mathbf{H}) , \tag{66}$$

$$\rho \left[\frac{\partial \varepsilon}{\partial t} + (\mathbf{v}\,\nabla)\varepsilon \right] + P\,\nabla\,\mathbf{v} = 0 . \tag{67}$$

Here, as above, ρ is the density, $\mathbf{v}$ is the velocity, P is the pressure, and ε is the specific internal energy. The matter is assumed to be a perfect gas with the equation of state

$$P = (\gamma - 1)\,\rho\varepsilon , \tag{68}$$

where $\gamma = 5/3$ is the adiabatic index. In addition, in the present study, we disregard the magnetic viscosity effects. This last assumption will be justified below.

Our model assumes that the planet moves in a circular orbit. Therefore, it is convenient to use a noninertial frame rotating together with the star–planet system around the barycenter. In this frame, the locations of the star's and planet's centers do not change, and the angular momentum vector of the frame $\mathbf{\Omega}$ coincides with the orbital angular velocity of the star–planet system. In this frame, the specific external force entering the equation of motion (65) is expressed as

$$\mathbf{f} = -\nabla\Phi - 2(\mathbf{\Omega} \times \mathbf{v}) . \tag{69}$$

Here, the first term on the right-hand side describes the force caused by the gradient of the Roche potential Φ. The second term is the Coriolis force.

The background magnetic field is presented as $\mathbf{H} = \mathbf{H}_{\rm pl}$, where $\mathbf{H}_{\rm pl}$ describes the proper planetary magnetic field. Our model assumes that the magnetic field of the hot Jupiter is a dipole,

$$\mathbf{H}_{\rm pl} = \frac{\mu}{|\mathbf{r} - \mathbf{r}_{\rm pl}|^3} \left[3(\mathbf{d}\,\mathbf{n}_{\rm pl})\,\mathbf{n}_{\rm pl} - \mathbf{d} \right] , \tag{70}$$

where μ is the magnetic moment, $\mathbf{r}_{\rm pl}$ is the radius-vector of the planet's center, $\mathbf{n}_{\rm pl}$ is the unit vector from the planet's center to the observer, $\mathbf{d}$ is the unit vector along the magnetic axis, and the dipole magnetic moment is $\boldsymbol{\mu} = \mu\mathbf{d}$.

As an example, we consider the typical hot Jupiter HD 209458b. The main parameters of the numerical model were the same as in our previous studies (see, e.g., [28, 29]). For the reader's convenience, we present here the main parameters of the system: the host star's spectral class is G0, it has mass $M_* = 1.15 M_\odot$ and radius $R_* = 1.2 R_\odot$. The star rotates with a period of $P_{\rm rot} = 14.4$ days, corresponding to an angular velocity of $\Omega_* = 5.05 \times 10^{-6}$ s^{-1} or a linear equatorial velocity of $v_{\rm rot} = 4.2$ km s^{-1}. The planet's mass is $M_{\rm pl} = 0.71 M_{\rm jup}$, the photometric radius is $R_{\rm pl} = 1.38 R_{\rm jup}$, where $M_{\rm jup}$ and $R_{\rm jup}$ are the mass and radius of Jupiter, respectively. The large orbital semi-major axis of the planet is $A = 10.2 R_\odot$ corresponding to an orbital period of $P_{\rm orb} = 84.6$ h.

Initially, a spherically symmetric isothermal atmosphere was set around the planet with the density distribution

$$\rho = \rho_{\rm atm} \exp \left[-\frac{G M_{\rm pl}}{R_{\rm gas} T_{\rm atm}} \left(\frac{1}{R_{\rm pl}} - \frac{1}{|\mathbf{r} - \mathbf{r}_{\rm pl}|} \right) \right] . \tag{71}$$

Here, as above, $\rho_{\rm atm}$ is the density at the photometric radius, $T_{\rm atm}$ is the atmospheric temperature, and $R_{\rm gas}$ is the universal gas constant. The initial outer radius of the atmosphere was derived from the balance with the stellar wind pressure. We have used the following atmospheric parameters in the calculations: temperature $T_{\rm atm} = 7500$ K, particle number density at the photometric radius $n_{\rm atm} = 10^{11}$ cm^{-3}.

As the parameters of the stellar wind we used corresponding values of the Sun's wind at a distance of $10.2 R_\odot$ from the center of the Sun [77]: temperature $T_{\rm w} = 7.3 \times 10^5$ K, velocity $v_{\rm w} = 100$ km s^{-1}, concentration $n_{\rm w} = 10^4$ cm^{-3}.

In our calculations, we have assumed the magnetic moment of the hot Jupiter HD 209458b is equal to $\mu = 0.1\mu_{\rm jup}$. The magnetic dipole orientation is given by angles θ and ϕ, which are the model parameters. The Cartesian components of the unit vector $\mathbf{d}$ along the magnetic axis are defined by the expressions

$$d_x = \sin\theta\cos\phi , \quad d_y = \sin\theta\sin\phi , \quad d_z = \cos\theta . \tag{72}$$

Here, we assume that the proper planetary rotation is synchronized with the orbital revolution, and the proper spin axis collates with the orbital angular momentum.

To solve numerically the MHD equations presented in the previous section, we use a combination of the Roe [107] and Lax–Friedrichs [156–158] difference schemes. The solution algorithm is described in our paper [140] and includes several steps corresponding to the method of splitting over physical processes. First, we solve numerically a subsystem of equations corresponding to ideal MHD with proper magnetic field $\mathbf{b}$, ignoring the background magnetic field $\mathbf{H}$. To solve this system, we have used the Roe scheme [159, 160] (see also monograph [88]) for MHD equations with Osher's enhancing correction [161] on an inhomogeneous grid. This scheme is described in detail in [162]. Note that the MHD variant of the Roe scheme is implemented in the code in such a way that, without the magnetic field ($\mathbf{b} = 0$), this scheme strictly transforms into the Roe–Einfeldt–Osher scheme we used in purely hydrodynamic calculations presented in Section 3 and papers [28, 29]. For fast magnetosonic characteristics, Einfeldt's correction is implemented in the difference scheme [163]. For slow magnetosonic characteristics, the original Einfeldt correction disagrees with the purely hydrodynamical Roe scheme. Therefore, for these characteristics, a modified entropy fix is used [162]. In the second step, we solve numerically a subsystem of equations corresponding to the background field effects. To solve it, we have used the Lax–Friedrichs scheme [156–158] with TVD (total variation diminishing) [164] corrections [88].

To purify the magnetic field $\mathbf{b}$ divergence, we have used the generalized Lagrange multiplier method [165]. This choice is dictated by the essentially nonstationary flow around a hot Jupiter, especially in the downstream flow forming the magnetospheric tail.

Calculations were carried out in a Cartesian frame with the origin at the planetary center. The x-axis passes through the planet and star centers and is directed from the star to the planet. The y-axis is along the planet's orbital motion, and the z-axis is along the planet's proper rotation. We used the computational domain with the sizes of $-30 \leqslant x/R_{\rm pl} \leqslant 30$, $-30 \leqslant y/R_{\rm pl} \leqslant 30$, $-15 \leqslant z/R_{\rm pl} \leqslant 15$ and with the number of meshes $N = 480 \times 480 \times 240$. To increase the spatial resolution in the planetary atmosphere, an exponentially narrowing toward the center grid was used; its structure is described in [162]. The characteristic size of the mesh at the photometric radius of the planet was $0.02 R_{\rm pl}$, whereas, at the outer edge of the computational domain, the mesh size was

Table 2. Angles θ and ϕ determining the magnetic dipole orientation by relations (72), angular distance χ between the direction to the L_1 Lagrangian point and the closest magnetic pole, and mass-loss rate $\dot{M}$ for different models.

Model	θ	ϕ	χ	$\dot{M}$, 10^{10} g s^{-1}
1	0°	0°	90°	1.47
2	30°	0°	60°	1.48
3	60°	0°	30°	1.14
4	90°	0°	0°	1.13
5	90°	90°	90°	1.60
6	90°	180°	0°	1.13

around $0.4R_{\rm pl}$. The boundary conditions were the same as in [148].

We have carried out a numerical simulation of the flow structure around the hot Jupiter HD 209458b in the super-Alfvénic regime, when the wind's magnetic field is not substantial. Variants of calculations differ by the planetary magnetic dipole orientation only. The corresponding values of the angles θ and ϕ determining components of the vector **d** in formulas (72) are listed in Table 2. In models 1–4, the magnetic dipole tilt varied from the rotational axis (model 1) to the orbital plane (model 4) opposite the star. In model 5, the magnetic dipole was directed to the star. In model 6, the magnetic dipole was aligned with the orbital motion of the planet.

Figures 30 and 31 demonstrate the results of numerical calculations. Left panels of the figures show the logarithm density (in color gradations) and velocity (arrows) in the planet's orbital plane. The right scale presents the decimal logarithm of the density in g cm^{-3}. The right panels show the decimal logarithm of density in the planet's orbital plane (in color gradations) and three-dimensional magnetic field lines. The numerical solutions shown in these figures correspond to the time $0.26P_{\rm orb}$ from the count beginning. The light lines in the left panels represent the Roche equipotentials passing near the Lagrangian points L_1 and L_2. The planet in the center of the computational domain is shown by the light circle with a radius corresponding to the planet's photometrical radius $R_{\rm pl}$. For clarity, the Cartesian coordinates x and y in the orbital plane are expressed in the planetary photometric radius $R_{\rm pl}$.

Analysis of these figures suggests that the qualitative picture of the flow near a hot Jupiter looks similar in all models and fully corresponds to a purely gas-dynamic flow around a quasi-closed envelope [28, 29]. This is due to a relatively weak proper planetary magnetic field in our models that does not significantly affect the matter dynamics.

Figures 30 and 31 show that two powerful outflows from the Lagrangian points L_1 and L_2 are formed in all models. The first stream is formed on the dayside and is directed to the host star. The gas in this flow protrudes against the stellar wind by the gravity force. The second stream is formed on the nightside and extends behind the planet as a wide turbulent trail.

The interaction of the stellar wind with the planetary envelope gives rise to an easily noticeable bow shock. It consists of two or even several separate shocks. The main shock arises immediately around the planetary atmosphere. Other (secondary) shocks appear around the stream from the inner Lagrangian point L_1 and its pronounced fragments and bulges. During the planet's orbital motion, a tangential discontinuity appears at the boundary separating the wind plasma and the envelope matter, because there the wind plasma moves along the envelope surface. The Kelvin–Helmholtz instability strongly distorts the boundary, but the distortion is rapidly brought back by the flow. A similar phenomenon is observed at the rear (along the orbital motion of the planet) part of the stream from the inner Lagrangian point L_1. The motion of matter in the stream is blocked by the dynamical pressure of the stellar wind and flung back. The produced gas flow is turbulized and fragments into many separate blobs. Most of this matter goes into the turbulent trail behind the planet.

Figures 30 and 31 show that the planetary magnetic field remains close to a dipole inside the Roche lobe. However, in the streams arising on the day and night sides, the magnetic lines are pulled out by the plasma flow from the ionospheric envelope. Along the stream from the inner Lagrangian point L_1, the magnetic field strength stays almost constant and is around 10^{-3} G. At the shock front, the magnetic field lines break according to the Hugoniot conditions.

Near the magnetospheric cusp (the region with open planetary field lines), the wind plasma can freely penetrate the upper atmosphere to cause an auroral glow. The most powerful particle fluxes from the wind plasma should have been formed in models 4 and 6, in which the magnetic poles lie along the line connecting the star's and planet's centers. However, the free arrival of particles at the magnetic poles is hampered by the ionospheric envelope. Therefore, the resulting ultimate flows should significantly weaken. This may explain present unsuccessful attempts to detect auroral glows in the atmospheres of hot Jupiters. For example, the authors of [166] attempted to detect radio emission from auroral regions of hot Jupiters HD 114762, 70 Vir and τ Boo using the Karl G Jansky Very Large Array (VLA). However, no significant radio flux was detected at the predicted frequencies. Another explanation for the null result proposed in paper [167] assumes that the cyclotron maser instability condition is not fulfilled [168], which is the main radio emission generation mechanism in planetary magnetospheres.

The mass-loss rate from hot Jupiters with different types of gas envelopes was calculated in paper [99] for a purely hydrodynamical case. Three-dimensional MHD simulations performed in paper [148] suggested that the presence of an even tiny magnetic field can noticeably decrease the mass-loss rate $\dot{M}$. This means that closed and quasi-closed ionospheric envelopes can appear around such planets for high Roche-lobe overflow degrees because, in this case, additional energy is required to overcome the magnetic pressure and line tension.

Our calculations show that the mass-loss rate also depends on the orientation of the planetary magnetic dipole field. Table 2 lists mass-loss rates for different models of hot Jupiter atmospheres. The value of $\dot{M}$ lies within the range from 10^{10} g s^{-1} to 2×10^{10} g s^{-1}. The maximum mass-loss rate (1.60×10^{10} g s^{-1}, model 5) differs by 42% from the minimum one (1.13×10^{10} g s^{-1}, models 4 and 6). The analysis suggests that the mass-loss rate increases with the angle χ between the direction to the star and the magnetic pole closest to the inner Lagrangian point L_1. The results of the calculations (see Table 2) can be empirically fitted as

$$\dot{M} = 1.1\times10^{10} + 4.9\times10^{7}\chi\ [\mathrm{g\ s^{-1}}]\,, \tag{73}$$

where the angle χ is in degrees. The obtained dependence can be explained by the fact that the strongest planetary magnetic

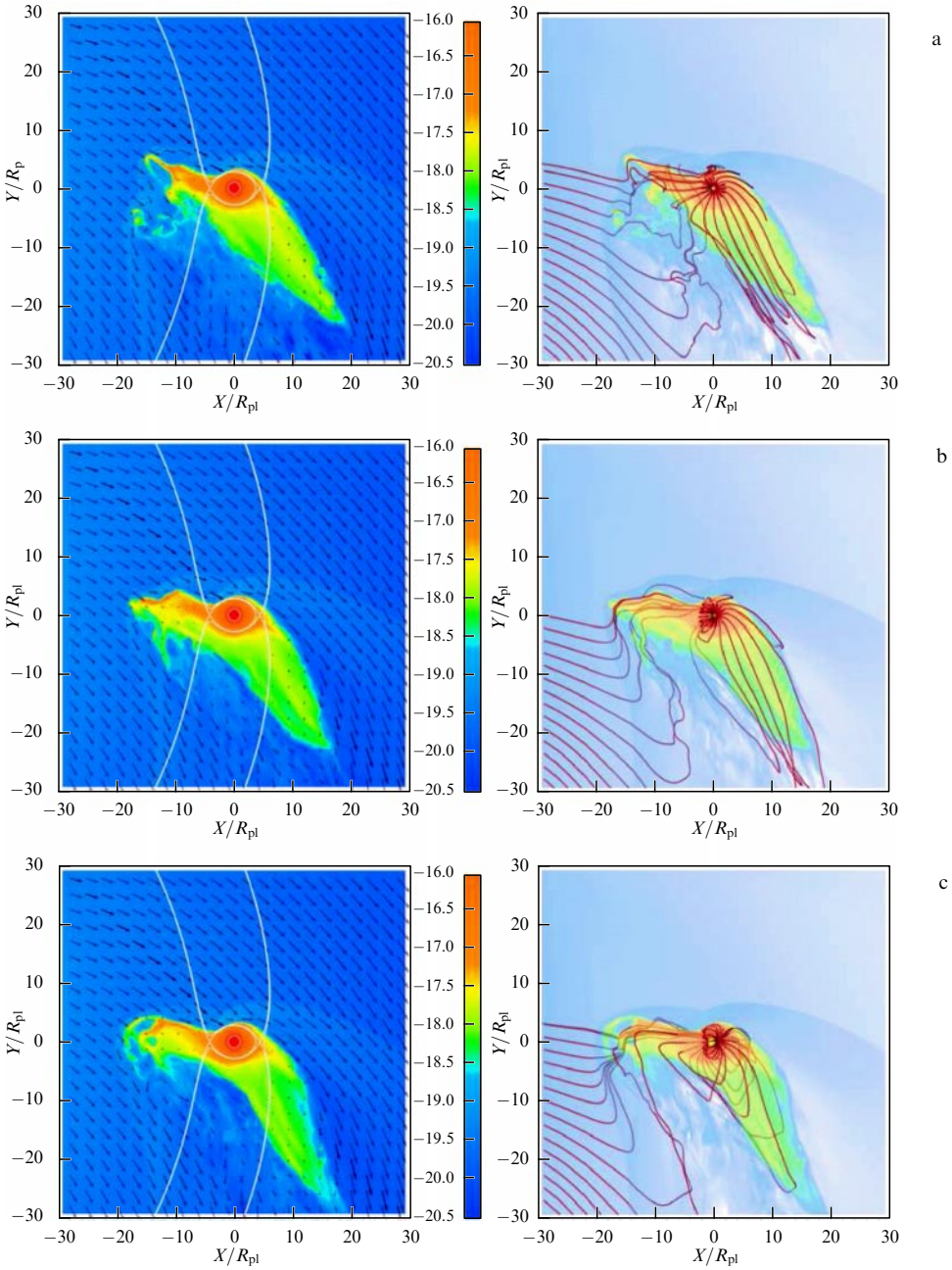

Figure 30. (Color online.) Distribution of decimal logarithm of density (color gradation), velocity (arrows in the left panels), and magnetic field (three-dimensional lines in the right panels) in the orbital plane of a hot Jupiter for models 1 ($\theta = 0°$, $\phi = 0°$) (a), 2 ($\theta = 30°$, $\phi = 0°$) (b), and 3 ($\theta = 60°$, $\phi = 0°$) (c). Solution is presented at the time moment $0.26P_{orb}$ from the beginning of calculations. Light lines in the left panels show the Roche equipotentials. Light circle corresponds to the planet's photometric radius.

field strength is attained at the magnetic poles in the upper atmosphere. Therefore, the closer the magnetic pole to the Lagrangian point L_1, the stronger the electromagnetic field hampering the motion of matter in the outflow. Of course, the matter moves freely along the magnetic field lines. However, in a stream with a relatively large diameter (around $3R_{pl}$), a perpendicular magnetic field component opposing the free outflow will be present.

4.2 Stellar wind effect

In our numerical model, to describe the stellar wind from the host star, we use well-studied properties of the solar wind. Much ground-based and space research (see, for example, recent review [169]) suggests that the solar wind magnetic field has a rather complicated structure. In the coronal region, the magnetic field is essentially nonradial, because there it is determined by the proper magnetic field of the Sun. At the coronal boundary located at several solar radii, the field becomes almost purely radial. Further away, there is a *heliospheric region* where the solar wind properties essentially determine the magnetic field. The magnetic field lines gradually twist into spirals with distance from the center in the heliospheric region due to the Sun's rotation. Therefore, especially at large distances, the magnetic field in the solar wind can be described with high accuracy by the simple Parker model [170].

However, the observed magnetic field in the solar wind is not axially symmetric and demonstrates a clear sectorial

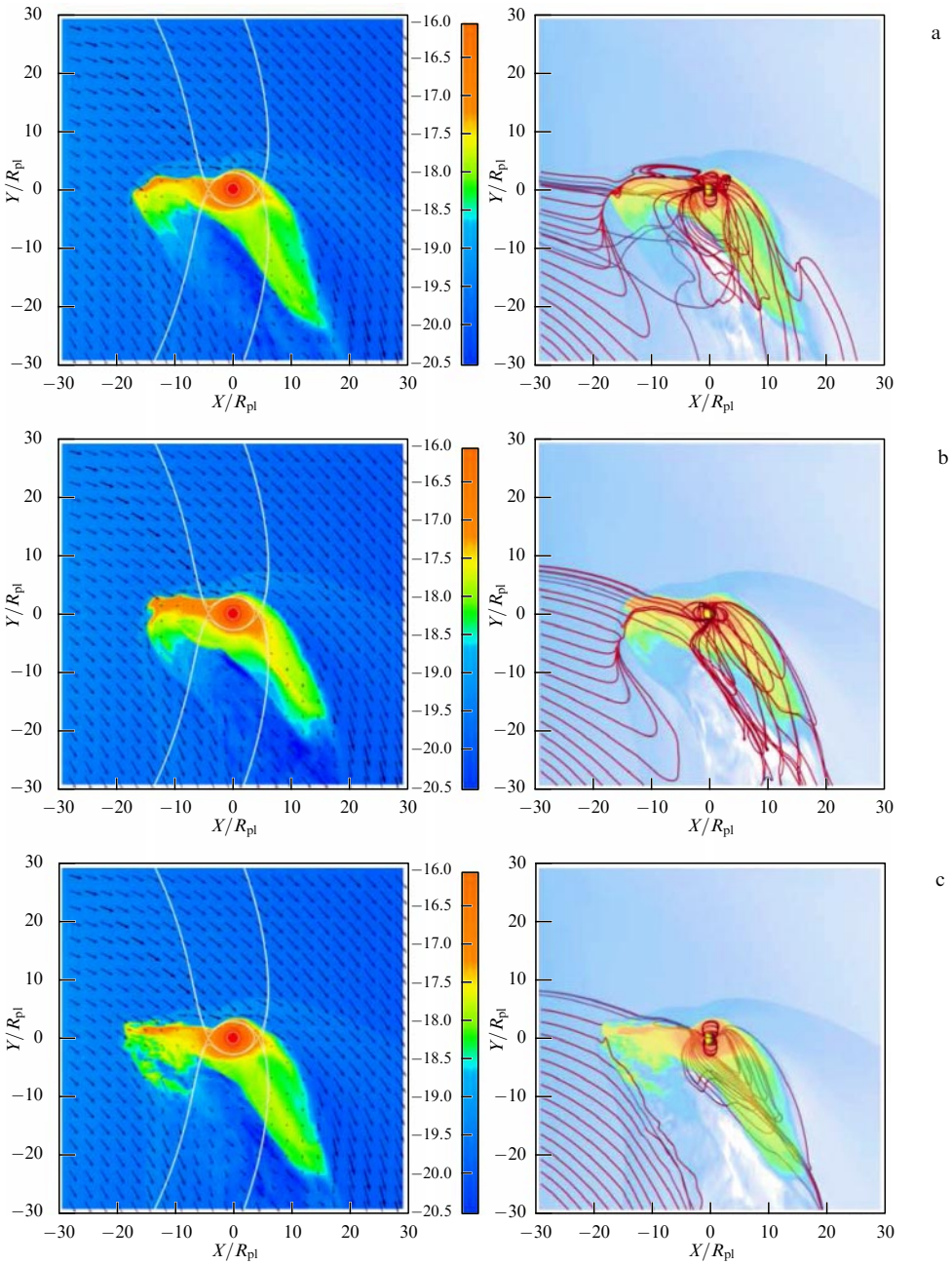

Figure 31. (Color online.) The same as in Fig. 30 for models 4 ($\theta = 90°$, $\phi = 0°$) (a), 5 ($\theta = 90°$, $\phi = 90°$) (b), and 6 ($\theta = 90°$, $\phi = 180°$) (c).

structure. This is because, at different points of the spherical surface of the corona, the field can have different polarities (the direction of the field lines with respect to the normal vector) due to, for example, the tilt of the Sun's magnetic axis to its rotational axis. As a result, in the ecliptic plane, two clearly separate sectors with different magnetic field directions are formed in the solar wind. In one sector, the magnetic field lines are directed toward the Sun, and in the opposite sector, from the Sun. These two sectors are separated by the *heliospheric current layer* corotating with the Sun. Therefore, during its orbital motion, Earth crosses it many times per year by passing from the solar wind sector with one polarity of the magnetic field to the neighboring sector with the opposite magnetic field polarity.

In the present review, we focus on the effects of global parameters of the magnetic field in the stellar wind and will assume that the orbit of a hot Jupiter lies inside the heliospheric region beyond the host star's corona. Therefore, to describe the magnetic field in the heliospheric region, in the first approximation, we can use the simple axially symmetric model from paper [171] (see also monograph [95]).

Taking into account the magnetic field, the background magnetic field in MHD equations (64)–(67) can be presented in the form $\mathbf{H} = \mathbf{H}_{pl} + \mathbf{H}_*$, where the first term $\mathbf{H}_{pl}$ describes the proper planetary magnetic field (70), and the second term $\mathbf{H}_*$ corresponds to the radial magnetic field component in the stellar wind B_r. The radial magnetic field of the stellar wind can be found from the Maxwell equation $\nabla \mathbf{B} = 0$. Considering the spherical symmetry, we obtain [95]

$$\mathbf{H}_* = \frac{B_* R_*^2}{|\mathbf{r} - \mathbf{r}_*|^2}\, \mathbf{n}_* \,, \tag{74}$$

where R_* is the stellar radius, B_* is the mean magnetic field on the stellar surface, $\mathbf{r}_*$ is the radius-vector from the stellar center, and $\mathbf{n}_*$ is the unit vector along the observer's line of sight. It is easy to verify that the background magnetic field is the potential: $\nabla \times \mathbf{H} = 0$.

Initially, the magnetic field $\mathbf{b}$ in the plasma will be determined solely by the azimuthal magnetic field component in the stellar wind. In the orbital plane of the planet, the azimuthal components of velocity v_φ and magnetic field b_φ are given by the expressions [171]

$$v_\varphi = \Omega_* r \, \frac{1 - \lambda^2 r_A^2/r^2}{1 - \lambda^2} \,, \tag{75}$$

$$b_\varphi = \frac{B_r}{v_r} \, \Omega_* \lambda^2 \, \frac{1 - r_A^2/r^2}{1 - \lambda^2} \,. \tag{76}$$

Here, v_r is the radial wind velocity, the radial coordinate r determines the distance from the stellar center, Ω_* is the angular rotational velocity of the star, and λ is the Alfvén Mach number for the radial velocity and magnetic field,

$$\lambda = \frac{\sqrt{4\pi\rho}\, v_r}{B_r} \,. \tag{77}$$

The Alfvén point is at the distance $r = r_A$ where the radial wind velocity v_r is equal to the Alfvén velocity $u_A = |B_r|/\sqrt{4\pi\rho}$, and the parameter is $\lambda = 1$. The regions $r < r_A$ and $r > r_A$ determine the *sub-Alfvénic* and *super-Alfvénic* zone of the stellar wind, respectively.

In paper [171], the Alfvén radius for the solar wind was found to be $r_A = 24.3 R_\odot$. In later studies, it was found to be at smaller radii (see, e.g., [172, 173]). Paper [174] analyzed solar activity over the last 250 years to conclude that the Alfvén radius can vary in the wide range from $15 R_\odot$ to $30 R_\odot$. On the other hand, the magnetic field of solar-type stars (parameter B_* in equation (74)) can differ from the solar value. The mean surface field of such stars falls in the range from about 0.1 to several Gauss [175, 176]. The magnetic fields of stars of other spectral classes can differ even more. In addition, the azimuthal magnetic field of the stellar wind (76) is determined by the proper stellar angular velocity (parameter Ω_* in equation (74)), which, in turn, also depends on the spectral class [176]. These facts expand the possible model parameter range.

Figure 32 shows the initial (without outflows from the envelope) structure of the magnetic field near the hot Jupiter HD 209458b modeled by us. The magnetic field parameters (field strength and the magnetic axis orientation) of the planet correspond to those in the calculations presented below. Figure 32 shows the distribution of magnetic field lines for $B_* = 10^{-3}$ G, a relatively weak wind field. The star is to the left, and the planet is to the right. The inner and outer radius of the ring corresponds to the stellar and coronal surfaces, respectively. The corona radius is about three times the stellar one. The thick solid line shows the Roche lobe boundary. The solid lines with arrows present the magnetic field lines. It is easy to see that the magnetic field clearly demonstrates four zones marked with corresponding figures. Zone 1 is determined by open stellar field lines beginning on the stellar surface and going to infinity. Zone 2 is determined by open field lines of the planet. In zone 3, the magnetic lines are common to the star and the planet; they begin on the stellar surface and end on the planetary surface. Finally, zone 4 includes the closed lines of the planet. In neutral points, the magnetic field direction is undetermined. In the equatorial plane, these points are denoted as N_1 and N_2. In space, the set of these points forms a neutral line, close to a circle, whose shape is determined by the orientation of the planetary magnetic field.

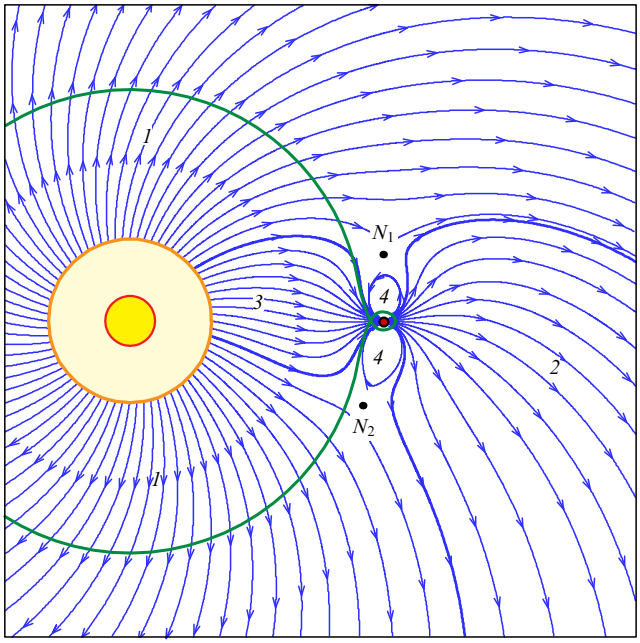

Figure 32. (Color online.) Initial magnetic field distribution in the equatorial plane for $B_* = 10^{-3}$ G. Thick solid line shows the Roche lobe. The star is shown as a colored dot with the inner and outer radii corresponding to the radius of the star and its corona, respectively. The figures mark four magnetic zones. N_1 and N_2 are the neutral points.

The large semi-axis of Mercury is 0.38 a.u. $= 82 R_\odot$. Considering estimates of the Alfvén radius r_A given above, this means that all planets in the Solar System lie in the super-Alfvénic zone of the solar wind. The sonic point, where the wind velocity matches the sound speed, lies even closer to the Sun at a distance of about 0.037 a.u. $= 8 R_\odot$. This suggests that magnetospheres (if present) of the planets of the Solar System have a structure similar to Earth's magnetosphere. They consist of the following main elements: a bow shock, a transitional region, a magnetopause, radiation belts, and a magnetospheric tail.

In the case of hot Jupiters, the magnetospheric structure can be completely different because of their proximity to the host star. To analyze the possible situation, we have processed the actual data for a set of 210 hot Jupiters taken from the database from the site http://www.exoplanet.eu. The set was sampled by the planetary mass ($M_{pl} > 0.5 M_{jup}$, where M_{jup} is Jupiter's mass), the orbital period ($P_{orb} < 10$ days), and the large orbital semi-axis ($A < 10 R_\odot$). In addition, only those planets with all the necessary known parameters were chosen.

The stellar wind model immediately close to the Sun at distances $1 R_\odot < r < 10 R_\odot$ was based on calculations performed in [77]. The density $\rho(r)$ and radial velocity $v_r(r)$ profiles enabled us to calculate for each hot Jupiter the dynamical wind pressure,

$$P_{dyn} = \rho(A) v_r^2(A) \,, \tag{78}$$

and the magnetic pressure,

$$P_{mag} = \frac{B_r^2(A)}{8\pi} \,, \tag{79}$$

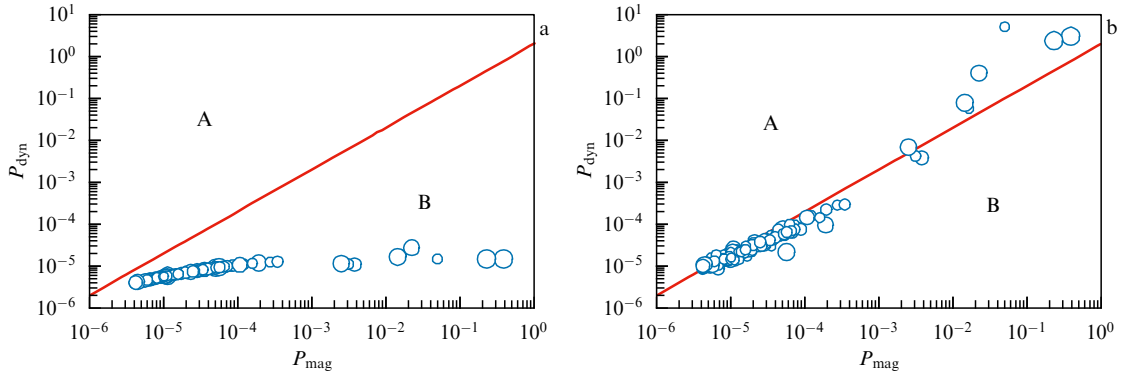

Figure 33. (Color online.) Distribution of hot Jupiters in the $P_{mag} - P_{dyn}$ diagram. (a) Alfvén Mach numbers are calculated using the wind velocity only. (b) Planetary orbital velocities are included. Planetary parameters are taken from the database http://www.exoplanet.eu. Data for 210 hot Jupiters are used. Planets correspond to the centers of the circles. The circle sizes on the logarithmic scale correspond to the planetary mass. Solid line indicates the location of the Alfvén point in the solar wind. A — super-Alfvénic zone, B — sub-Alfvénic zone.

in the planet's orbit. The radial field was calculated as $B_r(A) = B_*(R_\odot/A)^2$ with $B_* = 1$ G. The obtained distribution of hot Jupiters on the two-dimensional plot $P_{mag} - P_{dyn}$ is presented in Fig. 33a. The circles show planets with sizes corresponding to the logarithm of mass M_{pl}. The solid line shows the location of the Alfvén point of the solar wind at which $P_{dyn} = 2P_{mag}$.

It is seen that all hot Jupiters from our set lie in the sub-Alfvénic region of the stellar wind. However, in the planet's co-moving frame, the flow character is determined by both the wind velocity and the planet's orbital velocity. When taking into account the orbital velocity, the dynamical pressure takes the form

$$P_{dyn} = \rho(A)\left[v_r^2(A) + \frac{G(M_* + M_{pl})}{A}\right]. \qquad (80)$$

Note that the planet's orbital velocity depends on both the orbital radius and the mass of the planet. The corresponding diagram is presented in Fig. 33b. The orbital velocity shifts the entire sequence significantly upward to the super-Alfvénic wind zone. Note that most of the planets in this diagram form some regular sequence (the bottom left corner of the plot). These planets are located sufficiently far from the star, where power laws fit the radial density and velocity profiles well. Planets close to the star are spread rather chaotically in this diagram. For such planets, the dynamical wind pressure (80) is mainly determined by their orbital velocities.

As for hot Jupiters with orbits inside the sub-Alfvénic zone, the Alfvénic Mach number $\lambda = v_r/u_A$ is less than unity, and the ratio v_r/u_F, where u_F is the fast magnetosonic speed, is also less than unity, because, clearly, $u_F > u_A$, and hence $v_r/u_F < v_r/u_A$. In other words, near such a hot Jupiter, the stellar wind velocity is less than the fast magnetosonic speed. In the pure gas dynamics, this case corresponds to a subsonic flow around a body when no bow shock emerges. Thus, we conclude that the flow around such a hot Jupiter must be shockless [143]. No bow shock should be present in the magnetospheric structure around such a hot Jupiter.

It should be borne in mind that this distribution was obtained for the solar wind from the quiet Sun model. We assumed the mean surface magnetic field on the Sun is 1 G. Even for the Sun, during its activity cycle, the location of hot Jupiters in Fig. 33b relative to the Alfvén point can change to either side. In reality, each planet from our set is streamlined not by the solar wind but by the host star's stellar wind. Its parameters can be significantly different.This means that the stellar wind flow around the planetary atmosphere should be studied individually for each planet and its host star.

As noted above, the *ionospheric envelope* includes the upper atmosphere of a hot Jupiter consisting of an almost completely ionized gas [103]. A closed ionospheric envelope corresponds to the case where the hot Jupiter's atmosphere lies entirely inside its Roche lobe. An open ionospheric envelope corresponds to the case where the hot Jupiter overfills its Roche lobe to form outflows from the Lagrangian points L_1 and L_2. As the proper magnetic field of hot Jupiters is fairly weak, the magnetopause lies inside the ionospheric envelope. In such a situation, a *shock-induced magnetosphere* (Fig. 34a) and a *shockless-induced magnetosphere* (Fig. 34b) are the most likely.

An induced magnetosphere [142] is produced by currents circling in the upper ionospheric layers. The currents induced in the ionosphere partially screen the wind magnetic field. As a result, the magnetic lines enshroud the planetary ionosphere by forming a specific magnetic barrier or ionopause. The bow shock is set immediately before this barrier. A magnetospheric tail is formed on the nightside that the ionospheric plasma can partially fill up. Unlike a proper magnetosphere (like Earth's or Jupiter's), the magnetic field orientation in the induced magnetosphere is entirely determined by the stellar wind field. As a result, the entire magnetospheric structure tracks the direction to the star when the planet moves in orbit. In the Solar System, this situation for the closed ionospheric envelope corresponds to the Venerian magnetosphere and, to some extent, to the Martian one. The induced magnetospheres with open ionospheric envelopes can arise around comets approaching close to the Sun.

An intriguing situation can emerge in the intermediate case ('grey' zone), where the hot Jupiter's orbit passes close to the Alfvénic point. In particular, in this case, the planet itself can be in the sub- or super-Alfvénic zone of the wind, while the extended outflowing ionospheric envelope can cross the Alfvénic point and partially outflow into the opposite wind zone. This case can be quite common for hot Jupiters, because most of them are found close to the Alfvénic point.

The above analysis enables us to conclude that, near almost all presently known hot Jupiters, the stellar wind velocity is close to the Alfvén velocity. Here, many of them can be even in the sub-Alfvénic zone, where the magnetic

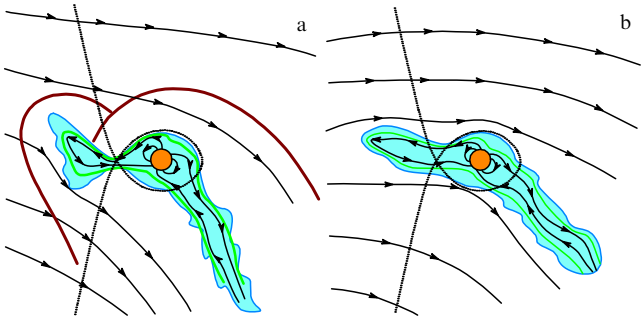

Figure 34. (Color online.) Structure of a shock-induced magnetosphere (a) and a shockless-induced magnetosphere (b) in the case of an open ionospheric envelope of a hot Jupiter. Lines with arrows show magnetic lines. Dotted line indicates the Roche lobe boundary. Colored region corresponds to the planetary gas envelope. Location of the shock wave (outer solid line) and the magnetopause (inner solid line) are presented.

pressure of the wind exceeds its dynamic pressure. This means that the stellar wind magnetic field is an important factor when studying the streamlining of a hot Jupiter's ionospheric envelopes. Therefore, it should be necessarily taken into account both in theoretical models and in observational data interpretation.

The stationary structure of the proper magnetosphere (shocked or shockless) is determined by the total magnetic field of all sources inside it. The main sources include the proper planetary field (for example, the dipole field), the field of induced currents in the magnetopause, and the field of currents in the magnetospheric tail. The Solar System's giant planets (first of all, Jupiter and, to a lesser extent, Saturn) have another characteristic magnetosphere element: the so-called magnetodisk [141], a thin (around 30 km in Jupiter) current layer near the equatorial plane of the magnetosphere. The magnetodisk creates a significant additional dipole magnetic field formed by both its proper currents and induced screening currents. For example, the effective dipole moment of Jupiter's magnetodisk exceeds the proper planet's magnetic moment by 2.6 times. The magnetodisk is located at characteristic distances from $18R_{\rm jup}$ to $92R_{\rm jup}$.

For the magnetodisk to be produced, two factors should be present simultaneously: a rapid rotation of the planet and a source of additional plasma inside the magnetosphere. In the Jupiter system, the magnetosphere plasma is supplied by the Jovian satellite Io. Due to its volcanic activity, a great deal of neutral gas is injected into the magnetosphere; its ionization results in the formation of a plasma mainly consisting of hydrogen, oxygen, and sulphur ions. The centrifugal force caused by the planet's rotation makes the plasma move from the planet along the magnetic lines. As a result, the plasma concentrates near the magnetospheric equatorial plane to form, due to the distortion of the magnetic lines, a thin current layer — the magnetodisk. Paper [177] notes that magnetodisks can appear in magnetospheres of hot Jupiters as well. In this case, the expanding ionospheric envelope of hot Jupiters may be the source of plasma for the magnetodisk.

Consider an Alfvénic surface determined by the balance of the kinetic (rotational) energy of the outflowing plasma and the energy of the proper planetary (dipole) magnetic field. Inside the Alfvénic surface, the energy of the dipole magnetic field is high, and therefore the plasma rotates almost as a solid body together with the field lines. The magnetic field lines themselves are not distorted. Some magnetic field lines near the equatorial plane do not intersect the Alfvénic surface. Consequently, the plasma flowing along these lines always stays inside this region and rotates as a solid body with the magnetic field. This region is called the 'dead zone' [178].

The plasma flowing along the magnetic lines crossing the Alfvénic surface can leave the inner magnetosphere. Outside the Alfvénic surface, the magnetic field energy becomes less than the plasma kinetic energy. Therefore, the centrifugal force accelerates the plasma, and its motion significantly distorts the initial dipole magnetic field. As a result of such a flow, the plasma of the expanding ionospheric envelope approaches the equatorial plane and pulls the planetary magnetic field lines toward this plane. This results in the formation of a thin current layer, because the field lines are oppositely directed above and below the equatorial plane. A magnetodisk will be produced from the ionospheric plasma. Electric currents in the magnetodisk generate an additional magnetic field inside the magnetosphere [179]. Analysis shows that, as a rule, the effective magnetic moment of the magnetodisk exceeds the proper planetary magnetic moment [177]. Note that the formation mechanism of the magnetodisk generally is not related to the presence or absence of a bow shock. Therefore, this element can be present in both shocked and shockless magnetospheres of hot Jupiters.

Figures 35 and 36 present the results of 3D numerical simulations of the flow structure around the hot Jupiter HD 209458b [180]. In these calculations, we have used the numerical model described in [140]. The main model parameters were the same as those described above. The wind magnetic field was defined by formulas (74) and (76). Calculations were performed for two models corresponding to the weak and strong wind magnetic field. The mean magnetic field on the stellar surface was set to be $B_* = 0.5$ G and $B_* = 0.01$ G in the first (strong field) and second (weak field) models, respectively. Considering that the stellar radius is somewhat higher than the solar one, the field in the first model practically corresponds to the mean magnetic field on the solar surface, as follows from comparing the corresponding magnetic moments of the stars.

In the calculations, we have also taken into account the proper planetary magnetic field (70). We have assumed that the magnetic moment of the hot Jupiter HD 209458b is $\mu = 0.1\mu_{\rm jup}$, where $\mu_{\rm jup}$ is Jupiter's magnetic moment. The magnetic dipole axis was tilted by 30° to the spin axis oppositely to the star. As before, in the model, we have assumed that the proper rotation of the star is synchronized with the orbital revolution, and the spin axis is collinear with the orbital angular momentum.

In the first model (strong field), the sub-Alfvénic flow regime is realized. As seen from Fig. 35, in this case, the interaction of the stellar wind with the ionospheric envelope of the planet is shockless. The bow shock does not form around either the planetary atmosphere or the matter expelled from the Lagrangian point L_1. This is clearly seen from the density and velocity distribution (Fig. 35a). The wind magnetic field turns out to be so strong that it blocks the transversal plasma motion in the magnetic field. Therefore, the ejected matter moves towards the star predominantly along the wind magnetic field (Fig. 35b). Consequently, the electromagnetic force caused by the wind magnetic field plays an essential role in this process, comparable to the gravity force, centrifugal force, and the Coriolis force.

In the second model (weak field), the super-Alfvénic flow regime is realized. The stellar wind interaction with the

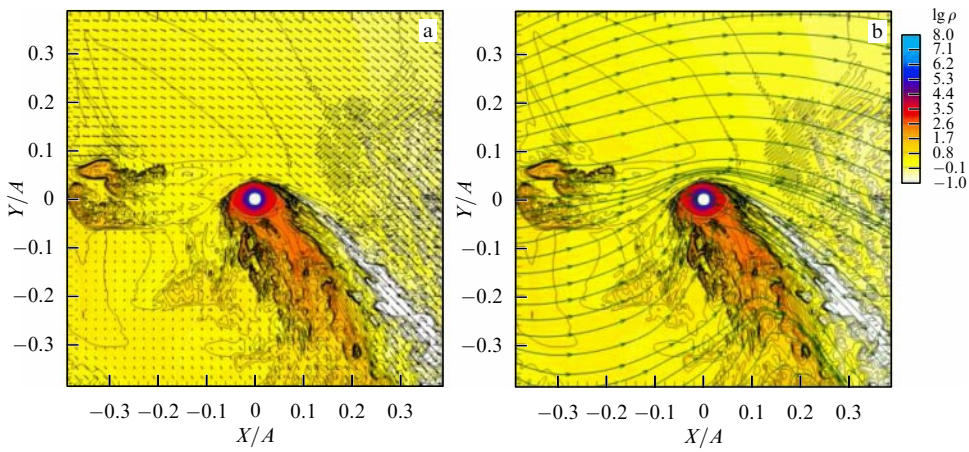

Figure 35. (Color online.) Distribution of density (color gradation and isolines), velocity (a), and magnetic field (b) (lines with arrows) in the orbital plane of a hot Jupiter. Solution is presented for the strong stellar wind magnetic field model ($B_* = 0.5$ G) at the time $0.5P_{\rm orb}$ from the beginning of calculations. Thin light line indicates Roche lobe boundary. Circle corresponds to planetary photometric radius.

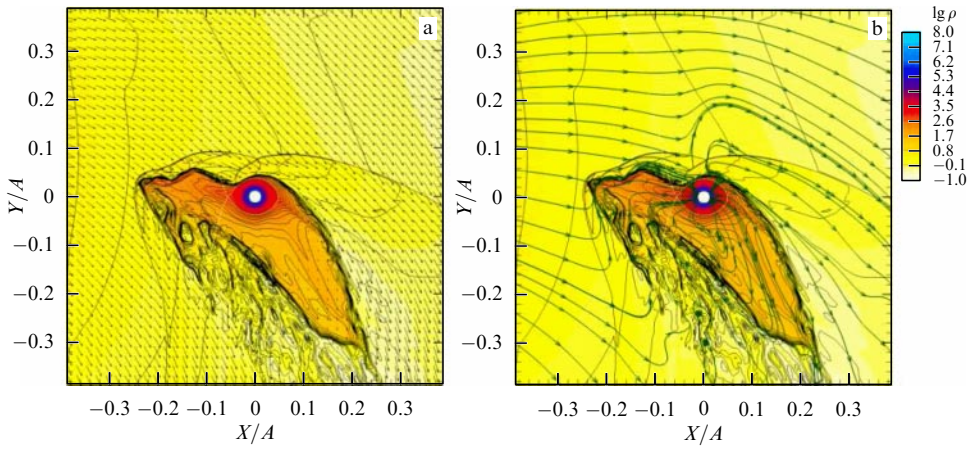

Figure 36. (Color online.) Distribution of density (color gradation and isolines), velocity (a), and magnetic field (b) (lines with arrows) in the orbital plane of a hot Jupiter. Solution is presented for the weak stellar wind magnetic field model ($B_* = 0.01$ G) at the time $0.26P_{\rm orb}$ from the beginning of calculations. Thin light line indicates Roche lobe boundary. Circle corresponds to planetary photometric radius.

planet's ionospheric envelope gives rise to a bow shock, which is clearly seen in Fig. 36. This shock appears to consist of two separate shocks, one of which emerges from the interaction of the wind directly with the planetary atmosphere, and the other, from the interaction with the stream from the Lagrangian point L_1. Inside the Roche lobe, the magnetic field keeps the dipole structure. However, in the flows forming on the day and night side, the magnetic field lines are strongly stretched and distorted. As the stellar wind magnetic field is weak in this case and does not play any significant dynamical role, the flow structure corresponds to a purely gas-dynamic case described in papers [28, 29].

4.3 Sub-Alfvénic flow regime

The sub-Alfvénic regime of the stellar wind flow around the hot envelope of a hot Jupiter has interesting features. An analysis of our calculations (see Fig. 35) shows that, in this case, a new type of hot Jupiter envelope arises, because the strong magnetic field of the stellar wind forces the matter to move along not the ballistic trajectory but the wind magnetic field lines. Clearly, the observational appearances of such envelopes must be different than the super-Alfvénic flow.

The structure of the sub-Alfvénic flow (stellar surface magnetic field $B_* = 0.5$ G) at time $t = 0.5P_{\rm orb}$ from the beginning of calculations is presented in Fig. 35. By that moment, a turbulent magnetospheric tail on the nightside of the planet has been formed. The magnetopause has been formed completely. The stellar wind interaction with the ionospheric envelope outflowing from the inner Lagrangian point L_1 is shockless. The bow shock does not arise around either the planetary atmosphere or the matter ejected from the Lagrangian point L_1. According to the classification proposed by us in paper [140], an induced shockless magnetosphere with an open ionospheric envelope is forming.

One can see wave-like density (and other MHD quantities) fluctuations in the wind around the planet. In our models, these fluctuations arise in the sub-Alfvénic flows, whereas in the super-Alfvénic flows, they are absent [140, 150, 151]. Their appearance can be explained as follows. The velocities of the radial Alfvénic waves propagating in the stellar wind are $v_{\rm r} + u_{\rm A}$ and $v_{\rm r} - u_{\rm A}$. The former waves directly propagate along the magnetic field, the latter in the opposite direction. In the super-Alfvénic zone of the stellar wind, $v_{\rm r} > u_{\rm A}$, and, hence, the velocities of both Alfvénic waves are positive. Therefore, any fluctuations in the stellar wind will be carried out from the computational domain by the moving plasma. In the sub-Alfvénic zone of the stellar wind, $v_{\rm r} < u_{\rm A}$, and, hence, $v_{\rm r} + u_{\rm A} > 0$ and $v_{\rm r} - u_{\rm A} < 0$. In

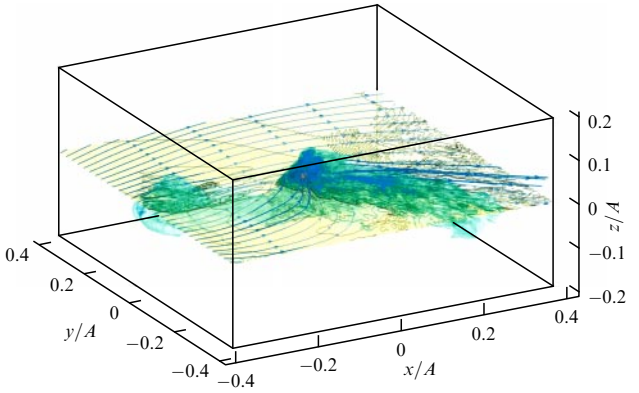

Figure 37. (Color online.) Distribution of the decimal logarithm of density (color gradation and isolines in the orbital plane and isosurfaces in the space) and magnetic field (three-dimensional lines with arrows) in the computational domain at time $t = 0.5P_{\rm orb}$ from the beginning of calculations.

other words, some Alfvénic waves propagate outwards, and others inwards. Also, consider that magnetosonic waves can participate in these processes. A nonlinear interaction of these waves likely gives rise to these density fluctuations.

The wind magnetic field turns out to be strong enough to prevent ionospheric plasma motion across the magnetic lines. The envelope matter moves predominantly along the wind magnetic lines. This means that, in this case, in the process of the hot Jupiter's ionospheric envelope expanding, the electromagnetic force caused by the wind magnetic field is comparable to the gravitational attraction by the star, the centrifugal force, and the Coriolis force. The wind magnetic field is partially distorted by matter flows from the ionospheric envelope but generally preserves its initial structure.

In the orbital plane, the flow is fragmented into separate clumps. By the end of calculations, the envelope itself reaches the left boundary of the computational domain. However, a 3D flow structure analysis suggests that most of the matter in the flow concentrates below the orbital plane. This conclusion follows from Fig. 37, showing the 3D flow structure at the same moment ($t = 0.5P_{\rm orb}$). The logarithmic density distribution is shown both in the planet's orbital plane (in color gradation and by isolines) in accordance with Fig. 35 and by isosurfaces in space. The 3D lines with arrows show the magnetic field lines that begin in the orbital plane from the left side of the computational domain.

The magnetic field geometry can explain such an asymmetric configuration relative to the orbital plane in the direction of the matter flow. In Fig. 35, the magnetic field lines show the structure of the two-dimensional (in the plane $z = 0$) field $(B_x(x, y, 0),\ B_y(x, y, 0))$. In fact, due to the planet's dipole tilt, its south magnetic pole lies below the orbital plane. Therefore, the magnetic field lines coming from the star terminate on the planetary surface below the orbital plane (see Fig. 37). As a result, the envelope matter should slightly deviate down from the planet's orbital plane by moving towards the star along the magnetic lines.

It is also interesting to note that a magnetic barrier forms in front of the planet along its orbital motion direction. It appears as an extended region of magnetic line concentration (see Fig. 35). Inside this region, magnetic field induction increases. The arising of the magnetic barrier is related to the induced field generated due to the interaction of the wind magnetic field with the planet's ionospheric envelope. We stress again that, in all figures, the streamlining of the planet by the stellar wind is shockless. Shocks never emerge either around the planetary atmosphere or the matter outflow from the inner Lagrangian point L_1.

The extended ionospheric envelope of a hot Jupiter forming in the sub-Alfvénic stellar wind flow around the planet is fundamentally different from the envelope forming in both purely gas-dynamical cases [28, 29] and the super-Alfvénic flow [148, 151]. This difference is schematically demonstrated in Fig. 38, showing the star (the filled color ring with the inner radius corresponding to the stellar radius and the outer radius corresponding to the coronal radius), the planet (colored dot), and its extended ionospheric envelope (blue-colored region). The green dashed line shows the Roche lobe boundary in the planet's orbital plane. The arrows indicate the flow direction from the open ionospheric (gas) envelope. In the case of a weak wind field (a purely gas-dynamic or super-Alfvénic flow), the ionospheric (gas) envelope stretches along the ballistic trajectory starting at the inner Lagrangian point L_1. If the envelope is open, the matter stream continues moving along the ballistic trajectory and is likely to form some ring-like structure around the star. This situation is displayed in Fig. 38a.

In the case of a strong wind magnetic field (sub-Alfvénic flow), the ionospheric envelope stretches from the inner

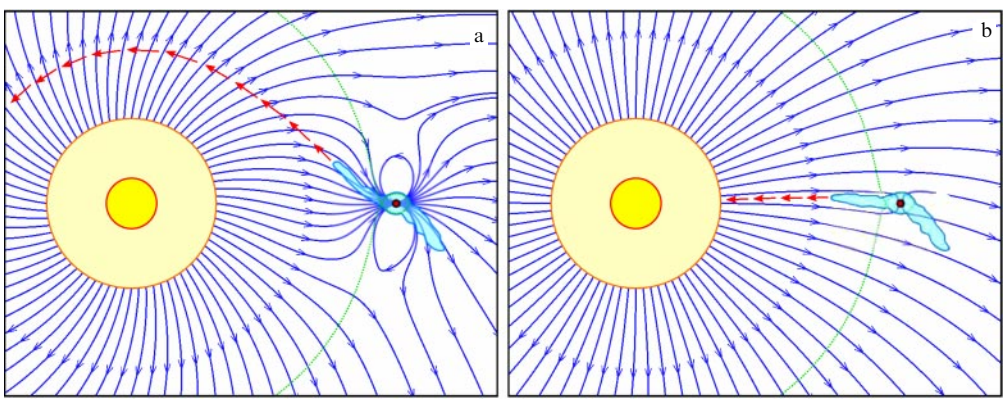

Figure 38. (Color online.) Schematic structure of a quasi-closed envelope of a hot Jupiter in the case of a weak (a) and strong (b) stellar wind magnetic field. The star is marked with a colored small circle. Blue region corresponds to planetary ionospheric (gas) envelope. Arrows indicate the direction of matter outflow from the open ionospheric (gas) planetary envelope. Roche lobe is shown by dotted green line.

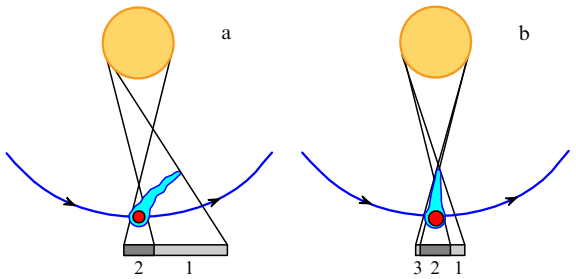

Figure 39. (Color online.) Diagrams demonstrating the difference between observational appearances of a quasi-closed envelope of a hot Jupiter in the case of a weak (a) and strong (b) stellar wind magnetic field. The star and the planet are shown by large and small filled circles. At the bottom, the grey rectangle indicates eclipse phases. 1 — stage of excessive absorption of stellar emission by the envelope of a hot Jupiter before the main eclipse (ingress), 2 — main phase of the eclipse, 3 — stage of excessive absorption by the envelope of the hot Jupiter after the main eclipse (egress).

Lagrangian point L_1 along the wind magnetic lines. As the wind magnetic field in this case is almost radial near the planet, the envelope matter moves directly towards the star. If the envelope is open, the matter flow continues moving along such a trajectory so as to hit the star. This situation is displayed in Fig. 38b. Thus, in a strong wind magnetic field (sub-Alfvénic flow), a new type of ionospheric envelope emerges that completes the envelope classification proposed in papers [28, 29] on the basis of purely gas-dynamic numerical modeling. To distinguish these two envelope types, they can be referred to as *super-Alfvénic quasi-closed* (*open*) *envelopes* (Fig. 38a) and *sub-Alfvénic quasi-closed* (*open*) *envelopes* (Fig. 38b).

As noted above, presently, the observational appearance of extended envelopes around hot Jupiters can be considered to be the detection of excessive absorption in the near-ultraviolet spectrum during a planet's transit. Here, a decreasing flux occurs in both the ingress to eclipse and egress from the eclipse (see, e.g., [17]). Clearly, the different structures of quasi-closed (open) envelopes of hot Jupiters in the super- and sub-Alfvénic flows must appear differently in such observations. In Fig. 39, we schematically present the possible observational differences of these two envelope types. The large and small filled circles show the star and the planet, while the arrows indicate the planet's orbital motion. At the bottom of the figure, the dashed rectangles correspond to different eclipse phases. The main eclipse phase (the transit) is marked by 2. In the case of a weak magnetic field (Fig. 39a), the extended envelope of a hot Jupiter outflowing along the ballistic trajectory should produce excessive absorption before the beginning of transit (ingress, marked by 1). After the termination of transit, this envelope does not touch the disk limb and does not produce additional absorption. However, in this case, some excess ultraviolet absorption can be due to the planet's magnetospheric tail.

In the case of a strong wind magnetic field (Fig. 39b), the extended envelope of a hot Jupiter outflowing towards the star along the wind magnetic lines must produce excessive absorption both before the transit (ingress, 1) and after it (egress, 3). The duration of both stages must be almost the same. Deviations from the strict symmetry (the egress stage is somewhat shorter than the ingress one) are due to the effects of inertia forces on the dynamics of matter and the presence of the azimuthal magnetic field component. In addition, as in the previous case, the magnetospheric tail can also cause some excessive absorption after the planet's transit.

Considering the results obtained, we can note interesting observational features of the transits of some warm Neptunes. For example, paper [181] models the transit of GJ436b in the Ly-α line. The obtained transit depth and light curve parameters at the ingress stage are consistent with observations. However, the post-transit turned out to be too long compared to observations. The authors of that paper note that the wind magnetic field could be responsible for this discrepancy. Another warm Neptune, GJ3470b (see, e.g., [182]), demonstrates an even shorter post-transit, although the planet, apparently, should have a long tail of planetary matter extending along the orbit. Thus, the model we describe in the present paper can open up additional possibilities to probe the parameters of stellar winds from the host stars of hot Jupiters. In particular, this can provide new information on the properties of the magnetic field in stellar winds.

4.4 Development of MHD models: necessary steps

Our first papers [28, 29] used a purely hydrodynamic approach to model the structure of extended envelopes around hot Jupiters. However, the analysis in this section suggests that that is not sufficient. A more precise model should include the magnetic field. It must take into account both the proper magnetic field of the planet and the wind magnetic field. The calculations presented above show that taking into account the magnetic field can significantly affect the structure of extended envelopes around hot Jupiters (which is crucial for interpreting observations) and the long-term evolution of these exoplanets.

It appears worthwhile to further develop the MHD models by including additional effects. First of all, we note that our numerical model has ignored magnetic viscosity. However, in some parts of the flow, the magnetic field diffusion can be important. In particular, the Bohm diffusion [183] with the magnetic viscosity

$$\eta_{\mathrm{B}} = \frac{1}{16}\frac{ckT}{eB}\,, \tag{81}$$

where c is the speed of light, and e is the elementary charge, can develop on the dayside at the boundary between the zones with the planet's open and closed magnetic field lines. In these regions of the hot Jupiter's magnetosphere, the magnetic field reconnection should efficiently occur, as in Earth's magnetosphere [141]. Similar processes should take place in the magnetospheric tail on the night side. The artificial viscosity has been responsible for all these effects in our calculations, which is determined by the difference scheme used and the grid structure. We propose including the Bohm magnetic viscosity into our numerical model to better treat these processes in future studies.

In our numerical calculations of the stellar wind flow around the envelopes of hot Jupiters, we have not taken into account the possible sectorial structure of the stellar wind magnetic field (see, e.g., [169]). Our studies have been focused on the effects of the global wind parameters and the proper planetary magnetic field. However, the effects of the planet crossing the current layer and the polarity changing are obviously important and should be considered. In particular, they can significantly perturb the planet's magnetosphere and hence change the mass-loss rate. In modeling the planet crossing through the current layer when the wind magnetic field polarity changes, not only should the model of the

current layer be specified, but also the magnetic viscosity should be taken into account.

The model of interaction of the magnetized stellar wind with the extended envelope of a hot Jupiter must be consistent with the wind. In our calculations, as a rule, we have used an approximate wind model, in which its radial velocity is constant in the computational domain. This approximation is justified in a purely gas-dynamical case. In a magnetized stellar wind, it does not allow us to compute the location of the Alfvénic point correctly. This is especially apparent in modeling the flow structure in the transitional (grey) zone. In the axially symmetric approximation, it is possible to use the MHD wind model described in [171]. In this case, the calculation of the radial dependence (distance to the star) of the MHD quantities reduces to numerically solving a system of algebraic equations. We have already attempted to calculate the MHD structure of the stellar wind around the hot Jupiter HD 209458b in this model [152].

In addition, global problems related to the generation of the proper magnetic field in the planetary atmosphere remain unaccounted for. However, to this end, it is necessary to simultaneously calculate the dynamics of the extended envelope and the atmosphere, which is an insurmountable problem as yet. Despite the progress in our modeling envelopes and atmospheres of exoplanets, the models now describe only separate processes in the exoplanets. The next logical step is creating a unified self-consistent model capable of simultaneously describing both the inner structure of the atmosphere and the extended envelope interacting with the stellar wind. Taking into account suprathermal particles (with a kinetic energy excess) in the aeronomical model of the upper atmosphere of an exoplanet (see Section 2) allows us to calculate the principal characteristics of the atmospheric gas self-consistently, including the density, temperature, chemical composition, cooling and heating rates, atmospheric glow excitation rates, and rates of thermal and suprathermal dissipation of the atmosphere. The combination of the aeronomic model with the 3D MHD model described in this section will enable us to obviate the need to set artificial boundary conditions in envelope studies, to estimate more correctly the mass-loss rate by hot exoplanets, and to assess their possible observational appearances depending on the parameters of the planet, of its atmosphere, and of the host star.

5. Effect of stellar activity on envelopes of hot Jupiters

In the previous sections, we have discussed the fact that envelopes of hot Jupiters can extend far beyond the planet's Roche lobe; here, the dynamical pressure of the stellar wind keeps the stable size and location of the envelope. The HJ envelopes are weakly bound gravitationally with the planet. Even a slight variation in the stellar radiation and/or stellar wind can significantly change their structure and affect the mass-loss rate.

The Kepler Space Telescope launch heralded a new era in studies of flares of Sun-like stars. In particular, the statistical properties of strong flares of such stars were calculated for the first time [184–186]. For solar-like stars, flares with an energy of 10^{33} erg, when the XUV intensity increases by ~ 2 orders of magnitude over a timescale of half an hour, were found to occur once every 500–600 years on average [186]. At the same time, a solar-like star was found that demonstrates such flares once every 100 days [185]. Such strong flaring activity must affect the HJ envelopes significantly. Moreover, even inactive late-type stars, like the Sun, have a stellar wind that can sharply vary. The strongest solar wind perturbations are due to coronal mass ejections (CMEs). In solar CMEs, the characteristic mass of plasma injected into the interplanetary medium is around 10^{15} g, the mean total energy is about 10^{31} erg, and the propagation velocity varies in the range of 20–3000 km s^{-1} with a mean value of about 500 km s^{-1} [187, 188]. The mean velocity and rate of solar CMEs change during the solar activity cycle. Even for a relatively quiet Sun, the rate of CMEs is quite high, from ~ 0.5 a day at the solar minimum to ~ 4 a day at the solar activity maximum [188].

In this section, based on the results of our calculations [79, 189–194], we consider in a consistent manner the effect of CMEs on HJ envelopes, focusing on changes in the structure, observational properties of the envelopes, and their evolutionary status.

5.1 Effect of a stellar flare on the dynamical state of the atmosphere

5.1.1 One-dimensional model. The modeling of the gas-dynamic response of an atmosphere on a UV flare requires the correct calculation of the heating and modeling of chemical processes, which is difficult in the full 3D setup. To model the atmospheric reaction on the flare, we have elaborated earlier on a one-dimensional aeronomic code [75, 195]. In this code, the atmosphere of a giant planet with a primary atmosphere is modeled along the line connecting the star's and the planet's centers, corresponding to the maximal irradiation. The code includes a chemistry calculation with nine components (H, H_2, e^-, H^+, H_2^+, H_3^+, He, He^+, and HeH^+) and 19 chemical reactions among them. The absorption is calculated in the extreme UV (100–1150 Å) and soft X-ray (10–100 Å) bands. The spectrum is split into energy 'bins.' The code also models the heating by suprathermal and super-thermal photoelectrons.

In papers [79, 191], this model was used to calculate the dynamical response of the atmosphere of HD 209458b to a flare from the host star. The calculations were carried out for a strong stellar flare with parameters defined in papers [196, 197]. The calculations assumed that the extreme UV radiation from the star increased by 100 orders of magnitude at the flare beginning and stayed constant over the entire flare duration (24 min).

As expected, one of the apparent results of the flare effect on the hot Jupiter's atmosphere is local heating that increases the atmospheric gas temperature. The local atmospheric heating due to extreme UV absorption leads to a dynamical response — the formation of two shocks propagating inward and outward in the atmosphere of the hot exoplanet. The change in the dynamical state following the stellar flare is presented in Fig. 40.

Figure 41 shows the temperature change at the radial profile peak and the temperature peak height as a function of time from the stellar flare beginning. The dashed lines show the parameters of the inner peak caused by the inward shock. Note that the temperature peak height (radial distance) decreases on a timescale of shorter than 30 min during the dynamical response of the atmosphere on the stellar flare.

To assess the possibility of the observational appearance of a stellar flare on the upper atmosphere of a hot exoplanet, we have estimated the atmospheric luminosity in the Ly-α line

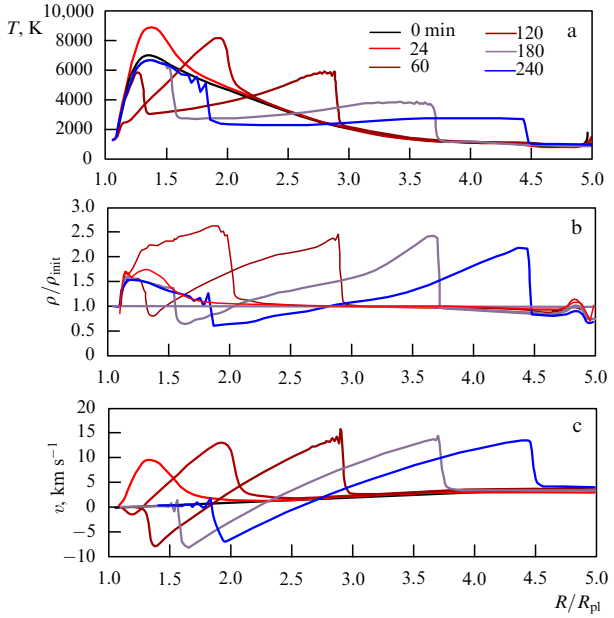

Figure 40. (Color online.) Dynamical state change due to a stellar flare. Shown are radial profiles of the temperature (a), ratio of mass density in the current state to gas density before the flare (b), and velocity (c) in the atmosphere of hot Jupiter HD 209458b before (0 min) and during the stellar flare (24 min), before the atmospheric shock break-out (24–180 min), and at the atmosphere relaxation stage (180–240 min).

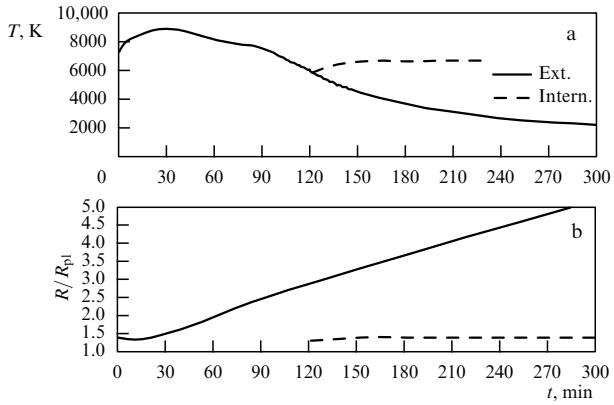

Figure 41. Change in the radial profile of the temperature peak (a) and the temperature peak height (b) as a function of time from the flare beginning.

using calculations of the hydrodynamical characteristics of the atmosphere (see Fig. 41). These calculations enabled determining the source function as the Planck function at the local temperature in each cell of the computational domain by assuming the LTE. Next, considering the radial distribution of atomic hydrogen, we have estimated the atmospheric absorption of local sources in the Ly-α line, enabling the calculation of the Ly-α line profile at the outer boundary of the exoplanet atmosphere.

Figure 42 presents the Ly-α line profiles before, during, and after the stellar flare. The calculations suggest that at the outer boundary of the atmosphere of hot Jupiter HD 209458b, a double-hump Ly-α profile arises; 60 and 180 min after the flare, features in the line profile appear reflecting the shocks propagating in the atmosphere.

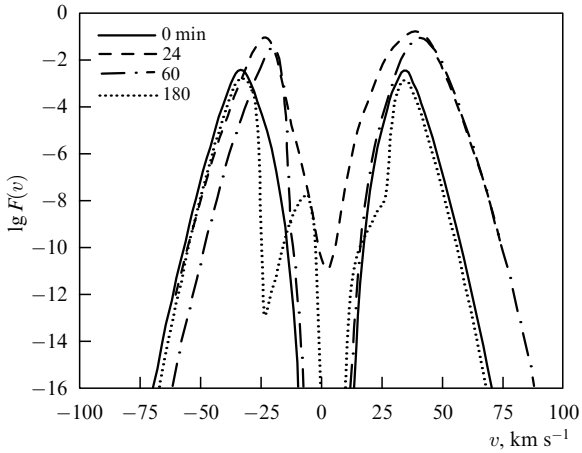

Figure 42. Atmospheric luminosity profiles of the hot Jupiter HD 209458b in the Ly-α line at the outer atmospheric boundary before (solid lines), during (dashed line), and after (60 min — dashed-dotted line; 180 min — dotted line) a stellar flare.

Figure 43 shows how the integral luminosity of the atmosphere of hot Jupiter HD 209458b in the Ly-α line changes due to the dynamical response of the atmosphere to the stellar flare and after its termination.

Note that the Ly-α energy flux from the atmosphere of hot Jupiter HD 209458b is estimated to be $\sim 2.0 \times 10^3$ erg cm^{-2} s^{-1} 180 min after the stellar flare. At the same time, the energy flux in this line from the host star is $\sim 5.6 \times 10^3$ erg cm^{-2} s^{-1}. In order to compare these energy fluxes in the Ly-α line, it is necessary to normalize the energy flux emitted by the atmosphere of HD 209458b to the surface area ratio of the planet and the host star, i.e., by the factor $f = (R_{\rm pl}/R_{\rm star})^2$ approximately equal to 10^{-2}. Correspondingly, the Ly-α flux ratio from the HD 209458b atmosphere and the host star is about 10^{-5}. Figure 43 suggests that this ratio can increase by several orders of magnitude during the stellar flare. As modern photodetectors enable registering such flux ratios, it is possible to observe the appearance of shocks due to the dynamical response of the atmosphere to the stellar flare.

5.1.2 Three-dimensional model. Paper [193] used a 3D gas-dynamical model to compute the flow of matter ejected from the atmosphere due to heating by a stellar flare.

The flare was modeled as a short-time increase in the XUV (10–1150 Å) radiation intensity. Flares with different intensities have different durations. For example, a flare with an intensity increased by a factor of 10 lasts for 12 min; 100-fold and 1000-fold intensity flares last for 24 and 30 min, respectively. The assumption that the radiation intensity increases simultaneously in all model wavelength ranges during the flare is physically acceptable for hydrogen-helium envelopes and solar-type host stars. The constant time profile of the flare is another model simplification, an assumption that does not affect the results, because the flares are short enough, and the atmosphere hardly reacts to the heating during the flare. The test calculations showed that, for this problem, similar to the stationary solution, the radiation pressure does not affect the solution significantly and can be ignored, at least for the given planet.

The calculations assume that the proper rotation of the planet is synchronized with its orbital period. The initial

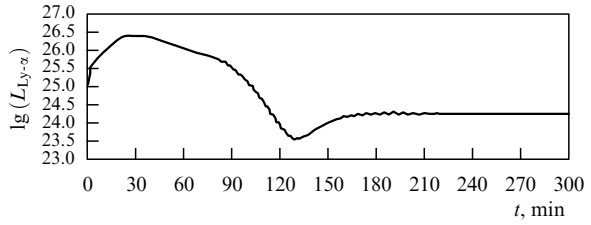

Figure 43. Change in the integral atmospheric luminosity of the hot Jupiter HD 209458b in the Ly-α line at the outer atmospheric boundary before, during, and after a stellar flare.

condition in this study is taken from paper [29]; it corresponds to a closed atmosphere with a temperature of $T_{\rm atm} = 7000$ K and a density at the photometric radius of $n_{\rm phot} = 5 \times 10^{10}$ cm^{-3}. As nothing is known about the stellar wind in this system, we used the solar wind parameters at a distance corresponding to hot Jupiter HD 209458b: particle number density $n_{\rm wind} \sim 10^4$ cm^{-3}, velocity $v_{\rm wind} = 100$ km s^{-1}, and temperature $T_{\rm wind} = 7.3 \times 10^5$ K [77]. The mass-loss rate in this stationary system is $\sim 10^9$ g s^{-1}, predominantly via the second Lagrangian point L_2 [99].

The calculations were performed on a nonuniform Cartesian grid $40 \times 40 \times 20\, R_{\rm pl}$ in size, condensed to the planet's center. The cell size at the planet's photometric radius did not exceed the model atmosphere height scale. We used the Roe numerical scheme [107]; the entropy fix was based on the LLF method. We also used the TVD correction to increase the space approximation degree in the smooth solution regions without smearing shocks [108].

Figure 44 demonstrates the distributions of gas-dynamical variables at the height $R_{\rm max} = 1.3 R_{\rm pl}$ in the planetary atmosphere obtained in the 1D aeronomic model. This height corresponds to the temperature profile maximum in a stationary atmosphere. In correspondence to the 1D model data, the temperature at the inner boundary $R_{\rm max}$ was set as follows. At the under-stellar side of the planet during the flare and the subsequent relaxation to the initial conditions, the boundary conditions were

$$T(t, R_{\rm max}) = T_{\rm atm} + \left(T_{\rm aer}(t, R_{\rm max}) - T_{\rm atm}\right) \cos\phi\,,$$
$$\rho(t, R_{\rm max}) = \rho_{\rm init} + \left(\rho_{\rm aer,\,rel}\,(t, R_{\rm max}) - 1\right) \rho_{\rm init} \cos\phi\,, \quad (82)$$
$$\mathbf{v}(t, R_{\rm max}) = v_{\rm aer}(t, R_{\rm max}) \cos\phi\, \frac{\mathbf{r}}{r}\,.$$

Here, $T_{\rm aer}(t, r)$, $\rho_{\rm aer,\,rel}(t, r)$, and $v_{\rm aer}(t, r)$ denote the temperature, relative density, and radial velocity of matter for the atmosphere response to the flare as obtained in the 1D aeronomic model presented in Fig. 44. The angle ϕ counts out between the vector directed to the given point ($\mathbf{r}$) and the x-axis coincident with the orbital axis of the system.

Note that such boundary conditions are the simplest ones provided that only the calculation for the under-stellar point is available. This distribution is not fully physically justified: for example, according to it, heating at the planet's terminator will be zero, which is not the case. Other effects, such as winds in the low atmospheric layers, are also ignored in this setup. However, these boundary conditions give a reasonable approximation for the 3D modeling of the interaction of shocks propagating in the atmosphere with the surrounding stellar wind.

Although the characteristic model flare durations are less than half an hour, perturbations in the atmosphere propagate

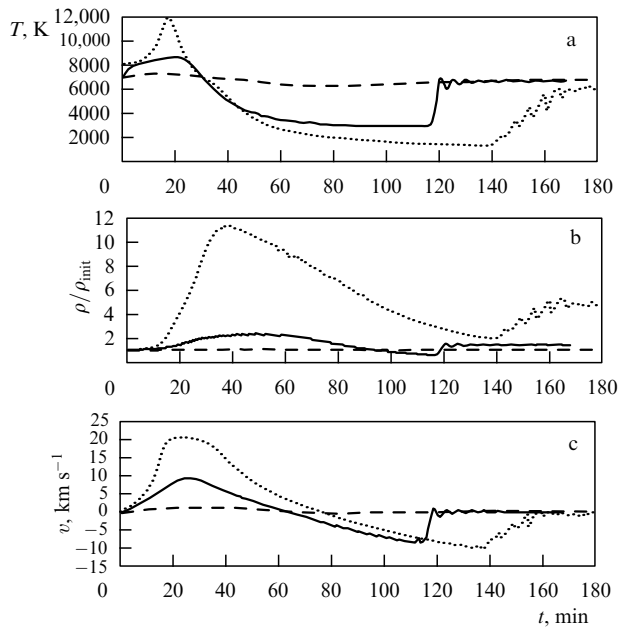

Figure 44. Time profiles of gas-dynamic quantities during pulse UV-heating at height $R_{\rm max} = 1.3 R_{\rm pl}$. This point corresponds to the temperature peak of the stationary solution. (a) Temperature, (b) relative velocity, (c) atmospheric gas velocity at the fixed height. Profiles for flares lasting for 12, 24, and 30 min for a weak (10-fold amplification), moderate (100-fold amplification), and powerful (1000-fold amplification) flare are shown by the solid, dashed, and dotted lines, respectively.

much longer. For example, for the middle-intensity flare and the outward shock velocity $v_{\rm wave,\,1} = 23$ km s^{-1}, the characteristic time of the perturbation propagation up to the atmospheric contact discontinuity is $\tau = 4R_{\rm pl}/v_{\rm wave,\,1} \sim 5$ h, where $4R_{\rm pl}$ is the longitudinal Roche lobe size for the model planet. The time of interaction of the ejected atmospheric mass with the stellar wind, which results in matter sweep by the stellar wind, is tens of hours.

Figure 45 presents the results of modeling the atmosphere dynamics for a middle-intensity flare with a 100-fold XUV intensity increase lasting 24 min. Figures 45a–f correspond to the initial solution and five subsequent time moments during the mass ejection from the atmosphere. Figure 45b, corresponding to $t = 4.6$ h after the flare beginning, which is much longer than its duration, suggests that the atmosphere 'swells' at the under-stellar point during the break-out of the shock formed deep inside the atmosphere. As a result, the visible size of the atmosphere will increase for the observer. Later on, the expelled matter will interact with the incident stellar wind; part of the matter will be carried away downstream, while another part can return to the atmosphere.

Figure 45c, corresponding to the moment $t = 8.4$ h after the flare beginning, shows that the matter ejected towards the star passes through the vicinity of the Lagrangian point L_1 to form a stream, which, as seen from Fig. 45d, is withdrawn and carried away from the planet downstream from the stellar wind. After later perturbations, the atmosphere relaxes to its initial form.

Figure 46 presents the result of modeling a low-intensity flare with a 10-fold flux increase over 12 min. This flare is weaker by one order of magnitude than the previous case. The heating wave in the atmosphere also has a significantly lower velocity, 15 km s^{-1} vs. 23 km s^{-1} in the previous case, and power. In this solution, the flare effects are almost invisible. It is seen that the form of the contact discontinuity in the

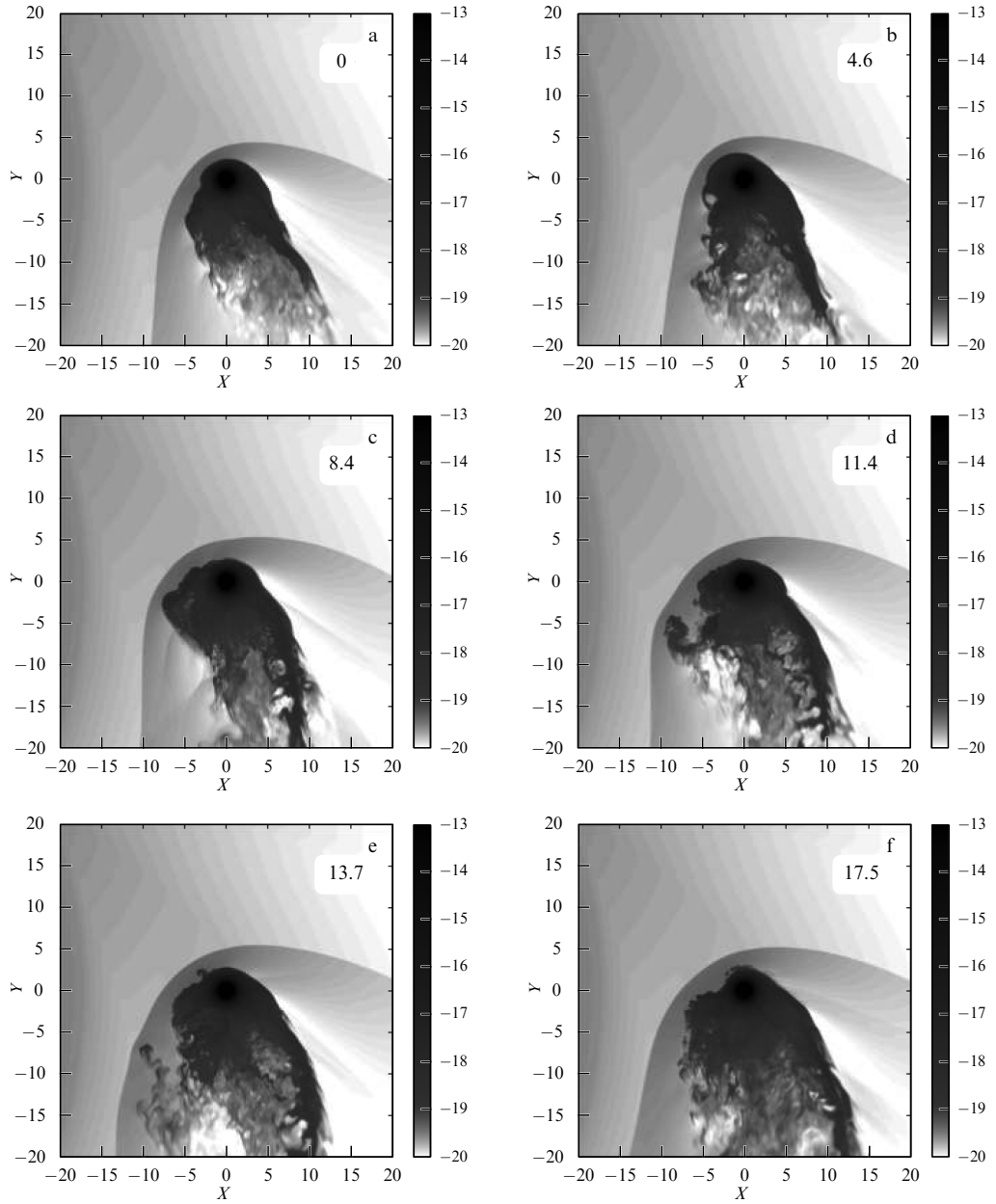

Figure 45. Atmosphere dynamics during atmospheric ejection caused by heating by a moderate-amplitude flare. Shown is the density distribution in the orbital plane of the system on a logarithmic scale. All distances are in units $R_{\rm pl}$. In each figure, the time after the flare beginning is shown in the top right corner. In Fig. a, the stationary solution from paper [29] is presented.

atmosphere changes after the flare, but this process does not affect either the mean mass-loss rate or the observational appearances of the envelope.

The results of modeling a 1000-fold flare lasting 30 min are shown in Fig. 47. Here, the atmospheric heating is accompanied by a very powerful mass ejection, and the expanding atmospheric matter shifts the surrounding stellar wind. Furthermore, it is seen that, ~ 15 h after the flare, the ejected atmospheric matter is collimated along the streamline in the Roche potential of the system. After $t \approx 20$ h, the flare goes out of the computational domain.

3D calculations suggest that, after the flare, the characteristic size of the hot Jupiter's envelope will increase, which can be potentially observed. The 3D modeling enabled us to calculate the photometric light curve in the Ly-α line for a middle-intensity flare. The calculation of absorption for the photometrical curve was carried out using formulas from paper [103], taking into account the Doppler shift and nonequilibrium ionization.

Figure 48 suggests that the matter ejected after the flare increases the eclipse depth by a few percent (from 4% to 6%). This effect lasts for about 2 h, whereas the transit duration is around 3 h. Since eclipse deepening by the planetary envelope occurs much later than the flare — for a middle-intensity flare, the eclipse 'time delay' is ~ 5 h — it will be possible to note the eclipse increase in the stationary photometric light curve.

Note that, for this effect, the perturbation propagation velocity in the atmosphere depends on the flare intensity. The stronger the flare, the faster the perturbation propagates, and the earlier and more pronounced the increased absorption. This paper used the parameters of a closed atmosphere; the solution with a quasi-closed envelope will produce a much larger eclipse corresponding to observations.

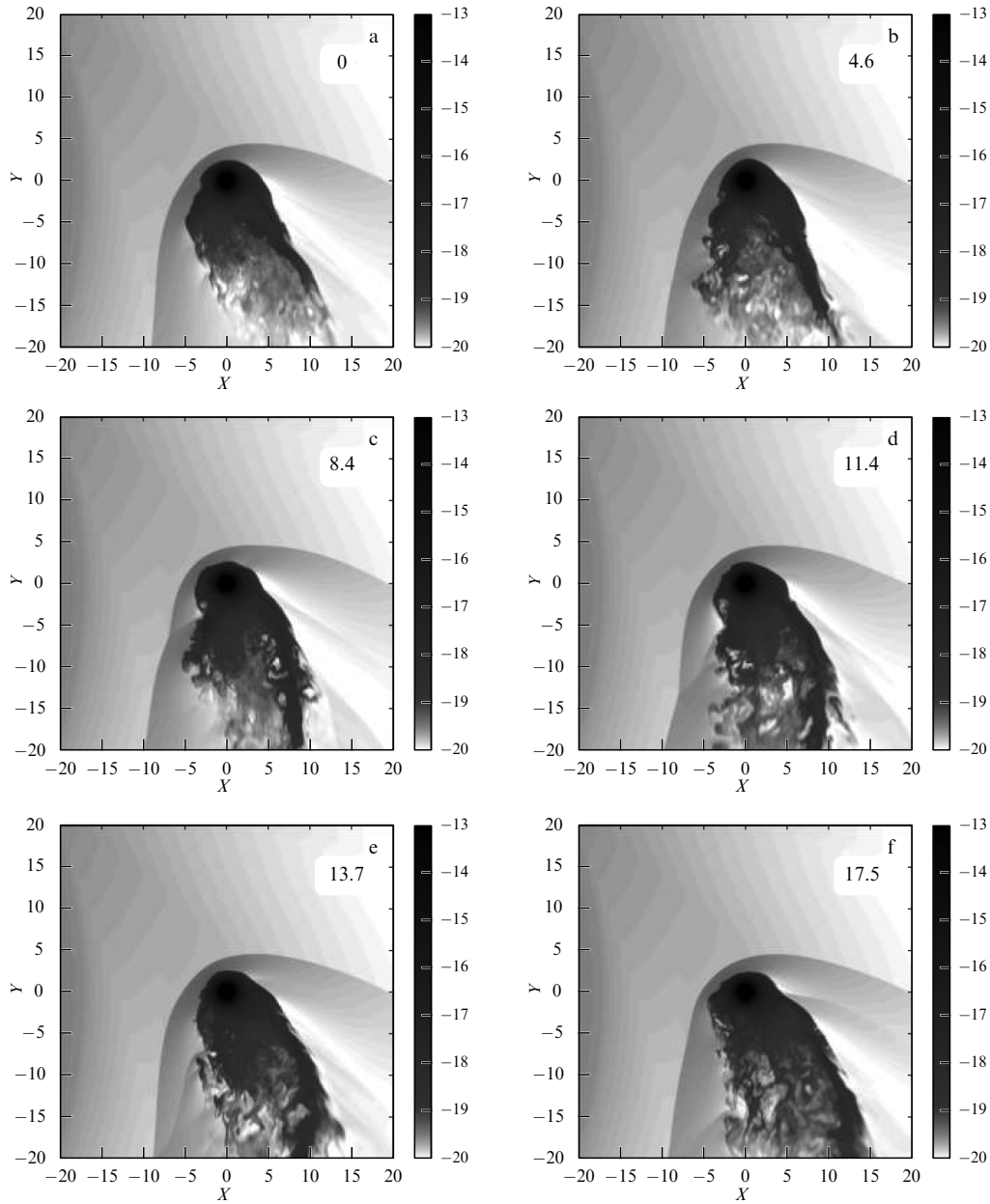

Figure 46. The same as in Fig. 45 for a weak flare.

Another physical effect is the mass loss from the atmosphere after the host star flare. The modeling enabled us to plot the mass-loss rate as a function of time shown in Fig. 49 on a logarithmic scale. The mass-loss rate is calculated as the atmospheric matter flux through the sides of a $12 \times 12 \times 16\, R_{\rm pl}$ cube centered on the planet. Here, the atmospheric matter is traced using an additionally computed transfer equation.

The presented plot suggests that the flux for the low- and middle-intensity flares increases about 15 h after the flare; for a powerful flare, the ejected matter arrives at the boundaries of the computational cube already after three hours. This is because the observed flux for the powerful flare represents the expanding atmospheric matter pushing the stellar wind, as seen in Fig. 47. The ejected matter interacts for a significant time with the stellar wind inside the computational domain for less powerful flares. Only after that is it carried away downstream to enhance the mass loss.

It is possible to calculate the total mass loss due to the flare by integrating the instantaneous mass loss rate. For flares with different intensities, the total mass loss is $\Delta M_{10} = 4 \times 10^{13}$ g, $\Delta M_{100} = 2 \times 10^{14}$ g, and $\Delta M_{1000} = 2 \times 10^{15}$ g for the first, second, and third flares. Here, the prolonged duration of the enhanced mass loss is ~ 30 h in all cases. For the middle-intensity flare, the mean mass-loss rate exceeds the stationary value by only a factor of three, and for a weak flare, by only a factor of 1.5. Therefore, flares with a UV intensity growth of less than one order of magnitude do not appreciably improve the rate of mass loss.

Flares with different amplitudes occur at different rates. For example, in a solar-type star, in the XUV range, the model 100-fold intensity flare occurs once every hundred years. On the other hand, the 10-fold and 1000-fold flares occur once every ten and thousand years, respectively. Considering these rates, we can estimate the total flare-induced mass loss over one billion years to be $\Delta M \sim 10^{22}$ g. As in the stationary wind with given parameters, where the atmospheric mass loss rate is $\dot{M} = 1 \times 10^9$ g s^{-1} [99], the planet loses $\Delta M = 3 \times 10^{25}$ g over this time. These values are

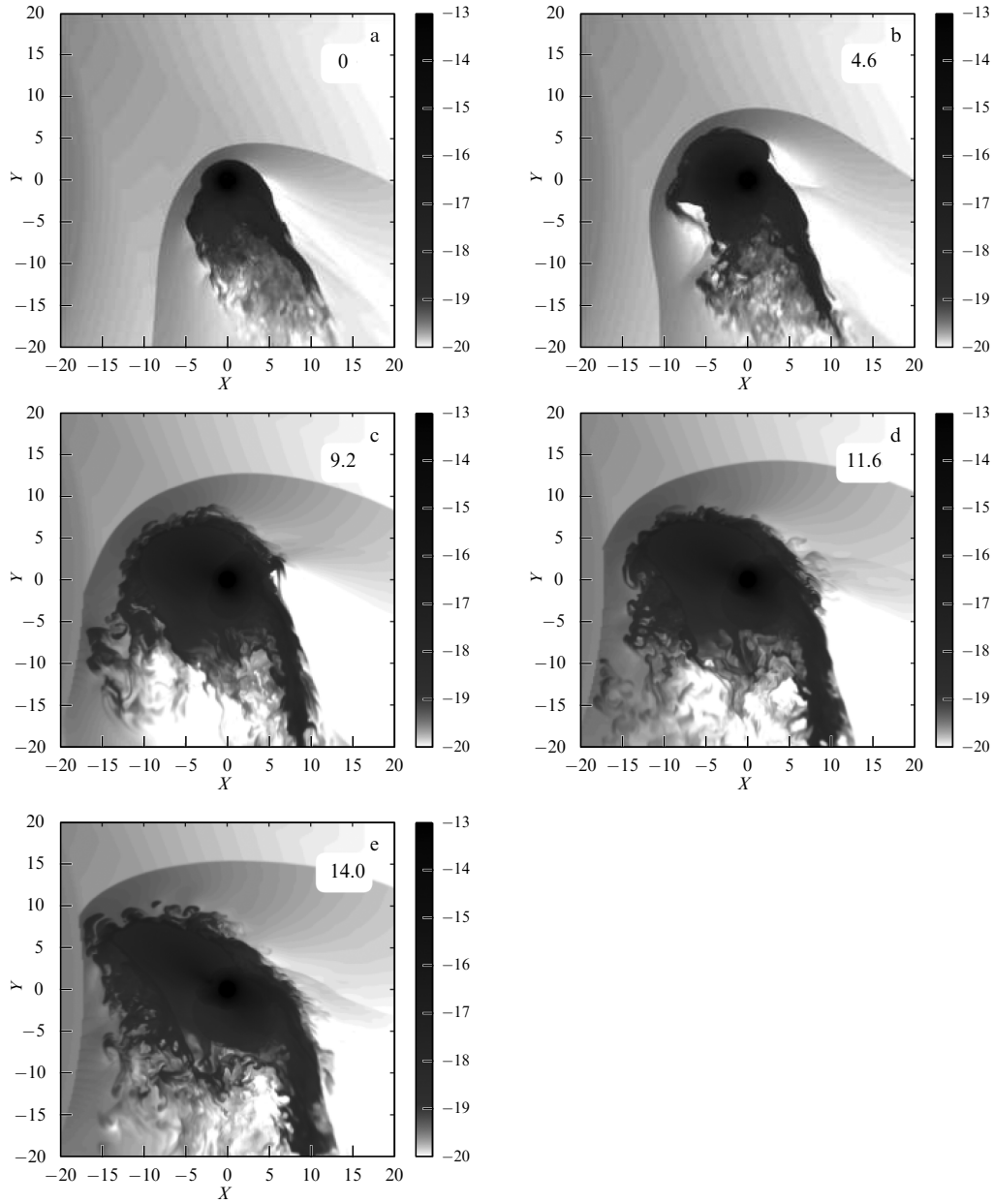

Figure 47. The same as in Fig. 45 for a strong flare.

comparable; therefore, one should take into account this mass-loss mechanism in evolutionary studies of planets of this class.

5.2 Interaction of coronal mass ejections with extended envelopes of hot Jupiters

The effect of CME from low-mass stars on the secondary atmospheres of Earth-like exoplanets in the habitability zone was considered, for example, in papers [198, 199]. These papers showed that planets with a weak magnetic field could lose hundreds of bars of atmospheric pressure due to CME. Paper [200] investigated the interaction of CME with planetary magnetic fields and showed that planets orbiting dwarf M-stars should possess a few dozen magnetic fields to prevent the destructive effect of CME on the atmosphere. For hot Jupiters orbiting solar-like stars, the magnetic fields do not exceed a few gauss [68, 125–127]; therefore, CME can play an essential role in the planetary atmosphere evolution.

Papers [189, 190, 194] presented results of 3D gas-dynamic simulations of the process of CME passing through the extended envelope of a hot Jupiter. The results of modeling of HD 209458b from paper [29] were taken as boundary conditions, and the CME parameters were taken to be solar-like at the exoplanet distance. For example, paper [190] used data corresponding to the CME of April 12, 1998 [201]. The unperturbed wind parameters at the model planet's orbit were chosen following paper [29]: velocity of 100 km s^{-1}, temperature of 7.4×10^5 K, and density of 10^4 cm^{-3}. The CME velocity was assumed to be 1300 km s^{-1} according to paper [202]. The typical CME consists of three phases: the shock and the early and late CME, during which the wind parameters significantly change. Also, perturbations change as the CME propagates. Therefore, to find the CME characteristics at the distance of the HD 209458b orbit, the solar CME parameters determined at the Earth orbit should be recalculated. The CME velocity, density, and temperature

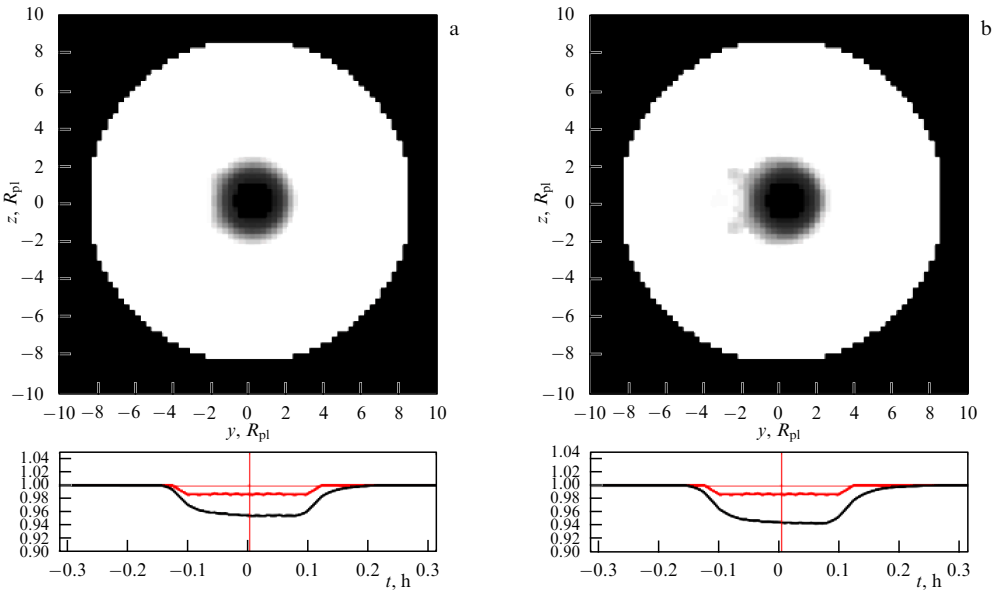

Figure 48. (Color online.) Increase in Lyman-alpha line absorption due to atmospheric ejection for a 100-fold flare. (a) Lyman-alpha eclipse for the stationary solution and (b) at the moment of maximum eclipse $t = 5$ h after the flare beginning. The eclipse is enhanced by several percent on a time scale of a few hours. The time in hours is along the abscissa. Thick red line indicates the eclipse due to the planetary disk alone (1.8%).

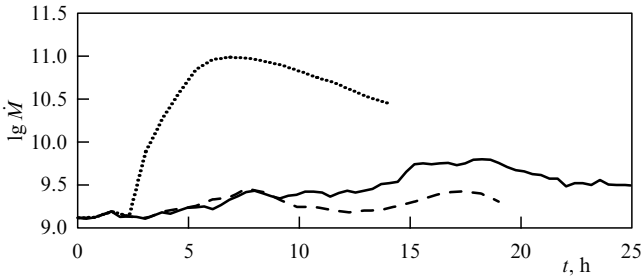

Figure 49. Mass-loss rate after flares with different intensities; solid, dashed, and dotted lines are for moderate, weak, and powerful flares, respectively. The time in hours is along the abscissa.

profiles, recalculated in paper [190] for the corresponding distance, are presented in Fig. 50. Three different speeds, 3000, 1300, and 600 km s^{-1} for a fast, moderate, and slow CME, were considered. Their durations were 1.3, 3.0, and 6.4 h, respectively.

All three CMEs similarly affected the flow, so that in Fig. 51 we show only the solution for the fast CME lasting 1.3 h. This figure displays the density distribution in the equatorial plane for nine moments, three for each CME phase. The time after the start of calculations is shown in the upper right corner. The dynamical wind pressure in the CME shock is $\sim 9 \times 10^3$ of the undisturbed wind value, so that, at the first phase, the CME shock virtually completely destroys the extended envelope (the flow from the L_1 point vicinity), not disturbing, however, the atmosphere inside the planet's Roche lobe. The dynamical pressure at the next phase of the early CME is lower ($\sim 8 \times 10^2$ of the unperturbed wind value), but this pressure turns out to be sufficient to lock the atmosphere inside the Roche lobe of the planet and ultimately block the flow from the L_1 and L_2 points. A similar picture can be observed during the third phase (the late CME), where the dynamical wind pressure is $\sim 3.6 \times 10^3$ of the undisturbed value. Figure 52 shows the mass-loss rate as a function of time for three solutions. In this case, the mass-loss rate is

Table 3. CME duration, total mass loss, and mean mass-loss rate by an extended envelope during planetary passage through a CME.

CME	Fast	Moderate	Slow
CME duration, h	1.3	3.0	6.4
Total mass loss, 10^{15} g	1.5	1.0	1.2
Mean mass-loss rate, 10^9 g s^{-1}	226	71	39

calculated as the total flux through the computational domain boundaries, so the plot has some delay. The plot can be used to estimate the relaxation time to the stationary rate of mass loss after the planet's passing through a fast, moderate, and long CME as ~ 0.6, ~ 1.2, and ~ 2 h, respectively.

In the stationary regime, the mass-loss rate for the studied flow is $\sim 3 \times 10^9$ g s^{-1} [99]. The flow passing through the CME leads to the entire extended envelope's withdrawal and temporarily increases the mass-loss rate. Table 3 lists the total mass loss and the mean mass-loss rate during the CME passage. The table shows that the total mass loss rate remains about the same in all three cases. This is entirely expected, because the CME duration is inversely proportional to its speed. Assuming a mean CME rate for a solar-type star of ~ 23 per month [203], for a hot Jupiter with a quasi-stationary envelope, the CME-induced mass loss can be estimated as $\sim 2 \times 10^{25}$ g over one billion years for the planet's mass of $\sim 10^{30}$ g. Here, solely due to the interaction with the undisturbed stellar wind, the planet will lose $\sim 9 \times 10^{25}$ g at a mean mass-loss rate of $\sim 3 \times 10^9$ g s^{-1} [99].

As shown in papers [189, 190], a head-on collision with CME fully withdraws the extended envelope. To investigate the effect of a less powerful CME, papers [194, 204] performed numerical simulations of a tangential collision of a planet with a narrow and weak CME. Those papers used a simplified configuration of the typical solar CME consisting of three phases; the duration of the phases was assumed to be the same and equal to one-third of the CME duration. Physical parameters such as density, pressure, and radial velocity remained constant inside each separate phase. Two CME types were considered: long (3 h) and short (0.5 h). In

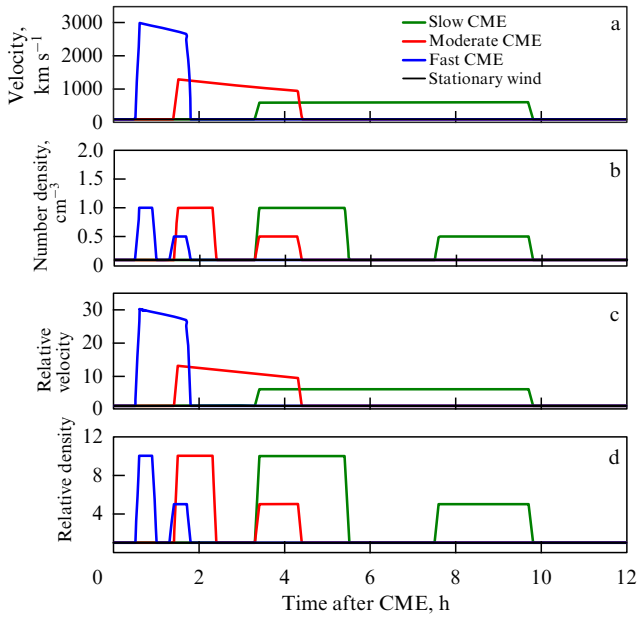

Figure 50. (Color online.) Time profiles of stellar wind velocity and density during passage of a slow (green), moderate (red), and fast (blue) CME (time in hours). Horizontal black line indicates the stationary stellar wind. Figures c and d display the relative velocity and density of the stellar wind.

both cases, the wind velocity in the entire CME was set to be constant: 1.3×10^3 km s^{-1} and 6×10^2 km s^{-1} for the long and short CME, respectively, for an undisturbed wind velocity of 100 km s^{-1}. The stellar wind density was 1.66×10^{-19}, 1.66×10^{-20}, and 8.3×10^{-20} g cm^{-3} at the first, second, and third phases, with an undisturbed wind density of 1.66×10^{-20} g cm^{-3}. The duration of all three phases was the same and equal to 1 h and 0.17 h for the long and short CME, respectively. The CME matter was assumed to move within a 30° cone before entering the computational domain.

Figure 53 shows the logarithmic density distribution in the equatorial plane of the system and the density isosurface $\rho = 2.5 \times 10^{-18}$ g cm^{-3} for the 'long' CME model. The planet is at the computational domain center in these plots, and the star lies to the left outside the figure limits (in the negative X region). The velocities are given in the planet's frame. All sizes are normalized to the planet's radius.

At $t = 0$, the CME (Fig. 53a) first touches the extended envelope. The CME is so short that all its three phases are within the computational domain by this time. At $t = 120$ min (Fig. 53b), the CME has already left the computational domain by breaking the shock system before the atmosphere and the envelope but has not disturbed the envelope itself. Nevertheless, a rarefication wave behind the CME decreased the pressure near the planet, which has destabilized the envelope, and, by the time $t = 261$ min (Fig. 53c), almost

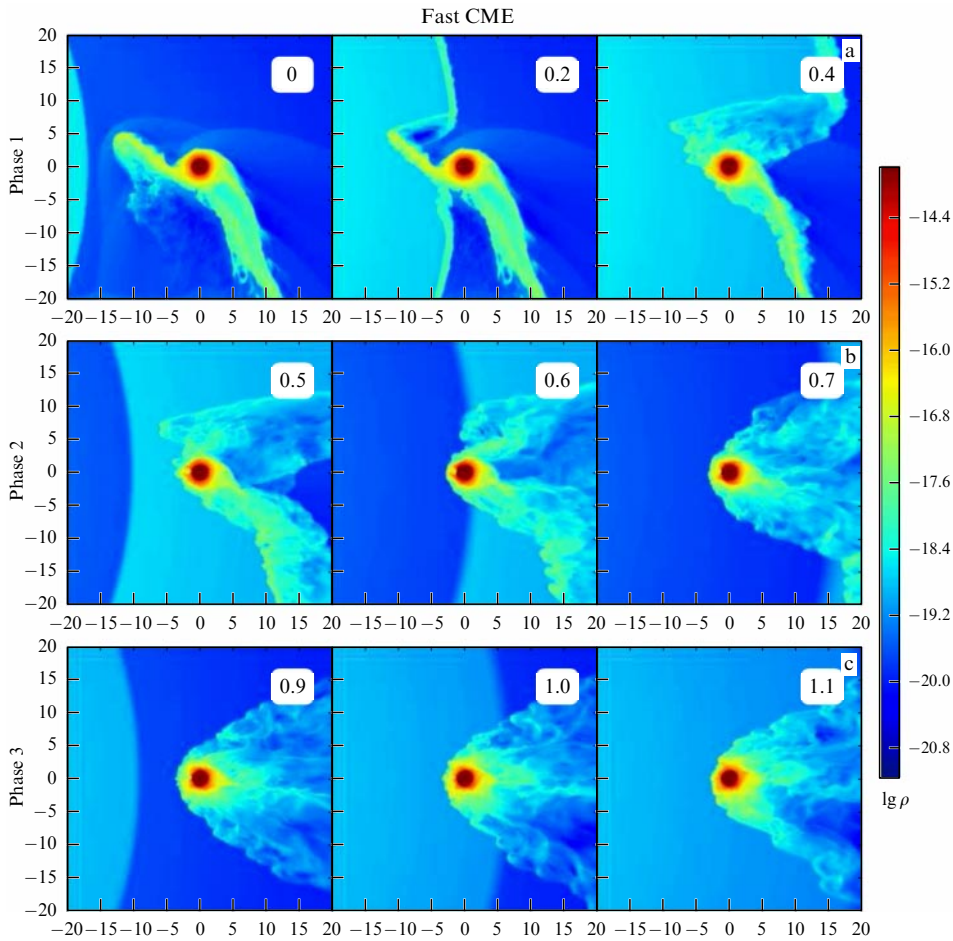

Figure 51. (Color online.) Density distribution in the orbital plane of a planet with a quasi-closed envelope during interaction with fast CME. The time in hours is shown in the upper right corner. Star is to the left outside computational domain boundary. All sizes are in units of $R_{\rm pl}$.

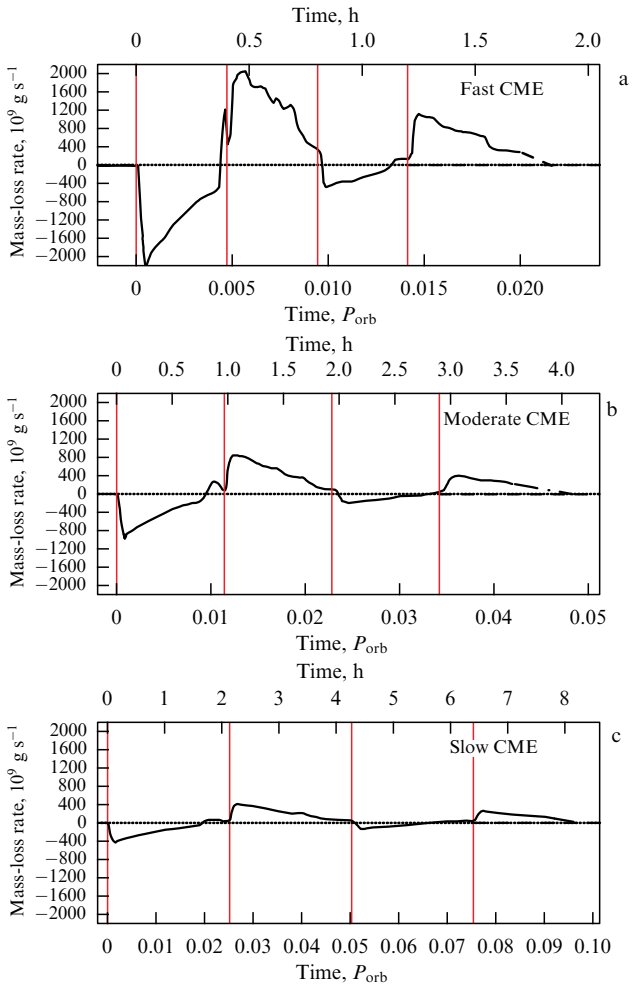

Figure 52. (Color online.) Mass-loss rate as a function of time when crossing a fast (a), moderate (b), and slow (c) CME. The vertical red lines indicate the limits of the three CME phases. At the end of calculations, the dashed-dotted line shows the extrapolation of the mass-loss rate to the level obtained for the stationary wind (dotted line), 3×10^9 g s^{-1}.

the entire stream from the inner Lagrangian point L_1 has dispersed, and the envelope around the planet has started dispersing (see paper [194] for more detail). By the end of computations ($t = 642$ min, Fig. 53d), the envelope continues dispersing. The full animation for the 'long' CME model can be found at https://bit.ly/2RvWP3x.

Figure 54, like Fig. 53, presents the solution for a shorter CME, also interacting tangentially but delayed relative to the planet's motion. At $t = 10$ min, the CME (Fig. 54a) first touches the extended envelope. Next, Fig. 54b shows the moment $t = 116$ min when the CME has passed through an almost entire computational domain. As in the first calculation, by this time, the envelope still preserves its form, but the violation of the pressure equilibrium destroys it by the time $t = 261$ min (Fig. 54c). The second calculation was completed much later, allowing us to observe the envelope recovering ($t = 1040$ min, Fig. 54d). The full animation for the 'short CME' model can be found at https://bit.ly/31JpEyd.

An interesting feature of the flow in the hot Jupiter envelope colliding with the CME is the mass loss in both the equatorial plane and the perpendicular direction. The diameter of the gas envelope immediately around the planet increases significantly and even exceeds the computational domain, i.e., larger than $10R_{pl}$, which is clearly seen in Figs 53 and 54 by comparing the flow at the beginning and at the end of the CME passage. This means that the moment of passing through the CME should be clearly observable in hot Jupiter transits.

The results of the modeling imply that even a tangential interaction with CME destroys the extended envelope. What is most destructive is the rarefication zone following the CME — a local decrease in the dynamical pressure leads to envelope expansion and its density decrease, which breaks the stationary flow, and almost all the envelope mass is shed. The planet's calculated lost mass was $\sim 10^{15}$ g for both cases. The approximately equal mass loss is because the interaction with the CME results in the entire envelope being shed. A similar picture was observed in the model considered in papers [189, 190]. Thus, even weak and narrow CMEs are dangerous for the extended envelope, which should be taken into account in estimates of the atmospheric mass loss from hot Jupiters.

5.3 Dependence of the exoplanetary atmospheric mass loss on the coronal mass ejection rate

The formation time of a quasi-closed planetary envelope t_{form} is another important parameter determining the total atmospheric mass-loss rate caused by CME [205]. According to the gas-dynamical calculations [29], for HD 209458b, this time is $t_{form} \approx 24$ h, which is about two times as long as the stream formation time in the ballistic approximation. Calculations in [29] suggest that the envelope extension L (distance from the L_1 point to the head-on collision point) is $\sim 7R_{pl}$. However, the analysis of the HST observations of the exoplanet WASP-12b [206] carried out in paper [121] suggested that the envelope size can be much larger, $L > 21R_{pl}$. Clearly, for larger envelopes, M_{env}, t_{loss}, and t_{form} are different. According to our estimates, the maximum possible size of the envelope of HD 209458b should be $\sim 52R_{pl}$, its mass is $\sim 10^{-15}M_{jup}$, and t_{loss} and t_{form} are ~ 15 and ~ 39 h, respectively.

The combination of these three parameters, M_{env}, t_{loss}, and t_{form}, allows, in principle, determining the dependence of the exoplanetary atmospheric mass loss on the CME occurrence rate. However, the CME duration t_{CME} compared with the envelope loss time t_{loss} should also be taken into account. Indeed, if the CME duration exceeds t_{loss}, the efficiency decreases, because the entire envelope will be removed over time t_{loss}, and no mass loss occurs in the time interval $t_{CME} - t_{loss}$. If t_{CME} is less than t_{loss}, the efficiency also decreases, because only the fraction $M_{env}\, t_{CME}/t_{loss}$ of the envelope will be carried away during the CME. Clearly, what is optimal is a CME with $t_{CME} = t_{loss}$, and we will consider only such flares below.

The flare rate significantly changes over the star lifetime. Data, including those obtained by the Kepler space telescope [207], enable determining the empirical dependence between the star age and the rate of superflares with energy exceeding the mean energy of the solar flares by three orders of magnitude: $f \sim t^{-1.4}$. Here, according to [185], the relation between the frequency and power of flares in solar-type stars has the universal form $\mathrm{d}N/\mathrm{d}E \sim E^{-2}$. This allows us to suppose that the rate of flares of any type changes with stellar age following the same law as superflares.

Consider the effect of the CME occurrence rate on the mass-loss rate. As shown above, the optimal efficiency is attained for the ejection duration $t_{CME} = t_{loss}$. In addition, the flares will carry away a maximal amount of matter if the envelope has time to form, i.e., the time between CMEs should be t_{form}. This means that the most effective mass

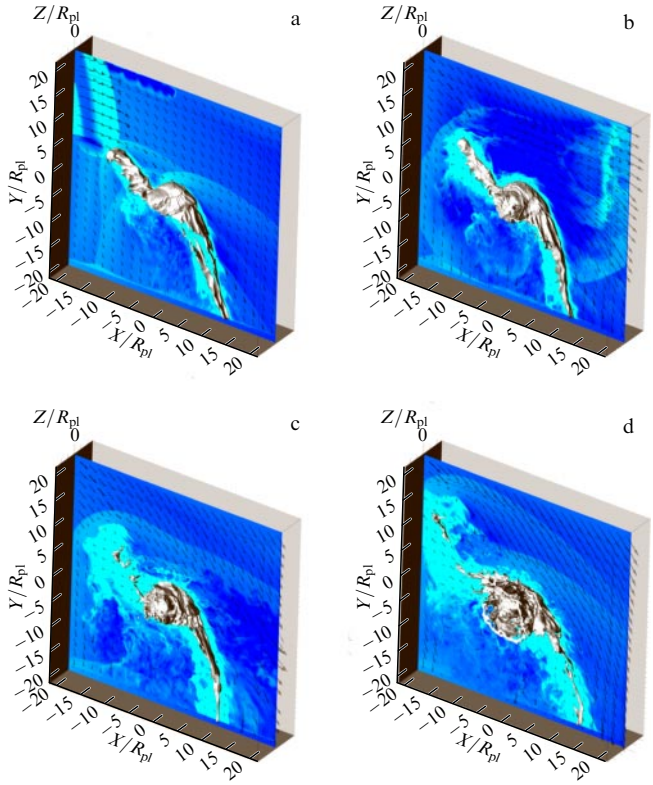

Figure 53. (Color online.) Solution for time (a) $t = 0$, (b) $t = 120$, (c) $t = 261$, and (d) $t = 642$ min for a 'long' CME.

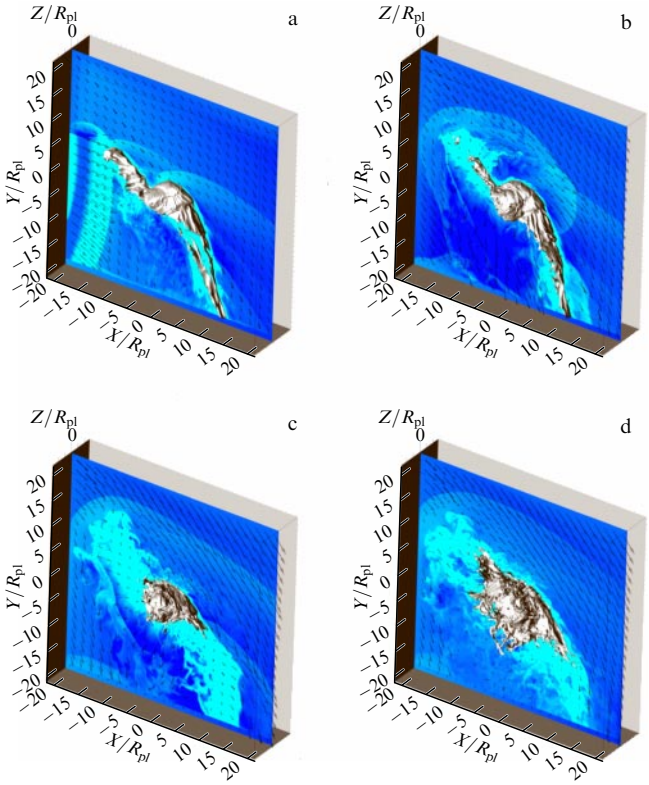

Figure 54. (Color online.) Solution for time (a) $t = 10$, (b) $t = 116$, (c) $t = 266$, and (d) $t = 1040$ min for a 'short' CME.

outflow per unit time is attained for the characteristic time between the flares equal to $t_{\rm loss} + t_{\rm form}$, and the total mass-loss rate $\dot{M} = M_{\rm env}/(t_{\rm loss} + t_{\rm form})$. For a quasi-closed envelope with a size of $L \sim 7R_{\rm pl}$, the optimal flare periodicity is 31.4 h, and the total mass-loss rate is $\sim 10^{10}$ g s^{-1} or $\approx 1.64 \times 10^{-13}$ of Jupiter's mass per year. For an envelope with maximal size ($L \sim 52R_{\rm pl}$), the optimal mass-loss rate will be about the same for the characteristic time of 54 h between the flares.

The above estimates of the mass-loss rate are maximal for flares powerful enough to shed the external envelope but insufficient to withdraw the matter inside the Roche lobe. Note that these estimates are in agreement with the mass-loss rate due to free outflow from the inner Lagrangian point $\dot{M}_{\rm L_1} = 2 \times 10^{10}$ g s^{-1}. This enables using the theoretically determined value $\dot{M}_{\rm L_1}$ in the general analysis of the mass loss from exoplanets.

With an increasing or decreasing flare rate (with constant flare duration), the losses will decrease, because either the flares will overlap to block the matter outflow from the Roche lobe or the envelope will be in a quasi-steady state between the flares, when the mass-loss rate is low. Beyond some threshold, the increase in the flare power will lead to shedding both the external envelope and matter inside the Roche lobe, which strongly enhances $\dot{M}$. This mechanism requires further investigation, because the direct effect of powerful CMEs on a dense atmosphere can significantly (by orders of magnitude) increase the mass-loss rate from hot Jupiters.

From knowledge of the flare rate dependence on the stellar age [207] and using the observed solar flare rate, it is possible to estimate the age at which a hot Jupiter with the parameters of HD 209458b will have a maximal mass-loss rate. The most favorable flaring rate happens at the age of 0.8 billion years. This estimate is based on the assumption that the envelope size is $\sim 10R_{\rm pl}$; however, its maximal extension, in the case of a low stellar wind velocity, for HD 209458b is $\sim 52R_{\rm pl}$. The same mass-loss rate is reached for a flare periodicity of once every 54 h, corresponding to the stellar age of 1.2 billion years.

5.4 Effect of a magnetic field on envelope interaction with coronal mass ejections

The analysis in Section 4 (see also [140]) showed that the stellar wind magnetic field is an important factor determining the flow structure in the envelope of a hot Jupiter, because many hot Jupiters are inside the sub-Alfvénic stellar wind zone where the magnetic pressure exceeds the dynamic pressure. As the Alfvén velocity does not exceed the fast magnetosonic speed, for hot Jupiters from the sub-Alfvénic zone, the wind velocity is lower than the fast magnetosonic speed. This case corresponds to a subsonic streamline of the body when no bow shock arises in pure gas dynamics. A similar situation occurs in magnetohydrodynamics. This means that the stellar wind flow around a hot Jupiter from the sub-Alfvénic zone should be shockless [143].

Paper [150] considered possible effects related to the change in the streamlining of a hot Jupiter's atmosphere when passing through a CME. The CME parameters used in that paper are presented in Table 4. These parameters are detected near Earth's orbit, where the shock, determining the beginning of the first phase, is purely gas dynamical. This is because the solar wind magnetic field in this region is weak. However, in the sub-Alfvénic zone of the solar wind, the shock at the CME front is a fast MHD shock wave. Therefore, its parameters (particularly its front propagation speed) can be significantly different from those of a purely gas-dynamical shock.

Table 4. Stellar wind parameters (density, temperature, magnetic field, and Alfvén Mach number) during CME passage.

Phase	1	2	3	4
Duration, h	—	8.5	13	22
n/n_w	1	4	0.6	10
T/T_w	1	5.07	0.79	0.30
v/v_w	1	1.33	1.44	1.11
B/B_w	1	2.25	1.75	1.13
λ/λ_w	1	1.18	0.63	3.11

In Section 4, we have shown that the interaction of the stellar wind with the planetary ionospheric envelope in the case of a strong magnetic field is shockless. The bow shock does not arise around either the planetary atmosphere or the matter ejected from the L_1 point. The stellar wind magnetic field is so strong that it blocks the free motion of plasma perpendicular to the magnetic field lines. Therefore, the ejected matter moves towards the star predominantly along the wind magnetic field lines. Thus, in this case, the electromagnetic force caused by the stellar wind magnetic field is comparable to the stellar gravity force, the centrifugal force, and the Coriolis force.

Oppositely, in the case of a weak magnetic field, the interaction of the stellar wind with the planetary ionospheric envelope gives rise to a bow shock. The shock consists of several intersecting shocks, one of which arises due to the wind interaction with the gas stream from the inner Lagrangian point L_1, and others due to the immediate interaction with the planetary atmosphere and the tail of matter behind it. The magnetic field preserves its dipole structure inside the Roche lobe. As the stellar wind magnetic field, in this case, is weak and does not play any significant dynamical role, the flow structure in the envelope is close to a purely gas dynamic case.

Thus, the calculations discussed in Section 4 allow us to conclude that a decrease in the stellar wind magnetic field leads to bow shock formation. As hot Jupiters lie close to the Alfvén point in the stellar wind, this, in particular, suggests that even relatively small fluctuations in the streamlining flow can lead to the disappearance or, oppositely, to the appearance of shocks around the planet.

Consider now MHD features of the interaction of a CME with an ionosphere of a hot Jupiter. The last line in Table 4 shows the change in the Alfvén Mach number

$$\frac{\lambda}{\lambda_w} = \sqrt{\frac{n}{n_w}}\,\frac{v}{v_w}\,\frac{B_w}{B} \tag{83}$$

at different phases of the CME passage. As seen from Table 4, the value of λ changes nonmonotonically. In the first phase, λ slightly exceeds the unperturbed value λ_w; in the second phase, λ becomes smaller than the unperturbed value λ_w; and in the third phase, λ sharply increases again to exceed the unperturbed value λ_w by a factor of three.

If the planet sits deep inside the sub-Alfvénic zone or, oppositely, far in the super-Alfvénic zone, the character of streamlining during the CME passage does not change. For a strong wind magnetic field, the streamlining will be shockless, and when the wind magnetic field is weak, the whole process from the beginning to the end will be accompanied by the formation of bow shocks. However, if the planetary orbit lies close to the Alfvén point, the CME interaction with the magnetosphere can be more complicated and intriguing. Let us recall that this case should be widespread among hot Jupiters [140].

Suppose that such a planet is close to the Alfvén point but from the sub-Alfvénic side. Then, in the second phase, the flow regime should remain shockless, because, in this phase, the Alfvén Mach number is smaller than the unperturbed value λ_w. In the first and third phases, the Alfvén Mach number, in contrast, increases relative to the unperturbed value. Depending on the specific situation, this could be quite sufficient for the flow velocity to exceed the fast magnetosonic speed in the third CME phase or immediately in the first and third phases. In the first case, in the third CME phase, a bow shock emerges that disappears by the end of the process when the system relaxes to the initial unperturbed state. In the second case, the shock arises already in the first phase, disappears in the second phase, then appears again in the third phase, ultimately disappearing after CME passage.

Suppose now that a hot Jupiter is close to the Alfvén point but from the super-Alfvénic side. Then, the flow regime can change in the second phase of CME passage when the Alfvén Mach number drops below the unperturbed value. This can be quite enough to make the flow shockless when the streamlining velocity gets smaller than the fast magnetosonic speed, and the bow shock does not form. Due to the flow regime change, the bow shock can 'switch off' for some time, to appear again after termination of the second phase of the ejection.

The arising or disappearance of the shock can also lead to observable effects. X-ray emission may be one of the shock appearances. As seen from Fig. 55, the temperature in shocks before the planetary envelope can be quite high (up to 1.5×10^6 K), with the mean thermal gas velocity (the sound speed) being ~ 144 km s^{-1}. The particle collision velocity at the shock front also depends on the velocity jump at the front, which is ~ 160 km s^{-1} in the solution obtained. This gives the mean particle collision velocity of ~ 300 km s^{-1} at the shock front passage. The collision of protons with such velocities should give rise to hard X-ray emission with an energy of ~ 1 keV related to the shock.

Considering the relatively high luminosity of the bow shock, its appearance/disappearance can be discovered by X-ray observations of exoplanets during CME passages. Such observations are presented in [208]. Observations of an outburst in the CVSO 30 system hosting a hot Jupiter with a mass of $\sim 3.6 M_{jup}$ and an orbital period of ~ 0.44 days were performed in the soft (0.1–1 keV) and hard (1–9 keV) X-ray bands. In the hard X-rays, a short-term luminosity decrease was detected ~ 2.7 h after the flare beginning. Unfortunately, the characteristics of the wind and the magnetic field of the star CVSO 30 are unknown. However, it is possible to assume that the observed X-ray dip could be related to the transition of the flow around the hot Jupiter from the super-Alfvénic to the sub-Alfvénic regime associated with the bow shock disappearance. If this is the case, we can use these data to probe the stellar wind. Indeed, dividing the planet-star separation by the time before the dip appearance on the light curve yields a mean velocity of ~ 60 km s^{-1}, in agreement with the wind velocity at such a distance for a solar-type star. Paper [208] points out that AAVSO (American Association of Variable Star Observers) data demonstrated an optical eclipse of this star at this time.

Another possible observational appearance of the flow transition from the shock to the shockless regime and back may be related to a change in the charge exchange rate

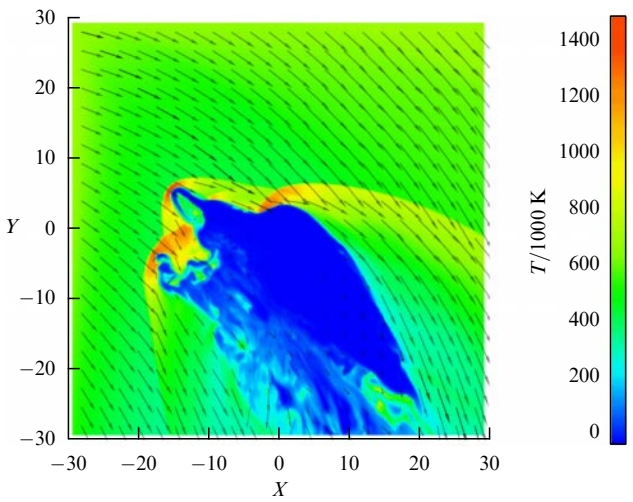

Figure 55. (Color online.) Temperature and density distribution in the orbital plane of a hot Jupiter for the super-Alfvénic flow regime. Solution is presented for the time $0.27P_{\rm orb}$ from the beginning. Distances are normalized to planetary radius $R_{\rm pl}$.

between the stellar wind plasma and the gaseous atmosphere of a hot Jupiter. The recharging process produces high-energy particles in the gas and the corresponding broadening of the absorption lines in the atmosphere of a hot Jupiter [68]. The shock disappearance should decrease the density of the stellar wind directly interacting with the hot Jupiter's atmosphere and correspondingly diminish the charge exchange rate. Thus, the change in the absorption lines during CME passage can provide additional information on the properties of the hot Jupiter's atmosphere and the stellar wind parameters.

Coronal mass ejections occur pretty frequently, especially in young stars, and significantly affect the long-term evolution of hot Jupiters. As shown above, the passage through a CME can lead to a short X-ray intensity drop or jump related to the flow regime change near the hot Jupiter. This effect can be potentially observed not only for transiting hot Jupiters, thus offering a unique opportunity of discovering exoplanets that cannot be detected by other means. In addition, analysis of the X-ray flux variability enables estimating the stellar wind parameters of distant stars, which is also challenging to do by other means.

6. Conclusions

The results presented above demonstrate that atmospheres and extended envelopes of hot Jupiters have been studied over recent years by scientists from many (most) countries. Together with active multiwavelength ground-based and space observations, considerable effort has been undertaken to develop numerical models of these objects. It is gratifying to note that work by Russian scientists based on kinetic, gas-dynamic, and MHD calculations has contributed significantly to the studies of HJs and is recognized worldwide.

These investigations have already enabled solving some fundamental issues about the physics, structure, and dynamics of HJ envelopes. Therefore, we can summarize the key results presented in the present paper as follows.

• Hot Jupiters possess giant quasi-stationary envelopes of irregular form. Such envelopes are justified by the theoretical estimates and numerical simulations presented in this paper and confirmed by existing observational data. Properties of the envelopes are determined by matter outflow from HJ atmospheres because of heating by and gravitational interaction with the nearby star and by interaction with the stellar wind, which stabilizes the outflow and bounds the envelope size. It is important to note that HJs differ from gas giants in high orbits, first and foremost, by the presence of extended gaseous and/or plasma envelopes.

• Theoretical estimates supported by the results of three-dimensional numerical modeling suggest that three main types of envelopes can form around hot Jupiters, depending on the parameters. The first type includes *closed envelopes* when the planetary atmosphere is inside its Roche lobe. The second type comprises *open envelopes* produced by outflows from the nearby Lagrangian points. Finally, it is possible to distinguish *quasi-closed envelopes* of the intermediate class when the dynamical pressure of the stellar wind blocks the outflow outside the Roche lobe. Calculations show that, in closed or quasi-closed envelopes, the mass-loss rate from hot Jupiters turns out to be significantly lower than from open envelopes.

• HJ envelopes are important because nonspherical and sufficiently dense envelopes should affect the observed radiation flux. No less important is the fact that the presence of an envelope significantly determines the physics of the interaction of stellar radiation and wind with the exoplanet. In particular, extended envelopes cause the formation of a large transitional region and thus increase the role of kinetic processes in the physics of the HJ atmosphere. The results presented above demonstrate that taking into account suprathermal photoelectrons in the aeronomic model decreases by several times the atmospheric gas outflow rate. Such a decrease can be responsible for incomplete loss of the primary hydrogen-dominated atmosphere of exoplanets. In addition, kinetic calculations correctly taking into account the heat losses by suprathermal photoelectrons suggest that the heating efficiency by stellar radiation does not exceed 0.2 in the thermosphere of hydrogen-dominated HJs. Calculations of the heating efficiency of the upper atmosphere of HJs by precipitating electrons show them to be more efficient in HJs than in the planet Jupiter, reaching 17%.

• The results of 3D calculations and their comparison with observations have revealed very complex dynamics of envelopes. The close proximity of most HJs to the host stars and their Roche lobe overflow leads to outflows through the libration points L_1 and L_2. Moreover, interaction with the stellar wind, as a rule, occurs supersonically, leading to the formation of a bow shock and the appearance of many features in the flow structure. It is important to note that calculations revealed a weak effect of the stellar radiation on the envelope dynamics, because the matter is ionized and poorly interacts with photons. At the same time, MHD modeling results presented in the paper confirm the significant influence of the proper magnetic field of HJs and the stellar wind magnetic field on the obtained solutions. For example, in the case of a strong magnetic field in the wind, a new type of envelope can appear when the outflowing matter moves towards the star along the wind magnetic lines.

• The envelopes around HJs can significantly change the evolutionary status of these exoplanets. The results of calculations presented in this paper suggest a strong effect from stellar activity (flares and coronal mass ejections) on the mass loss from HJs. Indeed, the HJ envelopes have large sizes and are bound weakly gravitationally to the planet. There-

fore, even a tangential interaction with a coronal mass ejection fully destroys the envelope and leads to the loss of the entire envelope mass. For HJs near young and active stars, such losses can be comparable to the stationary mass loss due to Roche lobe overflow.

Despite the progress in understanding the physics and kinetics of HJ envelopes, this problem still has a significant potential for development, both in observational and theoretical aspects.

Exoplanet studies are undoubtedly one of the most relevant topics of modern astrophysics and general science. For humankind, the possible existence of extraterrestrial life beyond the Solar System is the most interesting issue. Bearing this in mind, some sceptics believe that HJ studies are being carried out using the 'under light' principle, because the features of these exoplanets preclude the existence of any forms of life there, but most observational data have been acquired exactly for them. The presented results disprove this statement and suggest that knowledge about HJ envelopes can provide crucial information on the possibilities of the appearance of life on other planets of systems with HJs. Let us enumerate several points.

(1) Huge mass loss from HJ envelopes should affect the chemical composition of the interplanetary medium, thus determining the properties of the secondary atmospheres of Earth-like planets.

(2) The giant planets, including HJs, mainly determine the architecture of a planetary system. HJ migration, for various reasons, including atmospheric outflows [209], affects the structure of the potentially habitable zone in the planetary system.

(3) The motion of HJs towards the star can lead to its being engulfed and the appearance of a giant flare. Indeed, by assuming that half of the orbital kinetic energy of an HJ ($\sim 10^{45}$ erg) will be converted into radiation and emitted over one orbital revolution (during several days), the luminosity of such a flare will be five orders of magnitude higher than the solar one. Undoubtedly, the possibility of such a catastrophic event and its effect on the atmospheres of Earth-like planets should be carefully investigated.

(4) The devastating effect of stellar flares and CMEs on the appearance and sustaining of life on Earth-like planets is well recognized. However, if flares can be detected from Earth (as was the case with the Kepler space telescope, which discovered giant flares in solar-like stars), information on the emergence and propagation of CMEs may be obtained by inspecting the response of the HJ envelopes. Moreover, studies of HJ envelopes around solar-type stars provide information on stellar winds from such stars at different evolutionary stages, enabling investigating (predicting) future stellar activity, including that of our Sun.

In addition, we note that the methods and models elaborated for HJ studies can be applied to investigate other exoplanets (including Earth-like ones) and will be in demand so far as growing observational material after the launch of new prospective space missions.

Presently, there are many observational projects aimed at detecting and investigating exoplanets. Of special interest are space projects that will be able to obtain high-resolution spectra and light curves for transiting planets: HST (Hubble Space Telescope), TESS (NASA's Transiting Exoplanet Survey Satellite), CHEOPS (ESA's CHaracterizing ExOPlanet Satellite), and Gaia. The HST mission is coming to an end (it is assumed that it will cease operating in 2021), but, so far, it has been obtaining important data on exoplanets, including light curves and spectra in the near UV range during transits. Unfortunately, the orbit of this telescope precludes obtaining long time series of observations. The TESS mission launched in 2018 can perform long uninterrupted and high-precision observations of light curves due to its elongated orbit outside the Van Allen belts. The CHEOPS mission launched at the end of 2019 will be able to measure with high accuracy the light curves of stars with transiting exoplanets. This will offer the opportunity to determine the radii of transiting exoplanets with an accuracy of better than 10%. There are high expectations for the Gaia mission, which can discover exoplanets from spectral and photometrical data. The launch of several other space telescopes is envisaged soon, fully or partially aimed at studying exoplanets. First and foremost, we should mention here the launch of the 6.5-m James Webb Space Telescope (JWST) planned in 2021. The infrared camera of the JWST will enable observing transits of HJs and other exoplanets with a high signal-to-noise ratio and obtaining high-resolution spectra of transiting exoplanets. The PLATO (ESA's PLAnetary Transits and Oscillations of stars mission) space telescope, planned for launch in 2026, will fly near the Earth–Sun Lagrangian point L_2 and be equipped with 26 cameras for photometric observations of transiting exoplanets in a wide field of view. It is assumed that this instrument will be able to measure the size of transiting exoplanets with an accuracy of up to 3%. Approximately at the same time, the WFIRST (Wide-Field InfraRed Survey Telescope) is planned for launch. It is a wide-field infrared telescope with a 2.4-m mirror to observe about 200 stars close to the Sun. This instrument will be able to take images with a contrast of 10^{-9} using a coronograph and carry out spectroscopic observations. Finally, we should note the Russian Spectrum-UF (WSO-UV) space telescope to be launched in 2025. Spectrum-UF is a unique 1.7-m UV telescope with a sensitivity matching the HST. In the next 10–15 years, it will be unrivalled for UV observations. The mission features enable carrying out for the first time unique observations of exoplanets and their atmospheres. In particular, it will be possible for the first time to successfully search for biomarkers, because many potentially important lines lie in the UV range [210].

Forthcoming observations promise to provide a great deal of new information on different exoplanets; clearly, most of the data will be obtained for hot Jupiters. The interpretation of the new data will require more developed models. Note that this is a rare case in science evidencing a true symbiosis of theoretical and experimental studies, providing conditions for the correct interpretation of observations, and allowing the formulation of new observational tasks. As for the development of theoretical investigations, some ways to elaborate on numerical models are straightforward, and only additional resources (of a different kind) are required for their realization. The necessary steps include, for example, accurately taking into account the atmospheric chemistry; an increase in the spatial resolution, enabling us to take into account the effect of atmospheric processes on the envelopes and to investigate envelope expansion into the interplanetary medium; and taking into account magnetic viscosity. Some developments, for example, the creation of hybrid models, are not so obvious and require careful consideration of all physical processes involved in HJ envelopes. Nevertheless, to conclude, we can ascertain that, in the forthcoming years, studies of the atmospheres and envelopes of hot Jupiters

will remain topical and important and, moreover, will gain additional impetus.

Acknowledgements. The authors acknowledge the Government of the Russian Federation and the Ministry of Higher Education and Science of RF for their aid via grant no. 075-15-2020-780 (no. 13.1902.21.0039) for the support of studies of atmospheric losses. The results of this analysis are presented in Sections 2, 3, and 5. The results of Section 4 are obtained under the financial support of the Russian Science Foundation (project RSF 18-12-00447). Development of kinetic Monte Carlo models of the atmospheric precipitation of high-energy particles used in Section 2 is supported by RSF grant 19-12-00370. The work was carried out using equipment from the center of collective use, Complex of Modeling and Data Processing of Mega-Class Research Facilities of the National Research Center Kurchatov Institute (http://ckp.nrcki.ru/), and also facilities of the computational cluster of the Inter-agency Supercomputer Center of RAS.

References

1. Mayor M, Queloz D *Nature* **378** 355 (1995)
2. Safronov V S *Evolution of the Protoplanetary Cloud and Formation of the Earth and the Planets* (Jerusalem: Israel Program for Scientific Translations, 1972); Translated from Russian: *Evolyutsiya Doplanetnogo Oblaka i Obrazovanie Zemli i Planet* (Moscow: Nauka, 1969)
3. Pollack J B et al. *Icarus* **124** 62 (1996)
4. Marov M Ya *Phys. Usp.* **48** 638 (2005); *Usp. Fiz. Nauk* **175** 668 (2005)
5. Marov M "The formation and evolution of the solar system", in *Oxford Research Encyclopedia of Planetary Science* (Eds P Read et al.) (Oxford: Oxford Univ. Press, 2018) id. 2
6. Dawson R I, Johnson J A *Annu. Rev. Astron. Astrophys.* **56** 175 (2018)
7. Paardekooper S-J, Johansen A *Space Sci. Rev.* **214** 38 (2018)
8. Morbidelli A, in *Handbook of Exoplanets* (Eds H J Deeg, J A Belmonte) (Cham: Springer, 2018) p. 2523
9. Batygin K, Bodenheimer P H, Laughlin G P *Astrophys. J.* **829** 114 (2016)
10. Guo X et al. *Astrophys. J.* **838** 25 (2017)
11. Vidal-Madjar A et al. *Nature* **422** 143 (2003)
12. Ben-Jaffel L *Astrophys. J.* **671** L61 (2007)
13. Vidal-Madjar A et al. *Astrophys. J.* **604** L69 (2004)
14. Ben-Jaffel L, Sona Hosseini S *Astrophys. J.* **709** 1284 (2010)
15. Linsky J L et al. *Astrophys. J.* **717** 1291 (2010)
16. Fossati L et al. *Astrophys. J.* **714** L222 (2010)
17. Lecavelier des Etangs A et al. *Astron. Astrophys.* **543** L4 (2012)
18. Lammer H et al. *Astrophys. J.* **598** L121 (2003)
19. Yelle R V *Icarus* **170** 167 (2004)
20. García Muñoz A *Planet. Space Sci.* **55** 1426 (2007)
21. Murray-Clay R A, Chiang E I, Murray N *Astrophys. J.* **693** 23 (2009)
22. Koskinen T T et al. *Icarus* **226** 1678 (2013)
23. Shaikhislamov I F et al. *Astrophys. J.* **795** 132 (2014)
24. Khodachenko M L et al. *Astrophys. J.* **813** 50 (2015)
25. Shaikhislamov I F et al. *Astrophys. J.* **832** 173 (2016)
26. Shematovich V I, Ionov D E, Lammer H *Astron. Astrophys.* **571** A94 (2014)
27. Shematovich V I, Bisikalo D V, Ionov D E *Characterizing Stellar and Exoplanetary Environments* (Astrophysics and Space Science Library, Vol. 411, Eds H Lammer, M Khodachenko) (Cham: Springer, 2015) p. 105
28. Bisikalo D et al. *Astrophys. J.* **764** 19 (2013)
29. Bisikalo D V et al. *Astron. Rep.* **57** 715 (2013); *Astron. Zh.* **90** 779 (2013)
30. Haswell C A et al. *Astrophys. J.* **760** 79 (2012)
31. Nichols J D et al. *Astrophys. J.* **803** 9 (2015)
32. Grodent D, Waite J H (Jr.), Gérard J-C *J. Geophys. Res.* **106** 12933 (2001)
33. Marov M Ya, Shematovich V I, Bisikalo D V *Space Sci. Rev.* **76** 1 (1996)
34. Seager S, Deming D *Annu. Rev. Astron. Astrophys.* **48** 631 (2010)
35. Madhusudhan N *Annu. Rev. Astron. Astrophys.* **57** 617 (2019)
36. Massol H et al. *Space Sci. Rev.* **205** 153 (2016)
37. Shematovich V I, Marov M Ya *Phys. Usp.* **61** 217 (2018); *Usp. Fiz. Nauk* **188** 233 (2018)
38. Owen J E *Annu. Rev. Earth Planet. Sci.* **47** 67 (2019)
39. Johnson R E et al. *Space Sci. Rev.* **139** 355 (2008)
40. Lammer H *Origin and Evolution of Planetary Atmospheres: Implications for Habitability* (Heidelberg: Springer, 2013)
41. Holmström M et al. *Nature* **451** 970 (2008)
42. Shematovich V I *Russ. Chem. Rev.* **88** 1013 (2019); *Usp. Khim.* **88** 1013 (2019)
43. Tian F et al. *Science* **308** 1014 (2005)
44. Erkaev N V et al. *Astrobiology* **13** 1011 (2013)
45. Luger R, Barnes R *Astrobiology* **15** 119 (2015)
46. Bisikalo D V, Shematovich V I, in *Origins: from the Protosun to the First Steps of Life: Proc. of the 345th Symp. of the Intern. Astronomical Union, Vienna, Austria, 20–23 August, 2018* (Proc. IAU Symp. 345) (Eds B G Elmegreen, L V Tóth, M Güdel) (Cambridge: Cambridge Univ. Press, 2019) p. 168
47. Shematovich V I *Solar Syst. Res.* **44** 96 (2010); *Astron. Vestn.* **44** 108 (2010)
48. Ionov D E et al. *Solar Syst. Res.* **48** 105 (2014); *Astron. Vestn.* **48** 113 (2014)
49. Shematovich V I et al. *J. Geophys. Res. Planets* **113** E02011 (2008)
50. Garvey R H, Green A E S *Phys. Rev. A* **14** 946 (1976)
51. Jackman C H, Garvey R H, Green A E S *J. Geophys. Res.* **82** 5081 (1977)
52. Garvey R H, Porter H S, Green A E S *J. Appl. Phys.* **48** 190 (1977)
53. Shyn T W, Sharp W E *Phys. Rev. A* **24** 1734 (1981)
54. Dalgarno A, Yan M, Liu W *Astrophys. J. Suppl.* **125** 237 (1999)
55. Kawahara H et al. *Astrophys. J.* **776** L6 (2013)
56. Watson A J, Donahue T M, Walker J C G *Icarus* **48** 150 (1981)
57. Chassefière E *J. Geophys. Res.* **101** 26039 (1996)
58. Koskinen T T et al. *Icarus* **226** 1695 (2013)
59. Lammer H et al. *Mon. Not. R. Astron. Soc.* **439** 3225 (2014)
60. Ionov D E, Shematovich V I *Solar Syst. Res.* **49** 339 (2015); *Astron. Vestn.* **49** 373 (2015)
61. Linsky J L, Güdel M, in *Characterizing Stellar and Exoplanetary Environments* (Astrophysics and Space Science Library, Vol. 411, Eds H Lammer, M Khodachenko) (Cham: Springer, 2015) p. 3
62. Waite J H et al. *J. Geophys. Res.* **88** 6143 (1983)
63. Majeed T et al. *J. Geophys. Res. Planets* **114** E07005 (2009)
64. Badman S V et al. *Space Sci. Rev.* **187** 99 (2015)
65. Nichols J D *Mon. Not. R. Astron. Soc.* **414** 2125 (2011)
66. Bonfond B et al. *J. Geophys. Res. Space Phys.* **122** 7985 (2017)
67. Bonfond B et al. *Geophys. Res. Lett.* **39** L01105 (2012)
68. Kislyakova K G et al. *Science* **346** 981 (2014)
69. Lavvas P, Koskinen T, Yelle R V *Astrophys. J.* **796** 15 (2014)
70. Bourrier V, Lecavelier des Etangs A, Vidal-Madjar A *Astron. Astrophys.* **565** A105 (2014)
71. Bisikalo D V, Shematovich V I *Astron. Rep.* **59** 836 (2015); *Astron. Zh.* **92** 713 (2015)
72. Bisikalo D V et al. *Icarus* **282** 127 (2017)
73. Hardy D A, Gussenhoven M S, Holeman E *J. Geophys. Res.* **90** 4229 (1985)
74. Pavlyuchenkov Ya N et al. *Astron. Rep.* **59** 133 (2015); *Astron. Zh.* **92** 154 (2015)
75. Ionov D E, Shematovich V I, Pavlyuchenkov Ya N *Astron. Rep.* **61** 387 (2017); *Astron. Zh.* **94** 381 (2017)
76. Samarskii A A, Popov Yu P *Raznostnye Metody Resheniya Zadach Gazovoi Dinamiki* (Differential Methods of Solutions of Gas-Dynamical Problems) (Moscow: Nauka, 1992)
77. Withbroe G L *Astrophys. J.* **325** 442 (1988)
78. Huebner W F, Keady J J, Lyon S P *Astrophys. Space Sci.* **195** 1 (1992)
79. Bisikalo D V et al. *Astrophys. J.* **869** 108 (2018)
80. Lecavelier Des Etangs A et al. *Astron. Astrophys.* **514** A72 (2010)
81. Fossati L et al. *Astrophys. J.* **720** 872 (2010)

82. Lai Dong, Helling Ch, van den Heuvel E P J *Astrophys. J.* **721** 923 (2010)
83. Li Shu Lin et al. *Nature* **463** 1054 (2010)
84. Vidotto A A, Jardine M, Helling Ch *Astrophys. J.* **722** L168 (2010)
85. Vidotto A A, Jardine M, Helling Ch *Mon. Not. R. Astron. Soc.* **411** L46 (2011)
86. Vidotto A A, Jardine M, Helling Ch *Mon. Not. R. Astron. Soc.* **414** 1573 (2011)
87. Boyarchuk A A et al. *Mass Transfer in Close Binary Stars: Gas Dynamical Treatment* (Advances in Astronomy and Astrophysics, Vol. 6) (London: Taylor and Francis, 2002)
88. Bisikalo D V, Zhilkin A G, Boyarchuk A A *Gazodinamika Tesnykh Dvoinykh Zvezd* (Gas Dynamics of Close Binary Systems) (Moscow: Fizmatlit, 2013)
89. Kopal Z *Close Binary Systems* (New York: Wiley, 1959)
90. Plavec M, Kratochvil P *Bull. Astron. Inst. Czechslov.* **15** 165 (1964)
91. Savonije G J *Astron. Astrophys.* **71** 352 (1979)
92. Pringle J E, Wade R A (Eds) *Interacting Binary Stars* (Cambridge Astrophysics Series, Vol. 6) (Cambridge: Cambridge Univ. Press, 1985)
93. Bisikalo D V, Kaygorodov P V, Arakcheev A S *Living Together Planets, Host Stars, and Binaries. Proc. of a Conf., Litomyšl, Czech Republic, 8–12 September 2014* (Astronomical Society of the Pacific Conf. Ser., Vol. 496, Eds S M Rucinski, G Torres, M Zejda) (San Francisco, CA: Astronomical Society of the Pacific, 2015) p. 337
94. Landau L D, Lifshitz E M *Fluid Mechanics* (Oxford: Pergamon Press, 1987); Translated from Russian: *Gidrodinamika* (Moscow: Nauka, 1988)
95. Baranov V B, Krasnobaev K V *Gidrodinamicheskaya Teoriya Kosmicheskoi Plazmy* (Hydrodynamic Theory of a Cosmic Plasma) (Moscow: Nauka, 1977)
96. Verigin M et al. *J. Geophys. Res. Space Phys.* **108** 1323 (2003)
97. Koskinen T T et al. *Astrophys. J.* **723** 116 (2010)
98. Lubow S H, Shu F H *Astrophys. J.* **198** 383 (1975)
99. Cherenkov A A, Bisikalo D V, Kaigorodov P V *Astron. Rep.* **58** 679 (2014); *Astron. Zh.* **91** 775 (2014)
100. Bisikalo D V et al. *Astron. Rep.* **48** 449 (2004); *Astron. Zh.* **81** 494 (2004)
101. Bourrier V, Lecavelier des Etangs A *Astron. Astrophys.* **557** A124 (2013)
102. Katushkina O A, Izmodenov V V *Astron. Lett.* **36** 297 (2010); *Pis'ma Astron. Zh.* **36** 310 (2010)
103. Cherenkov A A, Bisikalo D V, Kosovichev A G *Mon. Not. R. Astron. Soc.* **475** 605 (2018)
104. Curdt W et al. *Astron. Astrophys.* **375** 591 (2001)
105. Wiese W L, Smith M W, Glennon B M *Atomic Transition Probabilities. A Critical Data Compilation* Vol. 1 *Hydrogen through Neon* (Washington, DC: U.S. Dept. of Commerce, National Bureau of Standards, 1966)
106. Brasken M, Kyrola E *Astron. Astrophys.* **332** 732 (1998)
107. Roe P L, in *Seventh Intern. Conf. on Numerical Methods in Fluid Dynamics. Proc. of the Conf., Stanford, CA, June 23–27, 1980* (Lecture Notes in Physics, Vol. 141, Eds W C Reynolds, R W MacCormack) (Berlin: Springer, 1981) p. 354
108. Balsara D *Astrophys. J. Suppl.* **132** 83 (2001)
109. Cantó J et al. *Astrophys. J.* **502** 695 (1998)
110. Scholz T T, Walters H R J *Astrophys. J.* **380** 302 (1991)
111. Møller P, Jakobsen P *Astron. Astrophys.* **228** 299 (1990)
112. Schneiter E M et al. *Mon. Not. R. Astron. Soc.* **457** 1666 (2016)
113. Sanz-Forcada J et al. *Astron. Astrophys.* **532** A6 (2011)
114. *The HIPPARCOS and TYCHO Catalogues. Astrometric and Photometric Star Catalogues Derived from the ESA HIPPARCOS Space Astrometry Mission* (ESA Special Publ. Ser., No. 1200) (Noordwijk: ESA Publ. Division, 1997)
115. Ermolaev A M *J. Phys. B* **21** 81 (1988)
116. Boyajian T et al. *Mon. Not. R. Astron. Soc.* **447** 846 (2015)
117. Callaway J *Phys. Lett. A* **48** 359 (1974)
118. Bell K L, Kingston A E *Proc. Phys. Soc.* **90** 895 (1967)
119. Inokuti M, Kim Y K *Phys. Rev.* **173** 154 (1968)
120. Bell K L, Kingston A E, McIlveen W A *J. Phys. B* **8** 358 (1975)
121. Bisikalo D V, Kaigorodov P V, Konstantinova N I *Astron. Rep.* **59** 829 (2015); *Astron. Zh.* **92** 705 (2015)
122. Shaikhislamov I F et al. *Mon. Not. R. Astron. Soc.* **481** 5315 (2018)
123. Dwivedi N K et al. *Mon. Not. R. Astron. Soc.* **487** 4208 (2019)
124. Shaikhislamov I F et al. *Mon. Not. R. Astron. Soc.* **491** 3435 (2020)
125. Grie meier J M et al. *Astron. Astrophys.* **425** 753 (2004)
126. Sánchez-Lavega A *Astrophys. J.* **609** L87 (2004)
127. Stevenson D J *Rep. Prog. Phys.* **46** 555 (1983)
128. Showman A P, Guillot T *Astron. Astrophys.* **385** 166 (2002)
129. Jones C A *Annu. Rev. Fluid Mech.* **43** 583 (2011)
130. Jones C A *Icarus* **241** 148 (2014)
131. Braginskii S I *Sov. Phys. JETP* **20** 1462 (1965); *Zh. Eksp. Teor. Fiz.* **47** 2178 (1964)
132. Parker E N *Cosmical Magnetic Fields: Their Origin and Their Activity* (Oxford: Clarendon Press, 1979)
133. Cowling T G *Mon. Not. R. Astron. Soc.* **94** 39 (1933)
134. Batygin K, Stanley S, Stevenson D J *Astrophys. J.* **776** 53 (2013)
135. Rogers T M, Showman A P *Astrophys. J.* **782** L4 (2014)
136. Rogers T M, Komacek T D *Astrophys. J.* **794** 132 (2014)
137. Rogers T M *Nat. Astron.* **1** 0131 (2017)
138. Moore K M et al. *Nature* **561** 76 (2018)
139. Erkaev N V et al. *Mon. Not. R. Astron. Soc.* **470** 4330 (2017)
140. Zhilkin A G, Bisikalo D V *Astron. Rep.* **63** 550 (2019); *Astron. Zh.* **96** 547 (2019)
141. Belenkaya E S *Phys. Usp.* **52** 765 (2009); *Usp. Fiz. Nauk* **179** 809 (2009)
142. Russell C T *Rep. Prog. Phys.* **56** 687 (1993)
143. Ip W H, Kopp A, Hu J H *Astrophys. J.* **602** L53 (2004)
144. Koskinen T T et al. *Astrophys. J.* **722** 178 (2010)
145. Trammell G B, Arras P, Li Z Y *Astrophys. J.* **728** 152 (2011)
146. Trammell G B, Li Z Y, Arras P *Astrophys. J.* **788** 161 (2014)
147. Matsakos T, Uribe A, Königl A *Astron. Astrophys.* **578** A6 (2015)
148. Arakcheev A S et al. *Astron. Rep.* **61** 932 (2017); *Astron. Zh.* **94** 927 (2017)
149. Bisikalo D V, Arakcheev A S, Kaigorodov P V *Astron. Rep.* **61** 925 (2017); *Astron. Zh.* **94** 920 (2017)
150. Zhilkin A G, Bisikalo D V, Kaygorodov P V *Astron. Rep.* **64** 159 (2020); *Astron. Zh.* **97** 145 (2020)
151. Zhilkin A G, Bisikalo D V, Kaygorodov P V *Astron. Rep.* **64** 259 (2020); *Astron. Zh.* **97** 242 (2020)
152. Zhilkin A G, Bisikalo D V *Astron. Rep.* **97** 538 (2020); *Astron. Zh.* **97** 538 (2020)
153. Zhilkin A G, Bisikalo D V, Boyarchuk A A *Phys. Usp.* **55** 115 (2012); *Usp. Fiz. Nauk* **182** 121 (2012)
154. Tanaka T *J. Comput. Phys.* **111** 381 (1994)
155. Powell K G et al. *J. Comput. Phys.* **154** 284 (1999)
156. Lax P D *Commun. Pure Appl. Math.* **7** 159 (1954)
157. Friedrichs K O *Commun. Pure Appl. Math.* **7** 345 (1954)
158. Rusanov V V *USSR Comput. Math. Math. Phys.* **1** 304 (1962); *Zh. Vychisl. Matem. Matem. Fiz.* **1** 267 (1961)
159. Cargo P, Gallice G *J. Comput. Phys.* **136** 446 (1997)
160. Kulikovskii A G, Pogorelov N V, Semenov A Yu *Mathematical Aspects of Numerical Solution of Hyperbolic System* (Chapman and Hall Monographs and Surveys in Pure and Applied Mathematics, Vol. 118) (Boca Raton, FL: Chapman and Hall. CRC, 2001); Translated from Russian: *Matematicheskie Voprosy Chislennogo Resheniya Giperbolicheskikh Sistem Uravnenii* (Moscow: Fizmatlit, 2001)
161. Chakravarthy S R, Osher S, in *Proc. of the 23rd Aerospace Sciences Meeting, 14–17 January 1985, Reno, NV, USA,* No. 85 AIAA (Reston, VA: AIAA, 1985) pap. 363, https://arc.aiaa.org/doi/abs/10.2514/6.1985-363
162. Zhilkin A G et al. *Astron. Rep.* **63** 751 (2019); *Astron. Zh.* **96** 748 (2019)
163. Einfeldt B *SIAM J. Numer. Anal.* **25** 294 (1988)
164. Harten A, Hyman J M *J. Comput. Phys.* **50** 235 (1983)
165. Dedner A et al. *J. Comput. Phys.* **175** 645 (2002)
166. Farrell W M et al. *Bioastronomy 2002: Life Among the Stars. Proc. of the 213th Symp. of the Intern. Astronomical Union Hamilton Island, Great Barrier Reef, Australia* (Eds R P Norris, F H Stootman) (San Francisco, CA: Astronomical Society of the Pacific, 2004) p. 73
167. Weber C et al. *Mon. Not. R. Astron. Soc.* **469** 3505 (2017)
168. Wu C S, Lee L C *Astrophys. J.* **230** 621 (1979)
169. Owens M J, Forsyth R J *Living Rev. Solar Phys.* **10** 5 (2013)
170. Parker E N *Astrophys. J.* **128** 664 (1958)
171. Weber E J, Davis L (Jr.) *Astrophys. J.* **148** 217 (1967)

172. Brandt J C, Wolff C, Cassinelli J P *Astrophys. J.* **156** 1117 (1969)
173. Sakurai T *Sol. Phys.* **76** 301 (1982)
174. Goelzer M L, Schwadron N A, Smith C W *J. Geophys. Res. Space Phys.* **119** 115 (2014)
175. Fabbian D et al. *Astron. Nachrichten* **338** 753 (2017)
176. Lammer H et al. *Earth Planets Space* **64** 179 (2012)
177. Khodachenko M L et al. *Astrophys. J.* **744** 70 (2012)
178. Mestel L *Mon. Not. R. Astron. Soc.* **138** 359 (1968)
179. Alexeev I I, Belenkaya E S *Ann. Geophys.* **23** 809 (2005)
180. Charbonneau D et al. *Astrophys. J.* **529** L45 (2000)
181. Khodachenko M L et al. *Astrophys. J.* **885** 67 (2019)
182. Awiphan S et al. *Mon. Not. R. Astron. Soc.* **463** 2574 (2016)
183. Chen F F *Introduction to Plasma Physics and Controlled Fusion* Vol. 1 *Plasma Physics* (New York: Plenum Press, 1984)
184. Maehara H et al. *Nature* **485** 478 (2012)
185. Shibayama T et al. *Astrophys. J. Suppl.* **209** 5 (2013)
186. Maehara H et al. *Earth Planets Space* **67** 59 (2015)
187. Vourlidas A et al. *Astrophys. J.* **722** 1522 (2010)
188. Webb D F, Howard T A *Living Rev. Solar Phys.* **9** 3 (2012)
189. Bisikalo D V, Cherenkov A A *Astron. Rep.* **60** 183 (2016); *Astron. Zh.* **93** 139 (2016)
190. Cherenkov A et al. *Astrophys. J.* **846** 31 (2017)
191. Bisikalo D V et al. *Astron. Rep.* **62** 648 (2018); *Astron. Zh.* **95** 686 (2018)
192. Cherenkov A A, Bisikalo D V, in *Sbornik Trudov Memorial'noi Konf. 2018 g., Posvyashchennoi Pamyati Akademika A.A. Boyarchuka* (Proc. of the A.A. Boyarchuk Memorial Conf. 2018) (Sb. Nauch. Tr. INASAN, Vol. 1, Eds D V Bisikalo, D Z Vibe) (Moscow: Yanus-K, 2018) p. 265
193. Cherenkov A A et al. *Astron. Rep.* **63** 94 (2019); *Astron. Zh.* **96** 106 (2019)
194. Kaigorodov P V, Ilyina E A, Bisikalo D V *Astron. Rep.* **63** 365 (2019); *Astron. Zh.* **96** 367 (2019)
195. Ionov D E, Pavlyuchenkov Ya N, Shematovich V I *Mon. Not. R. Astron. Soc.* **476** 5639 (2018)
196. Veronig A et al. *Astron. Astrophys.* **382** 1070 (2002)
197. Tsurutani B T et al. *Geophys. Res. Lett.* **32** L03S09 (2005)
198. Khodachenko M L et al. *Astrobiology* **7** 167 (2007)
199. Lammer H et al. *Astrobiology* **7** 185 (2007)
200. Kay C et al. *Astrophys. J.* **827** 70 (2016)
201. Farrell W M et al. *J. Geophys. Res. Planets* **117** E00K04 (2012)
202. Möstl C et al. *Astrophys. J.* **787** 119 (2014)
203. Richardson I G, Cane H V *Solar Phys.* **264** 189 (2010)
204. Kaigorodov P V, Il'ina E A *Nauch. Tr. Inst. Astron. Ross. Akad. Nauk* **3** 124 (2019)
205. Bisikalo D V, Cherenkov A A, Kaygorodov P V, in *Solar and Stellar Flares and their Effects on Planets: Proc. of the 320th Symp. of the International Astronomical Union, Honolulu, United States, August 11 – 14, 2015* (IAU Symp., Vol. 320, Eds A G Kosovichev, S L Hawley, P Heinzel) (Cambridge: Cambridge Univ. Press, 2016) p. 224
206. Johnstone C P et al. *Astron. Astrophys.* **577** A122 (2015)
207. Vidotto A A et al., in *18th Cambridge Workshop on Cool Stars, Stellar Systems, and the Sun, Proc. of the Conf. Lowell Observatory, 8 – 14 June, 2014* (Eds G T van Belle, H C Harris) (San Francisco, CA: Astronomical Society of the Pacific, 2015) p. 65
208. Czesla S et al. *Astron. Astrophys.* **629** A5 (2019)
209. Kurbatov E P, Bisikalo D V, Shaikhislamov I F *Astron. Rep.* **64** 1016 (2020); *Astron. Zh.* **97** 986 (2020)
210. Sproß L et al. *Astron. Rep.* **65** 275 (2021)